RIGA TECHNICAL UNIVERSITY

Luca Piacentini

MECHANICAL DESIGN AND OPTIMIZATION OF A SUPPORTING SYSTEM FOR CRYOGENIC DEVICES UNDER VARIABLE LOADS: THE STUDY CASE OF A CARBON ION ROTATING GANTRY FOR MEDICAL TREATMENTS

Doctoral Thesis

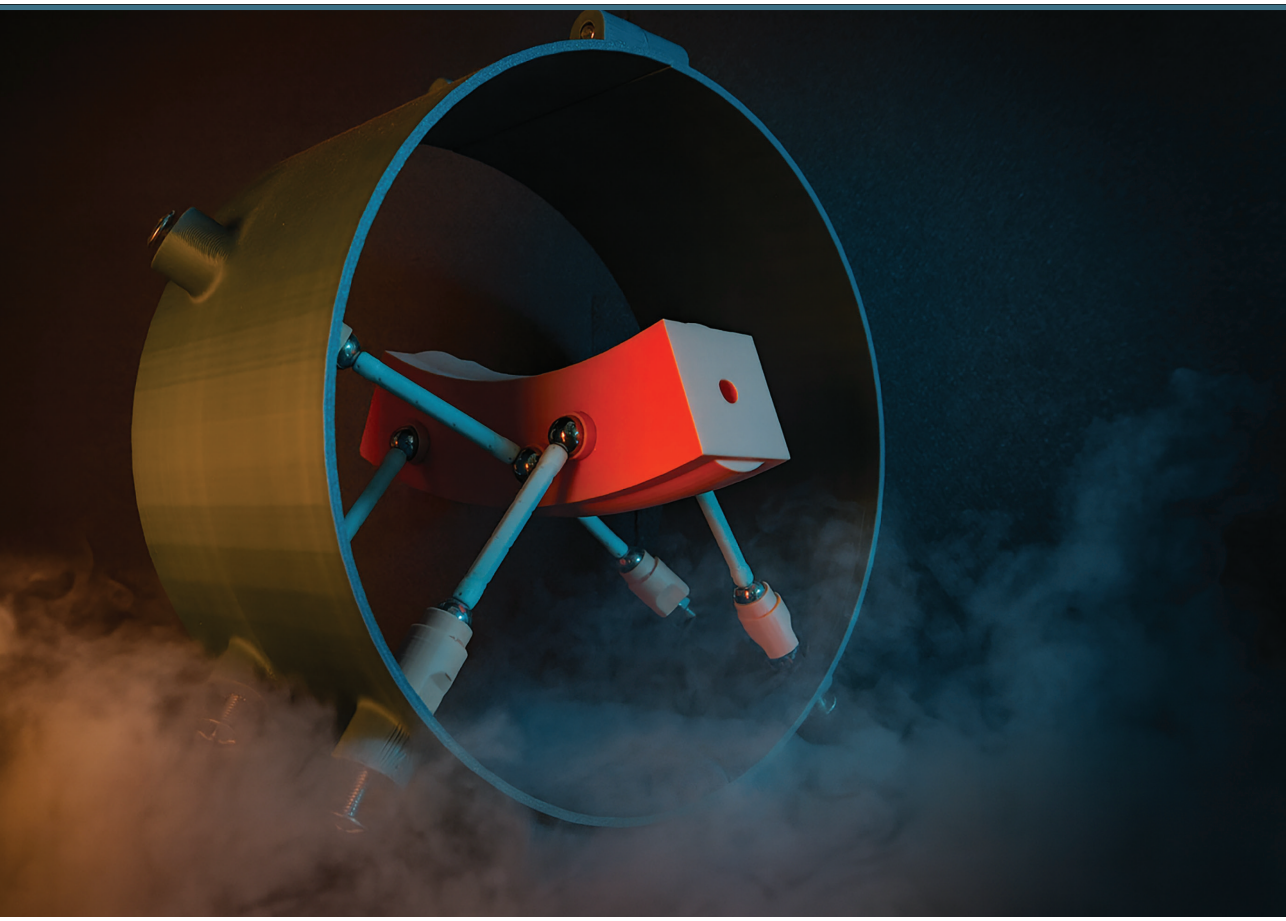

RTU Press
Riga 2025

RIGA TECHNICAL UNIVERSITY

Faculty of Natural Sciences and Technology
Institute of Particle Physics and Accelerator Technologies

Luca Piacentini
Doctoral Student of the Study Programme:
"Particle Physics and Accelerator Technologies"

MECHANICAL DESIGN AND OPTIMIZATION OF A SUPPORTING SYSTEM FOR CRYOGENIC DEVICES UNDER VARIABLE LOADS:

THE STUDY CASE OF A CARBON ION ROTATING GANTRY FOR MEDICAL TREATMENTS

Scientific Supervisors

Professor Dr. sc. eng. TOMS TORIMS
Dr. sc. eng. LUCA DASSA
Professor Dr. sc. eng. STEFANO UBERTI

RTU Press
Riga 2025

Piacentini, L. Mechanical Design and Optimization of a Supporting System for Cryogenic Devices under Variable Loads: The Study Case of a Carbon Ion Rotating Gantry for Medical Treatments. Summary of the Doctoral Thesis. – Riga: RTU Press, 2025, 168 p.

Published in accordance with the decision of the Promotion Council "RTU-04" of 4 july, 2025, Minutes No. 04030-9.4/1.

AKNOWLEDGEMENTS

I would like to express my deepest gratitude to my supervisors, Dr. Luca Dassa, Prof. Toms Torims, and Prof. Stefano Uberti, who guided me throughout my doctoral research, conducted at both CERN and Riga Technical University. I am sincerely thankful for everything they have taught me, and for their invaluable advice on how to grow not only as a researcher but also as a professional and as a person. I am also grateful to Dr. Maurizio Vretenar, the leader of the NIMMS initiative at CERN, and to Prof. Toms Torims, Prof. Kārlis Dreimanis, and Dr. Andris Ratkus, members of IPPAT, for the financial support that enabled me to carry out my research at CERN. My thanks extend as well to the EN-MME group at CERN and to UNIBS, for making it possible for Dr. Luca Dassa and Prof. Stefano Uberti to supervise my work. Finally, I wish to thank my family and friends for their unhesitating and tireless support throughout this four-year journey across Europe despite the thousands of kilometers that often separated us.

Cover Picture by *Luca Piacentini*.

DOCTORAL THESIS PROPOSED TO RIGA TECHNICAL UNIVERSITY FOR PROMOTION TO THE SCIENTIFIC DEGREE OF DOCTOR OF SCIENCE

To be granted the scientific degree of Doctor of Science, the present Doctoral Thesis has been submitted for defence at the open meeting of RTU Promotion Council on December 12, 2025, at 11.00, Zoom online https://rtucloud1.zoom.us/j/94276909347.

OFFICIAL REVIEWERS

Dr. sc. Eng. Olga Kononova,
Riga Technical University

Dr. sc. Alberto Degiovanni
Riga Technical University

Dr. sc. Florent Cosandier
École Polytechnique Fédérale de Lausanne, Switzerland

Dr. sc. Eduardo Cano Pleite
University of Madrid, Spain

DECLARATION OF ACADEMIC INTEGRITY

I hereby declare that the Doctoral Thesis submitted for review to Riga Technical University for promotion to the scientific degree of Doctor of Science is my own. I confirm that this Doctoral Thesis has not been submitted to any other university for promotion to a scientific degree.

Luca Piacentini ..... (signature)
Date: .....

The Doctoral Thesis has been written in English. It consists of an Introduction; 8 Chapters; Conclusion; 74 figures; 39 tables; 4 appendices; the total number of pages is 169, including appendices. The Bibliography contains 114 titles.

Abstract

This work proposes the design and optimization of the multi-rod ($\geq$6 rods) supporting system for cryogenic devices under variable loads. The case study of a carbon ion gantry for medical treatments has been used as an application example for the developed models.

Cryogenic devices require to solve a set of engineering challenges that are unique for these applications. One of the mechanical challenges is represented by the supporting system of the device. On one hand, the supporting system must be as stiff as possible to guarantee accuracy under variable loading conditions, reacting to high variable loads related to the rotation in the case of the gantry. On the other hand the supporting system represent a direct connection between the room temperature environment and the cryogenic device cooled at cryogenic temperatures ($-268.5\,^{\circ}$C) transferring heat to the cooled components. This represent a cost to keep the system functional at nominal temperatures as the heat must be extracted. The design of supports, their material and their arrangement play a key role in guaranteeing high stiffness and low heat-loads and costs.

No documented evidence has been found regarding the mathematical formalization of design of supporting systems for cryogenic devices subject to highly variable loads. While most common applications rely on statically indeterminate solutions under static loads, there is no documented knowledge on the potential use of a statically determinate supporting system for variable loads.

This work proposes the design and optimization of two supporting systems based on supporting bars, covering both the statically determinate and indeterminate solutions and comparing them using the gantry application as a study case. Both architectures have been mathematically described by so called Lumped Parameter Models (LPMs). These models enable to study the effect of a generic load, pre-load, cooling process, backlash and vacuum on the position and orientation of the cryogenic device and the stress state of the supports. For the statically indeterminate case a generic formulation of the model has been developed, applicable to solutions with any number of supports and without pre-imposed symmetries. This formulation represents an extremely valuable result of this work regarding the applicability to a much greater number of applications.

The models have been benchmarked against a widely used Finite Element Analysis (FEA) software proving the results of the developed LPMs to differ of only 1–3%. The developed models have been demonstrated to be 20 times faster than FEA in providing the same results, unlocking the full potential of computer aided optimization codes that would have been much more computationally expensive otherwise. A genetic optimization routine based on the developed LPMs have been presented and used to optimize both statically determinate and indeterminate supporting systems in the case study of the gantry. On average, the accuracy of the systems during rotation has been improved by 16% and heatloads reduced by 44% with respect to initially proposed solutions. The necessity of preload to remove backlash has been demonstrated, improving the accuracy matching the requirements, otherwise not satisfied for the system with backlash.

A comparison of different materials and size of supports has been done thanks to the LPMs enabling to find the optimal material for each of the supporting systems. Finally

the two designed and optimized supporting systems have been compared. A qualitative parameter in the comparison considered is the possibility of automating the positioning of the cryogenic device thanks to the designed supporting system. Results show that, assuming no automation of the supporting system, the statically indeterminate solution performs overall better in terms of positional accuracy during operation, minimal heat-flux and safety margin over transportation/handling loads while no major difference has been found analyzing the natural frequencies of the two solutions. In case of automation of the supporting system, the developed statically determinate solution represent a better candidate, allowing to recover elastic deformations also of the gantry main structure ultimately allowing to reduce its mass.

Anotācija

Šajā darbā tiek piedāvāta daudzstieņu ($\geq$6 stieņi) balsta sistēmas projektēšana un optimizācija kriogēnām ierīcēm mainīgu slodžu apstākļos. Kā izstrādāto modeļu piemērošanas piemērs izmantots oglekļa jonu rotējošs gantrijs medicīniskai ārstēšanai.

Kriogēnām ierīcēm ir nepieciešams risināt specifisku inženiertehnisku izaicinājumu kopumu, kas ir unikāli šīm pielietojumam. Viens no mehāniskajiem izaicinājumiem ir ierīces balsta sistēma. No vienas puses, balsta sistēmai jābūt iespējami stingrai, lai nodrošinātu precizitāti mainīgu slodžu apstākļos, reaģējot uz lielām mainīgām slodzēm, kas rotējoša gantrija gadījumā saistītas ar rotāciju. No otras puses, balsta sistēma veido tiešu savienojumu starp telpas temperatūras vidi un kriogēno ierīci, kas tiek atdzesēta līdz kriogēnām temperatūrām ($-268.5\,^{\circ}\mathrm{C}$), pārnesot siltumu uz atdzesētajām komponentēm. Tas rada izmaksas sistēmas uzturēšanai nominālajās temperatūrās, jo šis siltums ir jāizvada. Balstu konstrukcija, to materiāls un izkārtojums ir izšķiroši faktori, lai nodrošinātu augstu stingrību un zemas siltuma slodzes un izmaksas.

Nav atrasti dokumentēti pierādījumi par balsta sistēmu projektēšanas matemātisko formalizāciju kriogēnām ierīcēm, kas pakļautas ļoti mainīgām slodzēm. Lai gan biežākās visbiežāk pielietojumi balstās uz statiski nenoteiktām sistēmām statisku slodžu apstākļos, nav dokumentētu zināšanu par statiski noteiktas sistēmas potenciālu izmantošanu mainīgu slodžu gadījumā.

Šajā darbā tiek piedāvāta divu balsta sistēmu projektēšana un optimizācija, balstoties uz balsta stieņiem, aptverot gan statiski noteiktas sistēmas, gan statiski nenoteiktas sistēmas, un tās salīdzinot, izmantojot rotējoša gantrija piemēru kā gadījuma izpēti.. Abas arhitektūras ir matemātiski aprakstītas ar tā sauktajiem koncentrēto (Angl. *lumped*) parametru modeļiem (LPM). Šie modeļi ļauj pētīt vispārīgas slodzes, iepriekšējās nospriegošanas, atdzišanas procesa, mehāniskās brīvgaitas (Angl. *backlash*) un vakuuma ietekmi uz kriogēnās ierīces pozīciju un orientāciju, kā arī uz balstu sprieguma stāvokli. Statiski nenoteiktās sistēmas gadījumā ir izstrādāta vispārīga modeļa formulācija, ko var pielietot risinājumiem ar jebkuru balstu skaitu un bez iepriekš noteiktām simetrijām. Šī formulācija ir ļoti vērtīgs šī darba rezultāts attiecībā uz tās pielietojamību daudz plašākam lietojumu lokam.

Modeļi ir salīdzināti ar plaši izmantotas galīgo elementu analīzes (FEA) programmatūras rezultātiem, pierādot, ka izstrādāto LPM rezultāti atšķiras tikai par 1–3%. Ir

pierādīts, ka izstrādātie modeļi ir 20 reizes ātrāki par FEA, nodrošinot tādus pašus rezultātus un tādējādi atverot iespēju pilnvērtīgi izmantot datorizētas optimizācijas algoritmus, kuru izmantošana citādi būtu ievērojami dārgāka skaitļošanas ziņā. Balstoties uz izstrādātajiem LPM, ir izveidota ģenētiskās optimizācijas metode, kas izmantota gan statiski noteiktu, gan statiski nenoteiktu balsta sistēmu optimizācijai rotējoša gantrija gadījuma izpētē. Vidēji sistēmu precizitāte rotācijas laikā ir uzlabota par 16%, bet siltuma slodzes samazinātas par 44%, salīdzinot ar sākotnēji piedāvātajiem risinājumiem. Ir pierādīta nepieciešamība ieviest iepriekšējo nospriegošanu, lai novērstu mehānisko brīvgaitu, tādējādi uzlabojot precizitāti līdz prasību līmenim, kas pretējā gadījumā sistēmām ar brīvgaitu netiktu sasniegts.

Pateicoties LPM izmantošanai, ir veikts dažādu balstu materiālu un izmēru salīdzinājums, nosakot optimālo materiālu katrai no balsta sistēmām. Noslēgumā ir salīdzinātas abas projektētās un optimizētās balsta sistēmas. Kā viens no kvalitatīvajiem salīdzinājuma parametriem ņemta iespēja automatizēt kriogēnās ierīces pozicionēšanu, izmantojot izstrādāto balsta sistēmu. Rezultāti rāda, ka, pieņemot, ka balsta sistēma netiek automatizēta, statiski nenoteiktā sistēma kopumā sniedz labākus rezultātus pozicionālās precizitātes, minimāla siltuma plūsmas un drošības rezervei pārvadāšanas/apstrādes slodžu apstākļos, kamēr dabisko frekvenču analīzē būtiskas atšķirības nav konstatētas. Savukārt, ja balsta sistēma tiek automatizēta, izstrādātā statiski noteiktā sistēma ir labāks kandidāts, jo tā ļauj kompensēt arī rotējošā gantrija galvenās konstrukcijas elastīgās deformācijas, galu galā ļaujot samazināt tā masu.

Sommario

In questo lavoro si propone la progettazione e l'ottimizzazione di un sistema di supporto multi-asta ($\geq$6 aste) per dispositivi criogenici sottoposti a carichi variabili. Come caso di studio, per l'applicazione dei modelli sviluppati, è stato utilizzato un gantry a ioni di carbonio per trattamenti medici.

I dispositivi criogenici richiedono di affrontare una serie di sfide ingegneristiche uniche per questo tipo di applicazioni. Una delle sfide meccaniche è rappresentata dal sistema di supporto del dispositivo. Da un lato, il sistema di supporto deve essere il più rigido possibile per garantire precisione in condizioni di carico variabile, reagendo a carichi molto variabili legati alla rotazione, nel caso del gantry. Dall'altro lato, il sistema di supporto rappresenta un collegamento diretto tra l'ambiente a temperatura ambiente e il dispositivo criogenico raffreddato a temperature criogeniche ($-268.5\,^{\circ}\mathrm{C}$), trasferendo calore verso le componenti raffreddate. Ciò comporta un costo per mantenere il sistema operativo alle temperature nominali, poiché il calore deve essere estratto. La progettazione dei supporti, il loro materiale e la loro disposizione svolgono un ruolo fondamentale nel garantire un'elevata rigidità e bassi carichi termici e costi.

Non sono state trovate evidenze in letteratura riguardo alla formalizzazione matematica di sistemi di supporto per dispositivi criogenici soggetti a carichi fortemente variabili. Sebbene le applicazioni più comuni si basino su soluzioni iperstatiche in condizioni di carico statico, non esistono conoscenze documentate sul potenziale utilizzo di un sistema di supporto isostatico per carichi variabili.

In questo lavoro si propone la progettazione e l'ottimizzazione di due sistemi di supporto basati su barre di sostegno, comprendenti sia soluzioni isostatiche sia iperstatiche, e il loro confronto utilizzando il gantry come caso di studio. Entrambe le architetture sono state descritte matematicamente mediante i cosiddetti Lumped Parameter Models (LPM, modelli a parametri concentrati). Questi modelli permettono di studiare l'effetto di un carico generico, del precarico, del processo di raffreddamento, del gioco meccanico e del vuoto sulla posizione e l'orientamento del dispositivo criogenico e sullo stato di stress dei supporti. Per il caso iperstatico è stata sviluppata una formulazione generica del modello, applicabile a soluzioni con un numero qualsiasi di supporti e senza simmetrie preimposte. Questa formulazione rappresenta un risultato estremamente prezioso per la sua applicabilità a un numero molto più ampio di applicazioni.

I modelli sono stati confrontati con un software di analisi agli elementi finiti (FEA) ampiamente utilizzato, dimostrando che i risultati dei LPM sviluppati differiscono solo dell'1–3%. È stato dimostrato che i modelli sviluppati sono 20 volte più veloci della FEA nel fornire gli stessi risultati, liberando così il pieno potenziale dei codici di ottimizzazione tramite calcolatore, la cui esecuzione sarebbe altrimenti molto più onerosa dal punto di vista computazionale. È stata presentata una procedura di ottimizzazione genetica basata sugli LPM sviluppati e utilizzata per ottimizzare sia i sistemi di supporto isostatici sia quelli iperstatici nel caso di studio del gantry. In media, la precisione dei sistemi durante la rotazione è stata migliorata del 16% e i carichi termici ridotti del 44% rispetto alle soluzioni inizialmente proposte. È stata dimostrata la necessità del precarico per eliminare il gioco meccanico, migliorando così la precisione fino a soddisfare i requisiti, cosa che altrimenti non sarebbe avvenuta nei sistemi con gioco.

Grazie all'utilizzo degli LPM è stato possibile effettuare un confronto tra diversi materiali e dimensioni dei supporti, individuando il materiale ottimale per ciascun sistema di supporto. Infine, sono stati confrontati i due sistemi di supporto progettati e ottimizzati. Un parametro qualitativo considerato nel confronto è la possibilità di automatizzare il posizionamento del dispositivo criogenico grazie al sistema di supporto progettato. I risultati mostrano che, ipotizzando l'assenza di automazione del sistema di supporto, la soluzione iperstatica offre complessivamente prestazioni migliori in termini di accuratezza di posizionamento durante il funzionamento, flusso termico minimo e margine di sicurezza nei confronti dei carichi di trasporto/manipolazione, mentre non sono state riscontrate differenze significative nell'analisi delle frequenze naturali delle due soluzioni. Nel caso di automazione del sistema di supporto, la soluzione isostatica sviluppata rappresenta un candidato migliore, consentendo di compensare anche le deformazioni elastiche della struttura principale del gantry, permettendo infine di ridurne la massa.

Contents

List of Figures

Acronyms

AIDS	Acquired Immunodeficiency Syndrome
ATLAS	A Toroidal LHC Apparatus (LHC Collaboration)
BT	Barrel Toroid
CAS	Chinese Academy of Sciences
CERN	Conseil Européen pour la Recherche Nucléaire
CFRP	Carbon Fibre Reinforced Polymer
CMS	Compact Muon Solenoid (LHC Experiment)
CNAO	National Center of Oncological hAdron therapy
CRT	Classical Radiation Therapy
CS	Central Solenoid
DEMO	DEMOnstration power plant
DOF	Degrees of Freedom
DPK	Direct Position Kinematics
ECT	End Cap Toroid
ELI	Extra Low Interstitial
ESS	European Spallation Source
FAIR	Facility for Antiproton and Ion Research
FDA	Federal Drug Administration
FEA	Finite Element Analysis
FEM	Finite Element Model
FPC	Fundamental Power Coupler
GAs	Genetic Algorithms
GFRE	Glass Fibre Reinforced Epoxy
HIE-ISOLDE	High Intensity and Energy ISOLDE
HITRI*plus*	Heavy Ion Therapy Research Integration plus
HL-LHC	High Luminosity LHC
HTS	High Temperature Superconducting
ICS	Inter-Cavity Support
IHEP	Institute of High Energy Physics of CAS
IPK	Inverse Position Kinematics
ISOLDE	Isotope Separator On Line DEvice
ITER	International Thermonuclear Experimental Reactor
LBL	Lawrence Berkley National Laboratory
LCLS-II	Linac Coherent Light Source II

LET	Linear Energy Transfer
LHC	Large Hadron Collider
LLUMC	Loma Linda University Medical Center
LPM	Lumped Parameter Model
MDS	Magnetic Density Separator
MICE	Muon Ionization Cooling Experiment
MRI	Magnetic Resonance Imaging
Mu2e	Muon-to-Electron-conversion
OARs	organs at risk
RBE	Relative Biological Effectiveness
RHIC	Relativistic Heavy Ion Collider
RTU	Riga Technical University
SC	Super Conducting
SPL	Superconducting Proton Linac
SSC	Superconducting Super Collider
SSRF	Shanghai Synchrotron Radiation Facility
SSS	Short Straight Section
TLS	Taiwan Light Source
UFGE	Unidirectional FibreGlass Epoxy
UT	University of Twente
VECC	Variable Energy Cyclotron Centre
WIPO	World Intellectual Property Organization

INTRODUCTION

A Cryogenic device is a specialized equipment that operates at extremely low temperature, from 1.8 K to 125 K. These devices are used in diverse fields such as scientific research, industrial production, and high-tech applications. Most of the components of particle accelerators used in the field of scientific research, in particular in high energy physics experiments, are cryogenic devices. Some other possible applications include superconducting generators for wind turbines, satellites and aerospace in general. Cryogenic devices are used as well in direct societal applications like superconducting magnets used for a particular cancer treatment.

Typically, all cryogenic devices require the implementation of an essential set of subsystems:

- cooling system: it is needed to maintain the cryogenic device at cryogenic temperatures in case of a superconducting element has the main scope of maintaining the material of the coils in a superconducting state (around $1.9 - 5\,\mathrm{K}$);
- external vacuum vessel: it is needed to keep the cryogenic device insulated from the external ambient eliminating thermal exchange by convection with ambient temperature air and limiting contamination; additionally, the vacuum vessel ensures low levels of air contamination and humidity inside the device.
- internal supports: are needed to maintain the device in the correct position resisting the loads applied during the operational phases;
- thermal screen: it surrounds the cryogenic device at a certain distance from it almost completely enveloping it. The main aim is to cut the direct path of radiative heat from ambient temperature of the vacuum vessel to cryogenic temperature of the cryogenic device. Hence, the thermal screen is actively cooled at an intermediate temperature between room temperature and cold temperature. Internal supports are often split in half by thermalizations that are anchored to the thermal screen acting as an heat sink for conduction heat-flux through supports.

The design of the supporting system for a cryogenic device requires to satisfy four main requirements:

- ensure functionality for the cryogenic device by holding it in the correct position;
- grant sufficient rigidity in order to reduce elastic deformations and accuracy losses due to loads;
- minimize the heat-flux through the supports, this results in a reduction of running costs for the cryogenic cooling system;

- align the cryogenic device at warm during the passive alignment phase and in special cases also at nominal cryogenic temperatures to ensure higher levels of position accuracy.

The functionality of most cryogenic devices used in research and high tech applications is often related to the accuracy of the positioning of the device under the loads that are applied to it. An initial analysis of literature highlighted that most supporting systems are designed for static loads. Hence, since the operational loads are static, the loss of positioning accuracy due to elasticity in the system is recovered during a passive alignment phase at room temperature conditions (before the cool-down phase). Earthquake or vibration loads are not considered in the most cases, or if considered do not impact significantly the design of the supports. In case of a general variable load (i.e. resulting in a continuous displacement of the cold mass in the space) the position accuracy cannot be compensated during the passive alignment phase and the study of the impact of the stiffness of supports and their arrangement is of crucial importance.

The literature analysis highlighted the lack of clear documented scientific knowledge about the combined area of study of cryogenic device supporting systems, precise positioning and variable loads. Additionally, in literature rarely are presented formalized mathematical models to study the internal actions on the supports of a cryogenic device under loads. Such models lack also of generality and rely on assumption of symmetric support configuration. Furthermore, no model has been found for a mathematical model able to predict displacements of the cryogenic device under loads.

The study case of a superconducting C-ion gantry for medical treatments falls entirely in the previously mentioned knowledge gap and will be used in this thesis as an example to develop models that can be applied also on different applications. This thesis proposes to study only rod-supporting systems, because these have been found to be the most commonly used in documented static cases. Additionally, the use of rod supporting systems enables to have mainly axial loads on the supports, reducing the need of greater cross-sections that would be necessary to reduce the stress due to other internal actions, (i.e. shear).

The following sections give a detailed explanation of the use of cryogenic devices on a rotating gantry for medical treatments, highlighting the importance of this application for society.

1.1 Hadron-therapy background

Nowadays, more and more countries are improving their wealth, thus the control over diseases that are more common to low-income countries [1] is greatly improved, rising the life expectancy. Consequently, in wealthier states, people face an increasing probability to be affected by diseases that are harder to diagnose and treat. To illustrate, while neonatal conditions, diarrhoeal diseases, malaria, tuberculosis and AIDS are in the list of leading causes of death for low-income parts of the world, for high-income countries these are completely replaced by: Alzheimer's disease and other dementias; trachea, bronchus, lung, colon and rectum cancers; chronic obstructive pulmonary diseases, kidney diseases and diabetes mellitus [1].

In 2020, 2.7 million people in the European Union were diagnosed with cancer, and another 1.3 million people died as consequence of the same disease. Another source estimates figures related to the European area to be over 4 million for diagnosed people, and 1.9 million deaths [2]. Figures are estimated to be around 19.2 million for the whole world [3]. Today, Europe hosts a tenth of world's population but contributes to a quarter of world's cancer cases. Figures of lives lost due to cancer are expected to rise by more than 24% by 2035. Although cancer is an individual diagnosis, it has non-negligible impacts on the lives of the patient's relatives and social group. The overall economic impact of cancer in Europe is estimated to cost more than 100 billions € per year [4].

To date, different types of cancer treatment exist [5]. The most common are:

1. Surgery: the surgeon removes cancer tissues from the patient body. This procedure can give a complete or partial cure for the cancer. If the cancer has metastasized to other parts of the body, the complete removal of cancer by surgical process is no longer an available option. This treatment is applied when the tumor is small and localized. The presence of a single cancer cell, due to an incomplete removal of the tumor, can lead to recurrence of it. The proximity of the tumor to healthy vital organs is one of the difficulties associated with this treatment.
2. Chemotherapy: this method is carried out through the use of drugs to kill or destroy the cancer cells. This treatment is generally considered an effective method, however, it can cause side effects [6] as the drugs used can damage healthy cells or tissues. Side effects depend upon the type of drugs being used, the type and location of the cancer and the individual's response to the specific treatment.
3. Radiation therapy: high doses of radiation, traditionally ionizing radiations, are used to kill cancer cells. Radiation therapy given both internally and externally can also damage the normal cells. Radiation therapy is commonly used to treat most of the types of tumors. The radiation dose to be delivered to the tumor depends upon age of the person, type of the tumor, location of the tumor and possible side effects on organs at risk (OARs). The conventional photon therapy is used mostly on adults, due to major side effects on pediatric cases. Hadron therapy is a type of radiation therapy that uses heavy ions or protons to kill cancer cells. Thanks to the physic related to these particles there is an higher chance to spare OARs. Carbon Ion therapy may provide a particularly important benefit in the pediatric population [7].
4. Bone marrow transplant: by replacing the bone marrow of the patient with healthy stem cells the ability to create blood cells is restored. This treatment can be use to treat blood and immune system diseases that affect the bone marrow.
5. Immunotherapy: This treatment is known also as biologic therapy, aiming to train the immune system to recognize and attack the cancer cells. Cancer immunotherapy has brought significant improvements for patients in terms of survival and quality of life. However, mechanisms that rules immunotherapy inefficacy in certain cases are still under study. [8]
6. Hormone Therapy: This treatment fights cancer by changing the amount of hormones in the body to treat certain types of cancer that depend on these chemicals

to grow and spread. This treatment is mainly used to treat breast and reproductive system cancer. Side effects are related to the type of cancer, age, sex and type drugs used in the treatment.

As well as others: Targeted drug therapy, Cryoablation and Radiofrequency ablation which are not described here for sake of brevity.

1.1.1 Historty of Radiation therapy

The gift of radiation therapy to medicine came with an experiment by Wilhelm Conrad Röntgen, a professor at Würzburg University, who discovered in 1895 what he first called X-rays. Experimenting with different material, he noticed that these seemed to be opaque in a different manner with respect to the rays that were coming from his source apparatus. He attributed this behaviour to the properties of the material, mainly to the density. [9] The possible use of the discovery in medicine was made clear by the iconic X-ray picture of his wife's hand, where bones appeared opaque while flesh transparent.

The first attempt to treat cancer by X-rays is disputed between Victor Despeignes, a young French doctor which is believed to have tried a treatment of a patient with stomach cancer in 1986, and Emil Grubbe, a student at the Hahnemann Medical College of Chicago that supposedly tried to treat a patient with breast cancer. [10] However, the first successful treatment that is documented is attributed to Leopold Freund an Austrian radiologist who treated a five-year-old patient with *Naevus pigmentosus piliferus* in Vienna just months after the discovery of X-rays by Röntgen. [11]

The continuous breakthrough of new technologies shaped the photon therapy field to the one known to date. Meanwhile, for five decades starting in the 1920s, experiments in particle physics constantly required higher energies driving the necessity of new accelerating machines such as cyclotrons, proposed by Ernest Lawrence in 1930 and proton synchrotrons which proposal is attributed to Marcus Oliphant (1943). [12]

After second world war, in 1946, Robert R. Wilson who was working primarily at the Radiation Laboratory (currently the Lawrence Berkeley National Laboratory) was asked to perform radiation shielding calculations for proton beams. [13] During this work, Wilson concluded that the Bragg peak formed by a proton beam in a medium could be used for radiation therapy in the treatment of cancers, and he published a series of analytical results on this subject in the medical journal Radiology. [14]

The first patients were subsequently treated in 1954 at Lawrence Berkley National Laboratory (LBL) and in 1957 in Uppsala, Sweden. With progressing technical advances in imaging, computers, accelerators and treatment-delivery techniques, proton therapy became more accessible to the routine medical treatment of cancer patients in the 1970s and was approved as a therapy option for certain tumours by the Federal Drug Administration (FDA) in 1988. The first hospital-based oncological particle centre that opened in 1989 was Clatterbridge Centre for Oncology in the United Kingdom, followed in 1990 by the Loma Linda University Medical Center (LLUMC) in the United States.

Ions therapy has its origins between 1935 and 1938 when John H. Lawrence, an American physicist and physician conducted the first biomedical studies and demonstrated the greater biological effect by dense tissue ionisation of heavy particles in normal and

cancerous tissue. In the following years, he demonstrated the therapeutic advantages of heavy-charged particles with higher energy together with Cornelius A. Tobias, a nuclear physicist and member of LBL best known for his radiobiological studies and application of the high Linear Energy Transfer (LET). Since 1952, the very first patients were treated with argon, neon, silicon and helium-particle beams until carbon ion was found to have the ideal radiobiological characteristics. The Bevalac, a 1974-onward combination of the Super Heavy Ion Linear Accelerator (SuperHILAC) linac and the Bevatron, a proton accelerator, enabled clinical trials with heavy ions of more than 1,400 cancer patients at what is now LBL before it was decommissioned in 1993.

1.1.2 Advantages in hadron therapy

In addition to traditional cancer treatments such as surgery, chemotherapy, immunotherapy and classical radiation therapy, during the last 60-70 years hadron therapy emerged as a new field in radiation therapy. In particular it demonstrated to be a key option for treatments of pediatric solid tumours, tumours of the brain, skull base, spinal cord, upper respiratory tract, chest, pelvic and others [15].

As mentioned above, while Classical Radiation Therapy (CRT) uses ionizing X-rays beams (high energy photons), hadron therapy treats cancer by mean of beams of hadrons, which are non-elementary particles such as protons or heavy ions, like fully stripped carbon ions, that is a carbon atom without any electron around the nucleus. Other particles such as neutrons, charged pions, antiprotons, helium, lithium, oxygen and silicon ions are more rarely used or planned to be used in future treatments).

The advantages of using hadrons instead of X-rays are well depicted by Bragg curves [16], named after William Henry Bragg, these graphs plot the energy loss rate, or LET as a function of the distance through a stopping medium (described by the Bethe-Bloch formula). As a result of physical properties, both of the particle and the stopping medium, Bragg curves have a peculiar shape that often shows a peak, called Bragg peak (see Figure 1.1). A quantity similar to the LET is the dose, which expresses the amount of energy released by the radiation when interacting with matter (energy per mass).

As can be seen from Figure 1.1 X-rays deposit the maximum dose in shallow regions while hadrons can reach deeper tissues. Furthermore, X-rays release a non negligible radiation dose beyond the target increasing the probability of damaging healthy tissues. These damages can lead to secondary malignancies. In contrast, protons and carbon ions deposit only a negligible amount of energy in the exit region (after the peak). A small dose is deposited in the entry region (before the peak), however it is still much less dangerous than the effect that X-rays have in the same region. Therefore, hadron therapy proved to be better than CRT especially if tumors are positioned deeper in the body and it is necessary to spare OARs. Thus, hadron therapy aims at improving the expected quality of life of the patient after the treatment.

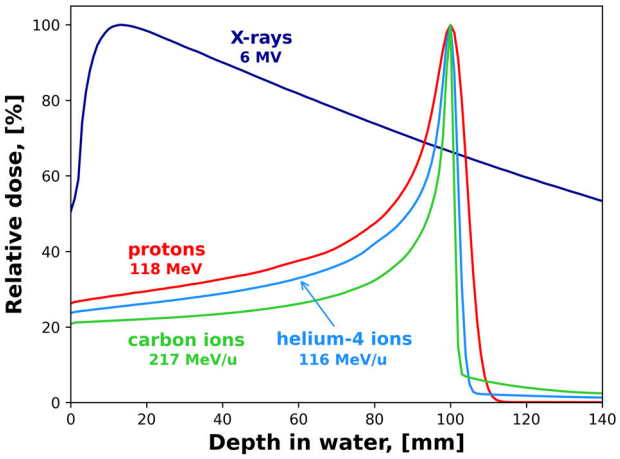

Figure 1.1: *General Bragg curves of photons (X-rays), protons, helium and carbon ions (by courtesy of Kristaps Palskis, RTU.)*

The main reasons behind the choice of carbon rather than other atoms are:

- an higher LET that translates in higher Relative Biological Effectiveness (RBE), the ratio of biological effectiveness of one type of ionizing radiation relative to another, given the same amount of energy deposited.
- a higher density of ionization in the treated volume, that means that ionizing radiation has an higher chance of breaking both strands of the DNA inside the tumor cell eluding its self repair capability,
- a damage non related to oxygen radicals, making the treatment suitable in case of hypoxic regions of the tumor, allowing to treat so called "*radio-resistant*" tumors.

The figures of patients treated with proton and carbon therapy through the years 2007 - 2021 are reported in Figure 1.2 (extrapolating hadron therapy data from [17]). As can be seen from the figure the number of patients is increasing which can be related both to the increase of people needing treatment but also from the availability and improvement of facilities that provide treatment.

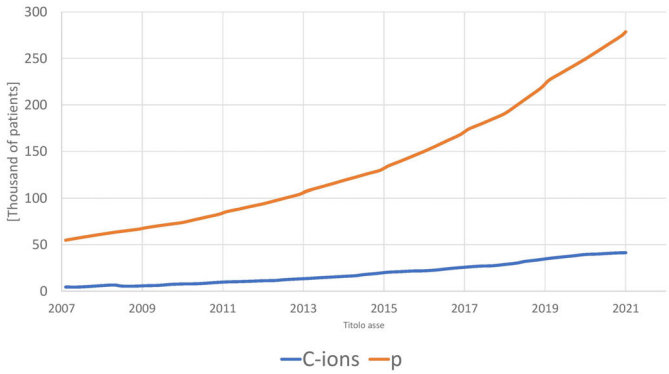

Figure 1.2: *Cumulative number of patients treated by C-ions or protons in the period 2007-2021 worldwide. [17]*

1.2 The gantry: brief state of the art

The beam necessary for treatment is generated from ion sources, gets accelerated either in a cyclotron or synchrotron to then be transported to the patient through a so called *"transfer line"*. The transfer line can be fixed horizontally, vertically or can rotate. In the last case, the transfer line must be supported by a robust machine called *"gantry"*.

The ability to reach the tumor from different directions is relevant for a number of reasons: to spread the dose over the volume of the tumor, to minimize the dose in the entry region (the same dose is spread on different entry angles) and to deliver the beam reducing the risk of damaging organs that are either in the proximity of the target volume or between it and the entry point of the beam.

Technically this can be achieved either by rotating the couch, on which the patient lays, with respect to a fixed beam or by rotating the beam around the patient. The latter is by far favored by the medical community, one of the main argument being the preservation of the treatment precision. This is because organs are subject to displacement when the body is subject to accelerations that are needed to rotate the couch. In such case the relation between the real position of organs and tumor at the time of the treatment and the known position acquired during the imaging process can be lost.

Gantries can be classified as isocentric if the isocenter is always in the same position or excentric if the isocenter rotates around the rotation axis of the gantry (see Figure 1.3 for a schematic). Because of the mentioned above preferences from the medical community and the lower risk of target movements, all commercial gantries are isocentric. In practical terms, both in isocentric and excentric gantries, the beam needs to bend from the longitudinal direction to a direction perpendicular to the rotational axis, this is done thanks to the Lorentz force generated in dipoles (curved objects in Figure 1.3).

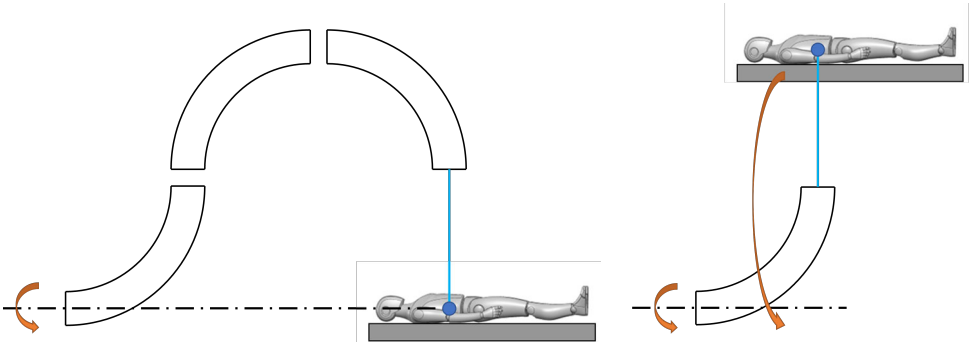

(a) *Iso-centric gantries.* **(b)** *Excentric gantries.*

Figure 1.3: *Schemes of isocentric and excentric gantries, in which the dot-dashed line represent the axis of rotation of the gantry in the isocentric case and for both the gantry and the patient in the excentric one. Note that the patient remains in a supine position during its rotation. The bent objects are dipole magnets.*

An additional classification of gantries is based on the technology used for the dipoles of the transfer line: dipoles can be normal conducting or superconducting if the coils cable is made of a superconducting material. Gantries are classified normal conducting or superconducting respectively.

To May 2022, a total of 185 gantry treatment rooms were operational, USA had 88, Europe 42 and Japan 31 [17]. As can be noted from Figure 1.4, the vast majority are proton gantries (182) while only three are C-ion gantries. Although gantries have been developed independently by some institutions like PSI in Switzerland and HIT in Heidleberg, the majority of gantries are commercial. While the market of commercial heavy ion gantries is still quite small, with only TOSHIBA (2 gantries in operation) [17], the market for proton gantries is well established and shared between multiple companies such as: IBA, Varian, HITACHI & MITSUBISHI (HITACHI acquired MITSUBISHI Electric particle therapy system in 2017), MEVION and others. See Figure 1.4 for the world distribution of commercial and non commercial gantries. The trend for Europe and Japan is to mainly buy from local companies (IBA or HITACHI respectively) while USA marked is shared between local and foreign companies. Most of the companies offer solutions using normal conducting gantries. An American company, ProNova, and TOSHIBA appear to be the only to offer superconducting gantries. An exceptional case is represented by MEVION, which offers a solution with compact superconducting synchrocyclotron mounted directly on the rotating structure.

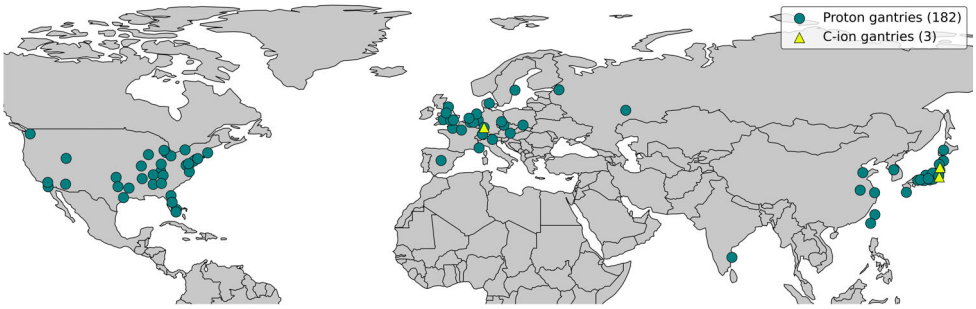

Figure 1.4: *Distribution of proton facilities using main commercial gantries. The number of treatment rooms operational to 2022 for main companies is reported between brackets.*

Table 1.1: *Classification of the main gantry models and their most relevant characteristics, data up to 2022.*

Company	Model	Number	p/C-ion	Technology	Length	Radius	
Varian	ProBeam	33	p	Normal conducting	10	5.25	m
IBA	Proteus®ONE	16	p	Normal conducting	9.5	3.6	m
IBA	Proteus®PLUS	52	p	Normal conducting	-	-	m
ProTom	Radiance 330®	1	p	Normal conducting	10	4	m
MEVION	S250i™	8	p	Superconducting	11	4.2	m
ProNova	SC360	5	p	Superconducting	5	4	m
Hitachi	PROBEAT-V	10	p	Normal conducting	11	5.5	m
Hitachi	PROBEAT-RT	7	p	Normal conducting	8	4	m
SHI	-	6	p	Normal conducting	4.6	4.5	m
Private	PSI 1	1	p	Normal conducting	11	2	m
Private	PSI 2	1	p	Normal conducting	11.6	4.2	m
Private	HIT	1	C-ion	Normal conducting	25	6	m
TOSHIBA	-	2	C-ion	Superconducting	13	5.45	m

The scarce number of C-ion gantries with respect to proton machines is related with the high cost of facilities. On the cost list one of the most impacting voices is the size of the gantry, which translates in a bigger gantry hall, that by default needs robust shielding walls (up to 6 m thick). That high cost is then given by the civil engineering of the hall. Another factor can be the market monopoly on C-ion gantries ruled by TOSHIBA, because the competition in a market is fundamental to improve technologies and lower costs to users, as demonstrated in many other examples in history.

1.2.1 Superconductivity

Key components of the transfer line are the dipole magnets (or bending magnets) that allow to bend the beam taking it from the accelerator complex and directing it to the target volume (tumor). Bending the beam allows to take it from the axial direction to a transversal direction. This, coupled with the rotation of the gantry and of the couch where the patient lays, allows in theory to reach the target from any direction. The bend

is possible thanks to Lorentz force $\mathbf{F} = q(\mathbf{E} + \mathbf{v} \times \mathbf{B})$ where q is the electric charge of the particle composing the beam, $\mathbf{E}$ the electric field in the region, $\mathbf{v}$ the velocity and $\mathbf{B}$ the magnetic field in the region. The magnetic field $\mathbf{B}$ generates a force that is perpendicular to the direction of motion of the particle, thus bending its trajectory. One figure of merit of dipoles is the beam rigidity [18]:

$$B\rho = 3.33564\frac{A}{Z}p \tag{1.1}$$

where B is the magnetic field strength (in [T]), ρ the radius of curvature of the trajectory (in [m]), A is the atomic mass, Z is the charge state of the particle and p is the momentum of the particle measured in [GeV/u/c].

Taking the numbers in Figure 1.1 for the momentum of protons and carbon ions ($Z = 4$) necessary to have a Bragg peak at the same depth, the beam rigidity is much greater for carbon ions.

A keystone for a lighter and compact C-ion gantry is the application of superconducting technologies [19] in the design of the magnets of the transfer line. This is reflected in the size of gantries reported in Table 1.1. The 90° dipole of the first normal conducting C-ion gantry has a mass of about 70 t and provides about 1.8 T [20, 21]. The last bending section of the gantry layout studied in this work has a mass of only 3.2 t and provides about 4 T, allowing to reduce the curvature radius thanks to the higher magnetic field, reducing the overall size of the machine.

1.3 Aim of the thesis

This thesis aims to develop a novel method for the optimal mechanical design of supporting systems for a cryogenic device under variable loads.

The specific case of superconducting magnets on a rotating gantry for medical applications serves as a case study to use for the first time the developed tools, with the goal of achieving an optimal design for the supporting system.

The mathematical models developed in this thesis are applicable to supporting systems consisting of six or more thin supports, of any geometry and material but joined at each end by spherical or universal joints, inhibiting the development of internal actions other than the axial component. The models are applicable at supports that can exhibit a thermal gradient through the supports. The models have been validated by comparing the predictions with those of standard finite element simulation software and not through testing campaigns as the cost of a full scale system is estimated around two millions of Swiss francs, and a simplified scaled down version around 100,000 Swiss francs.

1.4 Research plan of the thesis

To develop an optimal solution for a cryogenic device subjected to variable loads, i.e. the superconducting dipole of the gantry, this thesis is structured around the following tasks:

1. reviewing the literature on existing supporting systems for cryogenic devices, identifying their characteristics, common design approaches, and research gaps worth

exploring;
2. proposing different supporting architectures to ensure a comprehensive study of the problem;
3. defining the requirements and load cases for the supporting system under variable loads;
4. developing general mathematical models to analyze supporting systems under variable loads;
5. establishing relevant criteria for comparing different support system designs;
6. designing and optimizing each supporting system by selecting its architecture, material, and geometry;
7. evaluating the proposed solutions against the defined criteria.

1.5 Scientific novelty and practical applications

The scientific relevance of this work lies in its contribution of new knowledge to the field, as it introduces a simplified model that thanks to limited set of parameters can be used by a wider community of designers and engineers, allowing to achieve accurate results almost independently from the level of expertise that is instead highly required to run accurate Finite Element Analysis (FEA). The models, with their few relevant parameters offer an higher insightfulness into the behavior of the complex system, thanks to which designers and engineers can have a faster and clearer grasp on the influence of relevant parameters on crucial output quantities, boosting the capability to choose optimal configurations of supports before running computational expensive FEA. Additionally, a reduction in computational cost of running the model instead of FEAs can lead to machine based optimizations routine, able to improve performances of supporting systems of cryogenic devices. Moreover, the introduction of an exactly constrained architecture for the first time in the field can be used to implement automation, demonstrating its applicability in cryogenic environments. This has the potential to affect accelerator uptime reducing the impact of realignment campaigns, or increasing the online response to changes in external conditions (i.e. temperature). Not of second importance, this research can have a significant impact on hadron therapy technology, with a first application of the thesis results as major contribution to the European project Heavy Ion Therapy Research Integration plus (HITRI*plus*) [22]. Future practical applications may include medical imaging systems and various other fields, such as superconducting generators for wind turbines, superconducting radio frequency cavities, optical alignment systems for cryogenic devices in high-energy physics experiments, and satellites, all contributing to societal advancements.

2 LITERATURE ANALYSIS OF SUPPORTING SYSTEMS FOR CRYOGENIC DEVICES

The standard superconducting materials commonly used generally need to be cooled down to extremely low temperatures, in most cases down to $1.8 - 4.5\,\mathrm{K}$. The extraction of heat from the superconducting body, often referred to as the *"cold mas"*, becomes more expensive the lower the temperature the body needs to be maintained at. Moreover, every connection between the cold mass and the room temperature environment represents a bridge for heat to flow into the body, warming it up. Nevertheless, a minimum number of connections is necessary for the superconducting element to be functional. The supporting system is one of these, having the primary function of maintaining the cold mass in the nominal position and orientation. The most common applications of cold mass supporting systems are those associated with magnets or radio frequency cavities.

On one hand, the supports of the cold mass must be designed to guarantee the mechanical resistance to the loads the machine may experience during its operation: nominal loads, seismic loads, transportation loads, and loads due to malfunctioning events. Hence, as a rule of thumb, the larger the cross-section of the support, the lower the stress and the higher the safety factor over the mechanical resistance.

On the other hand, the larger the cross-section, the larger is the heat load to the cold mass flowing through the support. Therefore, the design of the supporting system is the subject of trade-offs and optimizations. As a result, engineers have developed a number of solutions that show recurrent patterns both with respect to geometrical architectures and materials used.

The aim of this chapter is to give an overview and classification of the solutions that have been adopted to solve this specific engineering problem.

2.1 Literature analysis methodology

The Open Access database used for searching scientific articles is connected to the Google Scholar browser [23]. The time frame has been limited to the most recent results available as of February 2023. Search operators were used to refine the research as follows:

- The "*word*" operator is used to include a specific word or sentence in the search;
- Parentheses, AND, and OR operators follow the common Boolean algebra;
- The ∼ operator allows the browser to search for synonyms of a word;
- The - operator excludes a word from the results;
- The intitle: operator forces the browser to find results that contain a specific word in the title;

The search field was established using the keywords listed in Table 2.1 combined with the aforementioned operators in the following string: *"FEA" AND "superconducting" AND "cold mass" AND "mechanical" AND (∼support OR ∼suspension) -ATLAS -CMS -intitle:"LHC"*. The keywords ATLAS and CMS were excluded to avoid repeated articles

in the results citing two of the most well-known physics experiments. Additionally, the keyword LHC was removed from the title to avoid publications related to LHC supports. Results related to these were included manually. The search yielded 194 results, which were viewed searching for images of the supporting system, its description and FEA results. Whenever the content of a found article was incomplete, related publications were searched.

Table 2.1: *List of keywords used in the search and their descriptions.*

Keyword	Description
FEA	Filters results in which the supporting system has been analyzed using Finite Element Analysis.
superconducting	Sets the search field to superconducting technologies.
cold mass	Highlights the interest in cold mass supports.
mechanical	Filters for mechanical analysis rather than just general physics analysis.
support	Sets the search field to the supports of a superconducting element.
suspension	Synonym for "support."
ATLAS	Avoids repeated articles in the results citing one of the most well-known physics experiments (included manually afterwards).
CMS	Avoids repeated articles in the results citing one of the most well-known physics experiments (included manually afterwards).
LHC	Avoids the many publications related to LHC supports (included manually afterwards).

This literature analysis aimed to highlight the following characteristics of the supporting system:

- The architecture, i.e., the arrangement of supports with respect to the superconducting body.
- The geometry of the single supporting element of the supporting system.
- The materials used for the supporting element.
- The characteristics of the supported body, such as its mass and length.
- The cool-down effect, i.e., the kinematic behavior of the architecture when the superconducting body undergoes a thermal cycle.
- The adjustability and classification of the adjustment system.

The most relevant results have been reported and analyzed in the following section.

2.2 Results of the analysis

The book "Cryostat Design" [24] provides a comprehensive review of cryostat design principles, offering practical data, equations, and case studies of some existing cryostats. In contrast, this review focuses solely on the supporting system for the cold mass. It

complements the previously presented case studies with new ones and, in the following sections, presents a classification of suspension architectures.

2.2.1 The "multi-post" architecture and geometry

The so-called "multi-post" architecture (represented in Figure 2.1) consists of two or more posts arranged vertically with respect to gravity and radially with respect to the supported body. The posts geometry consists of thin-walled cylindrical tubes serially interfaced with the various heat intercepts.

This architecture has been found in the magnet feeder system of ITER [25, 26], the cryodipoles and SSS of LHC [27, 28], the cryomagnets of RHIC [29], the cryomagnets of SSC [30], and the linac cryomodules of LCLS-II [31]. While for the majority of the supporting systems, the posts are placed on the bottom side of the cold mass, in LCLS-II, these are placed on its upper side.

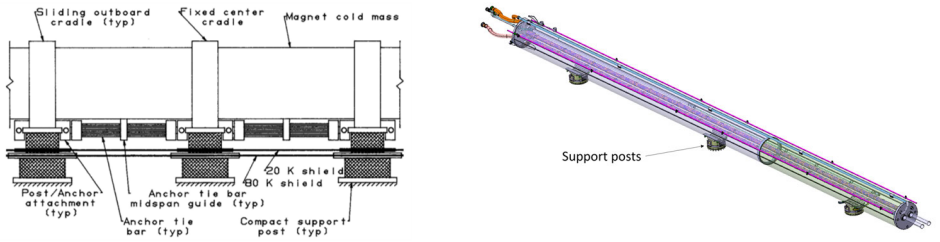

(a) **(b)**

Figure 2.1: *Example of the "multi-post" architecture for the supporting system of superconducting bodies. (**a**) represents the lateral view of three of the five supporting elements originally designed to support the SSC cryodipoles (Reproduced with permission from T. H. Nicol et al. SSC Magnet Cryostat supporting system Design; published by Springer Nature, 1988, [30]). (**b**) illustrates the arrangement of three supporting elements for the cryodipoles of the LHC.*

2.2.2 The "8-support" architecture and geometry

The so-called "8-support" architecture (represented in Figure 2.2) consists of eight supports arranged in sets of four at each end of the supported body in a symmetric pattern with respect to origin planes (with the origin at the centroid of the supported body). This architecture has been found in both the criss-crossed pattern (Figure 2.2b) and the non-concurrent version (Figure 2.2a and Figure 2.2c). Mainly two geometries have been found for the supporting element in this supporting system: the rod support (Figure 2.2a) and the so-called double-band support (Figure 2.2b and Figure 2.2c). The former consists of a rod, eventually split by the heat intercept, while the latter consists of racetrack-shaped elements connected by a linking element, to which the heat intercept is joined. The linking element consists of two pivots that allow a rotation of the bands with respect to each other.

The 8-rod architecture has been found in the quadrupole doublets of FAIR [32, 33] and the coils of an MRI at NeuroSpin [34, 35]. The 8-double-band supporting system has

been found in the analytical paper from CAS [36], the wiggler of TLS [37], the wiggler of IHEP [38], the coupling solenoid of the MICE [39], and the undulator of SSRF [40, 41].

The reasons why, in some designs, the double-band geometry has been preferred over the rod one have not been explicitly reported in the articles analyzed in this literature analysis. There could be a correlation with the behavior of the material used with respect to the shape chosen, more details will be added to this topic in the material and discussion sections.

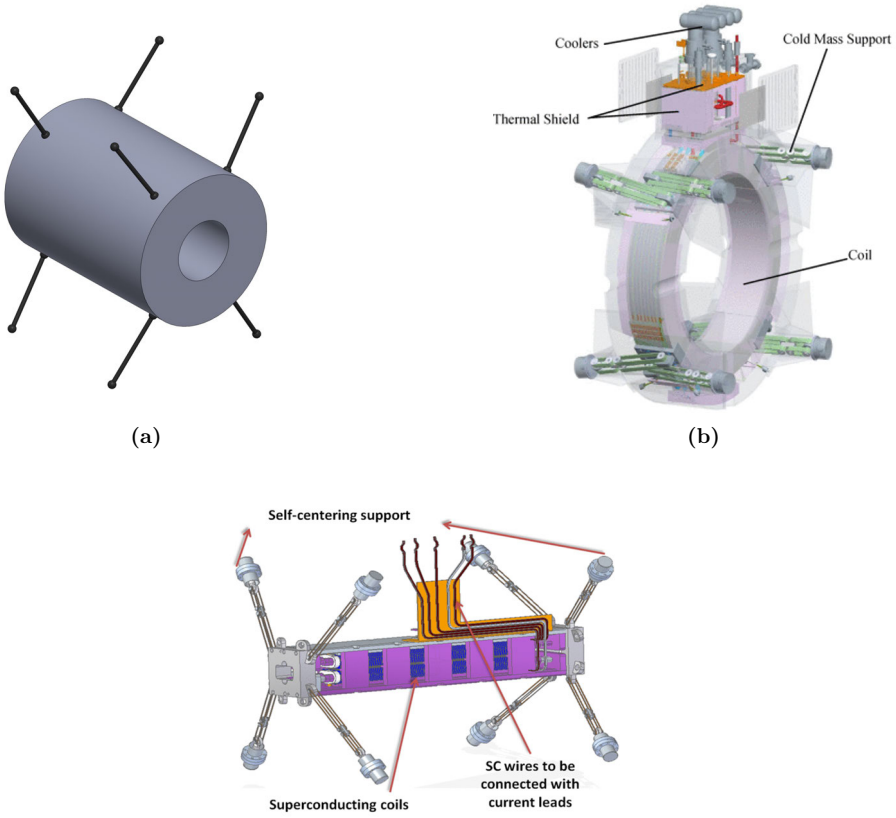

(a) **(b)**

(c)

Figure 2.2: *Example of the "8-support" architecture for the supporting system of superconducting bodies. In (**a**) you can see a schematization of the eight rods supporting the main coil of NeuroSpin MRI; (**b**) shows the eight double band suspension of the coupling solenoid of the MICE experiment [39] (Copyright 2011, by IEEE. reproduced with permission); in (**c**) are represented the eight double band supports of the superconducting undulator developed at the SSRF [40] (Copyright 2015, by IEEE. reproduced with permission).*

2.2.3 The cavity architecture and geometry

The cryomodule for cavities often contains a string of them. These can be individually supported or interconnected. Additionally, most designs benefit from the double-walled tube of the FPC to react to part of the loads, acting as a post.

For elliptical cavities of ESS (Figure 2.3a), a criss-cross 8-rod + 1 pseudo-post architecture has been found [42, 43]. In this case, the FPC tube is left free to slide in its axial direction to allow for thermal contractions.

A 22-rod + 2-posts arrangement has been found for the spoke cavities cryomodule of ESS (Figure 2.3b) [44–46]. The 22 rods are distributed on two individual cavities: eight in the criss-cross "8-support" architecture, for each cavity have used to react lateral and vertical loads; two axial rods for each body and two rods interconnecting the two cavities have been used to control the relative and absolute axial alignment. The FPC is used as a post for each cavity partially reacting loads.

The novel architecture chosen for crab cavities of HL-LHC [47, 48] is composed of one post and two flexure blades (Figure 2.3c). In the same way as for other superconducting cavities, the FPC is used as a post support, while two flexure blades have been added to stiffen the system.

An original architecture for cavities has been proposed in the framework of SPL studies (Figure 2.3d) [49, 50], where the FPC acts as a classic post at one end of the cavity, while two Inter-Cavity Support (ICS) have been used as stiffeners. These are left free to slide longitudinally while still transferring the vertical load to the next cavity. The alignment of such architecture could be not trivial on the side of ICS. The studies related to SPL stopped before the experimental phase.

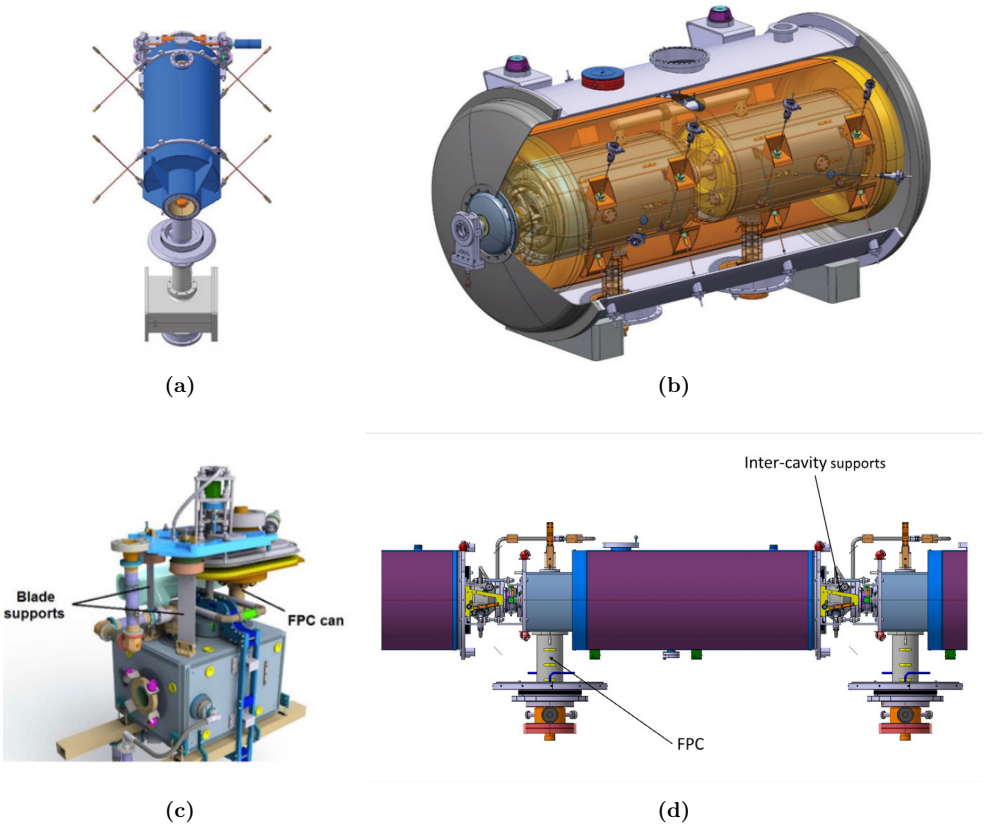

(a) **(b)** **(c)** **(d)**

Figure 2.3: *Example of cavity architectures. In (**a**) is represented the suspension architecture of elliptical cavities of ESS [43]; (**b**) is a representation of the supports of spoke cavities of ESS [45]; (**c**) illustrate the architecture of supports of crab cavities for the HL-LHC [47]; (**d**) is a drawing of the supporting system of SPL.*

2.2.4 Other architectures

Other "exotic" solutions have been found in the literature; these can be associated with the non-standard shape of the cold mass, its dimensions, weight, available space around the assembly etc.

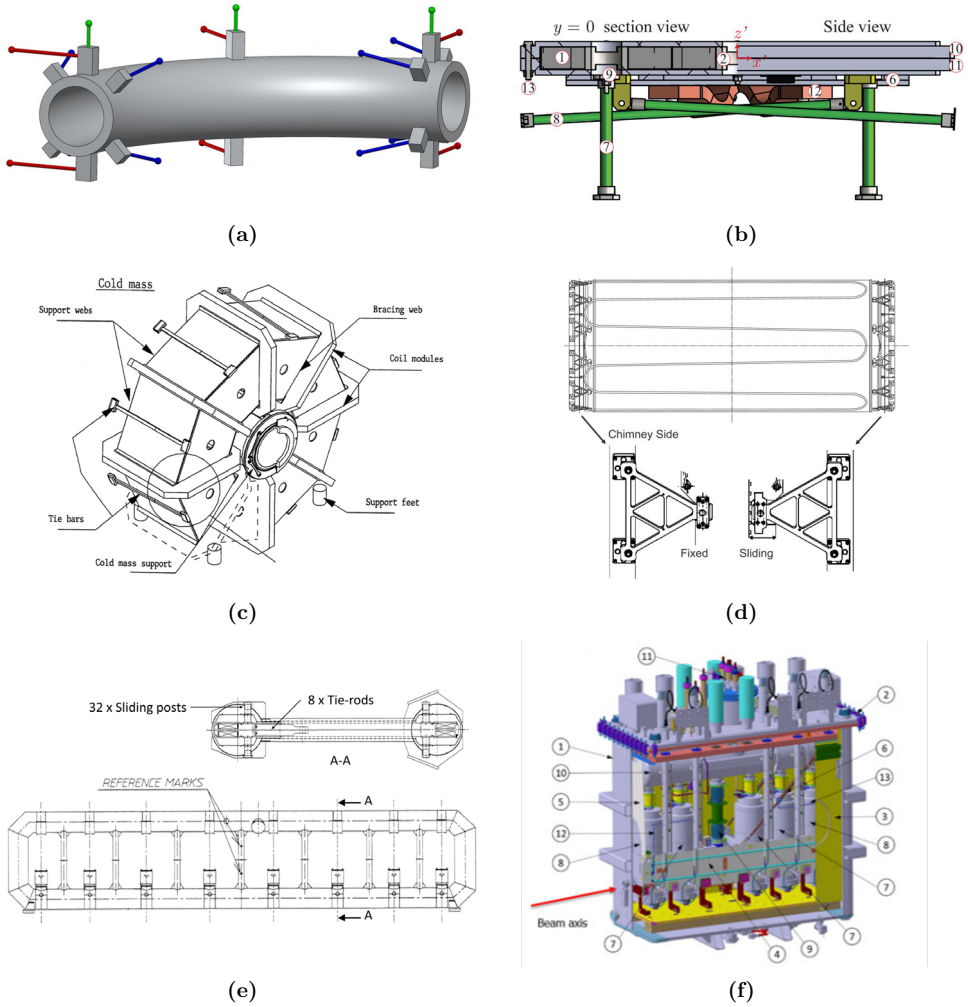

Figure 2.4: *Example of* "exotic" *suspension architectures. In (**a**) you can see the 14 rods + 3 spring (green) scheme of the supporting system of the transport solenoid of the Mu2e experiment (the original image can be found in [51]); (**b**) shows the supporting system for a magnetic density separator [52]; in (**c**) you can see the 16 tie bars and 4 gravity supports of the end cap toroid magnets [53]; in (**d**) is illustrated the 24 triangle supporting system of the central solenoid (Reproduced with permission from A. Yamamoto et al., The ATLAS central solenoid; published by Elsevier, 2008 [54]); (**e**) shows the 8 tie rods and 32 cryogenic stops of a single barrel toroid coil of ATLAS [55]. in (**b**) is represented the supporting system within HIE-ISOLDE cryomodule [56]*

A 17-rod architecture has been chosen for the transport solenoid of the Mu2e experiment (Figure 2.4a) [51, 57]. In this case, a set of four axial rods has been arranged at each end of the cold mass, three couples of radial rods have been distributed over three positions of the transport solenoid, to which one vertically spring-loaded rod has been connected.

A 4-rod + 4-post architecture has been proposed for the magnetic density separator studied at UT (Figure 2.4b) [52]. The four posts are arranged vertically at each corner of the coil, while the four rods follow a criss-cross pattern.

Highly tailored designs have been used for the supporting system architectures of the magnets of the ATLAS experiment at LHC (grouped in Figure 2.4): a combination of 16 tie rods and four gravity supports have been used for the end-cap toroid magnet (Figure 2.4c) [53, 58, 59]; eight tie rods and 32 cryogenic stops have been arranged over the length of each barrel toroid coil (Figure 2.4e) [55, 60, 61]; 12 triangular struts support the central solenoid at each end (Figure 2.4d) [54]. The central solenoid supporting system experiences a thermal gradient between the cold end and the warm end lower than the usual thermal jump of $294 - 296\,\mathrm{K}$ that other supporting systems have to comply with.

The supporting system of the solenoid of the CMS experiment at LHC consists of 30 tie rods: nine axial rods per each side of the magnet, four vertical, and eight radial [62].

The supporting system of the cold mass within the cryomodule of HIE-ISOLDE (Figure 2.4f) [56, 63] consists of two end plates fixed at each end of the support frame and to two separately actuated struts connected to the top plate of the vacuum vessel. Additionally, one tie rod per side is connected on one end to the support frame by means of elastic washers, while the other end is connected by means of a spherical joint with respect to the actuated strut.

The gravity support in the conceptual suspension architecture of DEMOnstration power plant (DEMO) [64], based on the ones designed for ITER, [65, 66] consists of an assembly of 21 flexible plates clamped in parallel and spaced apart by spacers (multi-blade support). Supports are placed so that the plates have their minor bending stiffness in the radial direction of the tokamak. While ITER has 18 gravity supports equally distributed at the bottom of the toriodal coils, DEMO is expected to have 16 of them. Additional internal suppports link adjacent toroidal coils, central solenoid, and poloidal field coils.

A four single-band suspension system has been designed built and tested to support a warm bore High Temperature Superconducting (HTS) steering magnet at the Variable Energy Cyclotron Centre (VECC) [67]. Each support can rotate around a pin joint at both ends.

An eight-pillar support architecture have been proposed to suspend a HTS quadrupole magnet for a proton cyclotron beam line studied at CAS [68]. Each composite rod appears to be fixed at each end.

2.2.5 Intermediate structural elements: common girder and space frame

Some designs include the use of a common girder, as done for the quadrupole doublets of FAIR [32, 33], or a space frame, as found for the cryomodule of elliptical cavities of ESS [42, 43] (see Figure 2.5). Both the common girder and the spaceframe are used to add a rigid intermediate structure between multiple cold masses and the cryostat. Adjustments of the pose (position and rotation) of the cold masses with respect to each other can be more easily done with this sub-assembly outside of the cryostat, as there is more open space for manual operations. Afterwards, the sub-assembly can be slid into the cryostat.

On one hand, as can be seen from Figure 2.5a, the common girder becomes itself part of the cold mass. Therefore, all the challenges related to the suspension of a cold body

with respect to the external room temperature environment remain. Hence, the 8-rod criss-crossed architecture has been chosen.

On the other hand, the space frame (Figure 2.5b) is closer to the external conditions in the thermal chain; normal adjustable jacks have been distributed along the cryostat to support the space frame. The supports between it and cold masses need to be addressed as well. For instance, the 8-rod criss-crossed architecture has been chosen to suspend the four elliptical cavities within the space frame, while the FPC locks longitudinal movements and is left free to slide along its axis.

Therefore, common girders and space frames do not represent a stand-alone solution. A suspension system similar to the ones mentioned in previous sections is needed. These intermediate structures are mostly used to allow precise alignments of a set of cold masses with larger manipulation freedom while reducing the number of penetrations of the vacuum vessel.

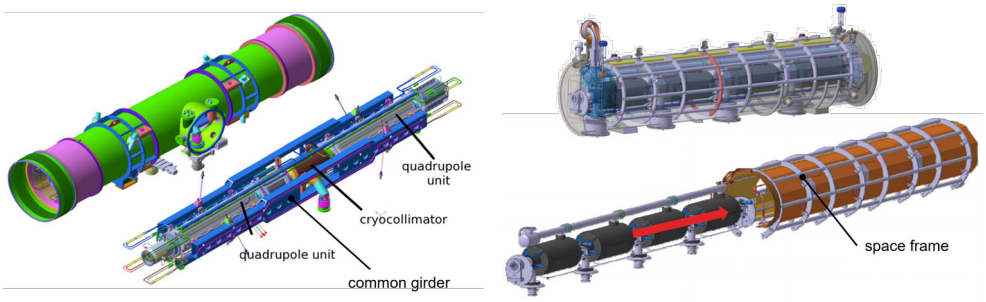

(a) **(b)**

Figure 2.5: *Example of multiple sub assemblies common cryostat suspension architectures. In (**a**) you can see the common girder of the quadruple doublets of FAIR Synchrotron [32]; (**b**) shows the space frame that supports four elliptical cavities of ESS (Reproduced with permission from Darve, Christine; Bosland, Pierre, The ESS elliptical cavity cryomodules; published by AIP Publishing, 2014 [43]).*

2.2.6 Other remarks on results and gantry results

Multiple designs with different shaped struts have been studied to support a modular HTS pole coil of wind power generators [69–72]. The structural mechanical design has not been motivated completely. The addition of a high number of supports, if compared to cold masses of a similar size, allows the redistribution of the high torque. The study of extra stress during the cool-down has not been reported, while it should be critical in these designs since the suspension struts are stiffer than in other reported applications. Additionally, since these suspension systems are related to power generation devices, less care than in other cases has been used to minimize the conduction heat loads. For the reasons just mentioned, these designs have not been added to the summary table.

A conceptual design of a HTS magnet for a particle physics experiment in space have been done in collaboration with CERN [73–75]. Space applications do not require vacuum insulation and a classic cryostat. The change in boundary conditions results in an

incoherent comparison of the structural supports of this application with other suspension systems described in this review.

The support architecture of references [76, 77] could not be classified due to the lack of reported information.

The string *"FEA" AND "superconducting" AND "cold mass" AND mechanical AND (∼support OR ∼suspension) -ATLAS -CMS -intitle:"LHC"* has been integrated with *AND "gantry"* to target the research field of rotating machines in medical applications. No relevant results have been found on supporting architectures in this field. Searching directly for supporting system of superconducting magnet on ProNova SC360 gantry also produced no results (search string: ProNova SC360 Gantry support, 42 results), with only optics or other general integration aspects being described [78–80]. Additional searches have been done in the "PATENTSCOPE" database of World Intellectual Property Organization (WIPO), a database that provides access to over 121 million patent documents. Patents applications related to ProNova have been searched (string "EN_ALLTXT:(ProNova SC360)", or the string "ProNova gantry"), no relevant results on the specifics of the design of the supporting system for the superconducting magnet have been found.

2.2.7 Materials used for the supports

The materials of the supports used in the architectures found are listed below:

- metallic materials: Ti-6Al-4V, Ti 5AL 2.5Sn ELI, SS316L, SS 316LN, AISI 304, Inconel® 718;
- composites: CFRP, G10, G11, G11CR, UFGE, GFRE, Ultem® 2100, SEl-GFN3 Noryl®.

The choice is usually guided by the ratio of heat conductivity and yield strength (the properties of some materials can be found in [81, 82]), which allow to comply with the requirements of minimal heat loads and proper mechanical resistance. Additionally, materials with low magnetic permeability are preferred to others in case of interference with the magnetic fields, which is true for almost all applications found.

2.2.8 Cool-down effects and adjustability

Two main strategies have been identified for managing the cool-down effects in superconducting systems, and these strategies depend heavily on the architecture of the supporting system. In structural mechanics, structures are classified as *statically determinate* or *statically indeterminate*. Statically determinate structures are defined as systems for which the number of equations match the number of unknowns, or physically, all the degrees of freedom of the system are exactly constrained. Usually in statically indeterminate supporting systems additional stress is present in the supporting elements during cool-down. While a statically determinate supporting system is free of extra stress during cool-down.

When using eight supports the supporting system is statically indeterminate, their symmetric arrangement can generate additional stress in the supporting elements during cool-down. However, this stress is accepted by design to promote a symmetric contraction of the superconducting body (E-SC in Table 2.4) so that the position of the supported

object remains unchanged. Therefore, the alignment strategy involves aligning the superconducting structure at warm temperatures and then relying on self-centering symmetric contraction during cool-down. However, minimal errors may arise due to the imprecise manufacture and assembly of the supports, which can cause them to be positioned asymmetrically.

The use of a "multi-post" architecture allows the system to cool-down without generating extra stress (N-AC in Table 2.4). The system is still overall statically indeterminate, but the system is compliant enough in some directions in order to accommodate the shrinkage of the cold mass. As a result, the pose of the magnet can change. Typically, one post is used as a fixed point while the others accommodate the contraction. The misalignment during cool-down cannot be ignored and must be estimated by accurate thermal analysis. The strategy is to intentionally misalign the pose of the suspended object, so that during cool-down it will translate within an acceptable range with respect to the nominal pose.

The N-AC behavior is also a characteristic of some mixed architectures that have been applied to superconducting cavities. For instance, in the case of crab cavities [47, 48], the flexure blades have been positioned with the blades tangential to an imaginary cylinder surface that shares the axis with the post. Thus, the radial contraction of the cold mass with respect to the post makes the blades bend in the plane with the least bending stiffness, generating little to no extra stress. The same cool-down effect has been achieved in SPL [49, 50] cavities with two ICS that are fixed to one cavity but free to slide and rotate with respect to the adjacent one, thus generating no extra loads during cool-down. The supporting system of the central solenoid of ATLAS [54], with one end fixed and the other able to slide, allows for no build-up of stress during cool-down. Hence, the centroid of the system is displaced longitudinally. In contrast, the presence of spherical bearings at the end of the triangular struts allows the system to preserve the radial position of the axis of the solenoid.

A potentially optimal solution that could benefit of a symmetric contraction without extra stress (N-SC in Table 2.4) has been applied to the quadrupole doublets of FAIR [32, 33]. This is claimed to be achieved by fine-tuning the geometry of the supporting system so that the contraction of the suspended body is coherent with the contraction of each support in terms of magnitude and direction, resulting in a symmetric contraction without extra stress. In addition to this, the contraction of the supports is fine-tuned by using two materials of different lengths and linear expansion coefficients for each of the eight supports. This is achieved despite the supporting system is again statically indeterminate.

The architecture applied to the barrel toroid coils of the ATLAS experiment [55] shows a de-stress behavior during cool-down. In fact, the tie rods have been pre-bent at room temperature to exhibit low to zero stress at cold temperatures. Moreover, the cryogenic stops have been designed to be split into two halves, allowing the cold mass to slide with respect to the vacuum vessel. Furthermore, placing the warm end of the tie rods within the coil envelope could allow the contraction of the coils and the rods to be coherent (both contract toward the horizontal symmetry axis of the coil, see Figure 2.4e). Therefore, to summarize, the system has been classified as de-stress and symmetric contraction (D-SC

in Table 2.4).

Adjustability is ensured at different interfaces of the assembly chain that goes from the cold mass to the assumed rigid ground. The following classification is based on the first adjustable link found in this chain. The position of the tuning link in this chain is often related to the support configuration. The "8-support" architecture usually utilizes the regulation of the warm end position of each support to adjust the pose of the suspended object. Thus, the tuning link is at the interface between the vacuum vessel and the support structures (SVI in Table 2.4). On the other hand, with a "multi-post" architecture, the regulation of the pose of the object is generally done at the interface between the vacuum vessel and the ground (VGI in Table 2.4). An example of this can be found in the alignment system of the cryomagnets in the LHC [83]. In most cases, if an SVI adjustable link is present, a VGI link is present as well. However, the opposite is not always true. Architectures that have been classified as pure VGI in Table 2.4 very often do not have an SVI link. Shims are not considered tuning links in this classification.

All of the adjusting systems found in the literature search are used during the initial assembly of the complex, tuning sessions or after maintenance, thus, classified as passive (P in Table 2.4). The suspension architecture of HIE-ISOLDE [56, 63] is coupled with an actuated system. However, there is no feedback loop with the position at cold of the suspended body, hence the architecture has been classified as passive.

2.3 Discussion

Table 2.2: *Description of the parameters used in Table 2.4.*

Parameter	Description
Ref	Relevant references related to suspension architecture design and description.
Project	Name of the project.
Element	Classification of the suspended cold mass.
SC material	Superconducting material and its raw shape used for the analyzed design.
Mass	Mass of the supported cold mass.
L1	First major dimension of the cold mass, generally in the longitudinal direction (curvilinear for Mu2e or height for tokamaks).
L2	Second major dimension of the cold mass, generally diameter.
Architecture	Suspension system elements and their classification based on geometry (i.e., post, band, rod, etc.).
Material	Material of the suspension elements.
Cool-down	Classification of the behavior of the support system during the cool-down, specifically related to the possibility of extra stress appearing in the supporting elements and to the influence of the thermal contraction on the misalignment of the cold mass.
Applicability	Evaluation of the possibility to apply the suspension architecture to support a cold mass that needs to be rotated.

Table 2.2: *Continuation.*

Parameter	Description
Adjustability	Classification of the adjustment/alignment system, based on its position in the assembly, the way of adjustment (passive or actuated) and the evaluation of its applicability to rotating cold masses.
Publication	Years of publication of the references.
Status	Status of the project at the moment of the publication of this article.

Table 2.3: *Summary of acronyms used for the parameters in Table 2.4 and their description.*

Parameter	Acronym	Description
Cool-down	E	Extra stress appears in the suspension system element due to cool-down
	N	No extra stress appears in the suspension system element due to cool-down
	D	The system gets de-stressed from an initial condition of pre-tensioned suspension system
	AC	The cool-down affects the position and orientation of the supported body in an asymmetric way, the architecture is not self-centering
	SC	The architecture is self centering during cool-down, there is no change in position and orientation of the cold mass
	ND	Not easily Deducible by these authors
Adjustability	SVI	The adjustment/alignment system is placed at the interface between the suspension system and the vacuum vessel
	VGI	The adjustment/alignment system is placed at the interface between the vacuum vessel and the ground
	A	The adjustment/alignment system is actuated
	P	The adjustment/alignment system is passive
	R	The adjustment/alignment system can be applied directly on a rotating machine with little R&D
	NR	The adjustment/alignment system cannot be applied directly on a rotating machine without R&D
Status	dev.	The system is in development
	const.	The system is in the construction phase
	comm.	The system is in the commissioning phase
	op.	The system is operational

Table 2.3: *Continuation.*

Parameter	Acronym	Description
	res.	The system is related to research, analytical calculations

The research on suspension systems for cold masses has resulted in more than 20 applications, ranging from accelerating cavities and cavity strings, wiggler magnets, magnetic density separators, solenoids, quadrupoles, dipoles, feeders, magnets for detectors tokamaks, and MRI. The mass of the suspended body varies from 160–225,000 kg, while the axial length varies from 0.3–25 m. The tokamaks have heights greater than or equal to 24 m, diameters of more than 30 m, and weights more than 23,000 t. The results have been reported in Table 2.4, a list of parameters used for the classification is given in Table 2.2, while abbreviations are listed in Table 2.3.

A few HTS applications have been found; in most of the cases these are related to innovative applications, such as wind power generators where the impact of heat loads is minimal if compared to the generated energy, thus less stringent requirements have been accepted. Two HTS magnet applications have been found, and no mention has been made of the necessity of a novel suspension system due to the adoption of HTS instead of standard low temperature superconducting technology.

Nevertheless, three recurrent suspension architectures have been identified: the "multi-post" architecture used mainly to suspend slender heavy bodies, for example, the cryomagnets of synchrotrons such as LHC, RHIC and SSC. These magnets are $10 - 17\,\mathrm{m}$ long and have a small diameter with respect to their length. This architecture aims to reduce the vertical sagitta without using many rods that would result in a high number of penetrations of the vacuum vessel. The "8-support" architecture is often used for relatively light or bulky bodies. The cavity architecture is used to support cavities by exploiting the tube wall of the FPC as a post together with extra stiffening structures. Other solutions deviate from the aforementioned due to geometrical reasons, such as the high curvature of the Mu2e transport solenoid, the pancake shape of the magnetic density separation device, or the geometry required by magnets used for particle detectors. Although they do not represent a standalone suspension solution, intermediate structures such as common girders and space frames placed between the vacuum vessel and the suspended body help with the management of modular assemblies and alignment procedures of multiple cold masses. In these cases, a suspension architecture is still necessary, and the associated challenges remain unchanged.

Common behaviors with respect to the cool-down process have been classified. Depending on the architecture, extra stress can develop in the supports in exchange for a more accurate pose (position and orientation) of the body after the cool-down. In different architectures, a reproducible asymmetric contraction of the system has been accepted in exchange for low to zero extra stress on the supports. Although more complex, a possible optimal solution has been identified in the architecture of FAIR, this could be based on careful tuning of the materials and geometry of the supporting system to achieve both desirable cool-down characteristics: a symmetric contraction without extra stress.

Table 2.4: *Summary table of the researched suspension system for superconducting elements. The main characteristics have been reported and classified following the nomenclature reported as notes below the table. Results have been ordered by increasing weight of the cold mass.*

Ref.	Project	Element	SC material	Mass kg	L1 [a] m	L2 [b] m	Architecture	Material	Cool-Down [c]	Applicability [d]	Adjustability [e]	Publication	Status [f]
[40, 41]	SSRF	Magnet	NbTi wire	160	0.8	0.8 *	8 bands	CFRP	E-SC	possible	SVI-P-R	2014, 2021	op.
[42, 43, 84, 85]	ESS	Cavity	Nb sheets	210	1.5 ca.	0.45 *	8 rods + 1 post ***	Ti-6Al-4V (rod) + power-coupler	E-SC	possible	SVI-P-R	2013, 2014 2017 2023	const.
[47, 48, 86]	HL-LHC	Cavity	Nb bulk	250	0.7 *	1 *	2 blades + 1 post	SS 316L + power-coupler	N-AC	possible	VGI-P-NR *	2014, 2017 2018	dev.
[49, 50, 87]	SPL	Cavity	Nb bulk		1.5 *	0.45 *	2 ICS + 1 post		N-AC	possible	VGI-P-NR *	2011, 2012 2014	ND
[44–46, 84]	ESS (spoke)	Cavity	Nb sheets		1.92	0.6 *	22 rods + 2 posts	Ti-6Al-4V (rod) + power-coupler	ND	possible	SVI-P-R	2013, 2014, 2016, 2017	const.
[67]	VECC	Magnet	Bi-2223 wire		0.4	0.4 *	4 bands	G10	N-AC	discouraged	VGI-P-NR	2023	op.
[68]	CAS	Magnet	YBCO tape		0.4 *	0.3 *	8 pillars	G10	E-SC	possible	SVI-P-R	2019	dev.
[52]	MDS (UT)	Magnet	NbTi wire	520	1.54	1 *	4 posts + 4 rods	G11	E-AC *	possible	Not relevant	2021	dev.
[56, 63]	HIE-ISOLDE	Frame	Cu sheets Nb coating	850	2	1 *	2 rods + 2 plates		N-AC	discouraged	SVI-P-NR	2014, 2018	op.
[38]	IHEP	Magnet		1400	1.4 ca.	0.2 *	8 bands	T300 (CFRP)	E-SC	possible	SVI-P-R	2020	op.
[37, 88]	TLS	Magnet	NbTi wire		1.4	0.2 *	8 bands	UFGE	E-SC	possible	SVI-P-R	2006, 2007	op.
[39]	MICE	Magnet	NbTi wire	1600	0.3	1.7	8 bands	UFGE	E-SC	possible	SVI-P-R	2011	op.
[32, 33]	FAIR	Frame	NbTi wire		5.56	0.7 *	8 rods	Ti-6Al-4V + AISI 304	N-SC	possible	VGI-P-NR *	2012, 2014	const.
[51, 57]	Mu2e	Magnet	NbTi wire		6.7	0.8 *	3 springs + 14 rods	Inconel® 718	ND	possible	SVI-P-R*	2013, 2017	const.

Table 2.4: Continuation.

Ref	Project	Element	SC material	Mass kg	L1 [a] m	L2 [b] m	Architecture	Material	Cool-down [c]	Applicability [d]	Adjustability [e]	Publication	Status [f]
[29, 89]	RHIC	Magnet	NbTi wire	3605	9.4	0.3 *	3 posts	Ultem® 2100 or SEl-GFN3 Noryl®	N-AC	possible	VGI-P-NR *	1991, 1995	op.
[36]	CAS	Magnet		4000	1.4	2.2	8 bands		E-SC	possible		2011	res.
[54]	ATLAS CS	Magnet	NbTi wire	4700	5.3	2.6	24 struts	GFRE	N-AC	possible	SVI-P-R	2007	op.
[30, 90]	SSC	Magnet	NbTi wire	7700	17	0.3 *	5 posts	G11CR	N-AC	possible	VGI-P-NR *	1988, 1990	cancelled
[31, 91]	LCLS-II	HE pipe	Nb sheets	8600	12	0.6 *	3 posts (hung)	G10	N-AC *	discouraged	SVI-P-NR + VGI-P-NR	2015, 2018	op.
[25, 26]	ITER	Feeder		10,000 ca.	10 ca.	0.5 *	2 posts	SS 316LN	N-AC *	possible	Not relevant	2013	const.
[27, 28, 83, 92]	LHC	Magnet	NbTi wire	25,000 **	16 **	0.6	3 posts **	GFRE	N-AC	possible	VGI-P-NR	1998, 1999 2004, 2005	op.
[55, 60, 61]	ATLAS BT	Magnet	NbTi wire	45,000	25	5	8 rods + 32 stops	Ti 5Al 2.5 Sn ELI GFRE	D-SC *	possible	VGI-P-R	1997, 2005 2006	op.
[34, 35, 93]	NeuroSpin	Magnet	NbTi wire	132,000	5	4	8 rods	Ti-6Al-4V	E-SC	possible	SVI-P-R *	2010, 2011 2023	comm.
[53, 58, 59]	ATLAS ECT	Magnet	NbTi wire	160,000	5	10.7	20 rods	stainless steel	ND	possible	SVI-P-R	1999, 2008	op.
[62]	CMS CS	Magnet	NbTi wire	225,000	12.5	6 ca.	30 rods	Ti 5Al 2.5Sn ELI	E-SC	possible	SVI-P-R *	2002	op.
[65, 66]	ITER	Magnet	Nb3Sn and NbTi	23×10^6	24	30	18 multi-blades	stainless steel	E-AC	possible	VGI-P-NR *	2011, 2013	const.
[64]	DEMO	Magnet	Nb3Sn, NbTi and RE-123		36 ca.	45 ca.	16 multi-blades	stainless steel	E-AC	possible	VGI-P-NR *	2022	dev.

a: Axial length of the supported body, (curvilinear for Mu2e project). b: Second major length of the supported body. c: Cool-down effect classification: Extra stress can arise as a consequence of cool-down (E). No extra stress (N). De-stress (D). Symmetric Contraction, the pose (position and rotation) of the cold mass does not change (SC). Asymmetric Contraction, the pose changes (AC). Not easily Deducible (ND). d: Applicability to a rotating machine. e: Adjustability classification: The pose of the cold mass is adjusted acting at the Suspension system to Vacuum vessel Interface (SVI). Vacuum vessel to Ground Interface (VGI). The alignment is Passive (P) if not actuated or Active (A). The adjustable system is applicable to rotating bodies (R) or not applicable (NR) mainly due to unilateral fixtures. f: Status at the beginning of 2023. In development (dev.), in construction (const.), in commissioning (comm.), operational (op.), and for research only (res.). * Not reported even implicitly. Deducted by this author. ** Data of cryodipoles, not of SSS. *** The post is represented by the power coupler, able to slide vertically but fixed radially in this case.

The materials for the supporting systems most commonly found in this literature analysis belong to either metallic or composite classes. The choice is guided by the compliance to requirements of mechanical resistance and minimization of heat loads to the cold mass The most common metallic materials used include titanium alloys, stainless steel alloys and nickel-chromium alloys. Composites such as glass fiber-reinforced epoxy or carbon fiber-reinforced polymers have also been utilized. Although not explicitly mentioned in the articles subject to this review, an analysis of Table 2.4 highlights a possible correlation between the shape of the support and its material. Indeed, almost all rods have been build from metallic materials while all double-bands architectures exploits composites. An exception is represented by the G11 rods of the magnetic density separator studied at UT.

Two recurrent solutions for adjustability have been identified based on the position of a tuning link in the chain of errors. This link can be found placed between the cold mass supports and the vacuum vessel (SVI) and/or between the vacuum vessel and the rigid ground (VGI).

All proposed solutions found in literature have been designed to function nominally, reacting mostly dead weight or electromagnetic forces in a static environment (i.e., no relative rotation with respect to the gravity vector). Generally, transportation loads, seismic loads, and catastrophic failures such as destructive quenching have been considered in the design process. Therefore, most of the solutions have been just verified for mechanical resistance in directions different from those on which the nominal load is acting. The misalignment of the cold mass due to the dead weight is constant and can be compensated once for all during assembly, leaving no design constrain on the stiffness of the system. Therefore, even though the position of the cold mass is a requirement of the supporting system, its design follows just a trade-off between heat loads and mechanical resistance.

In contrast, in presence of variable loads like in the case of the rotating gantry the complete passive compensation of the misalignment cannot be achieved for all loading conditions. For example, a compensation for the cryogenic device position done at a certain angular position of the gantry is detrimental to the positioning of the cryogenic

device when the gantry moves to another position. Therefore, in case of variable loads a change of paradigm is necessary: the design trade-off should be between heat loads and the overall stiffness of the supporting system, which is usually more restrictive than mechanical resistance alone. Hence, there is a space for research in architectures tailored to work on rotating machines. Most supporting systems presented in this literature analysis are deemed conceptually applicable in case of variable loads. However, deeper analysis and tailored designs are needed to adapt the same conceptual approaches to the case study presented in this thesis.

The supporting systems classified as SVI appears to be often designed with bilateral fixtures such as rod ends and spherical bearings, therefore, it would be be directly applicable to a rotating machine. In contrast, VGI supporting systems simplified designs usually exploits unilateral fixtures such as spherical washers. Hence, these are not directly applicable to rotating machines without additional R&D. A regulation system at the SVI for the pose of a body supported by posts is expected to raise the level of complexity of the cryostat assembly and decrease performances (stiffness) of the tuning system itself because of the serial combination of linear guides and pivots.

As mentioned, structures can be statically determinate or indeterminate based on the number and type of joints used and the number of bodies in the system. Generally, a statically determinate solution is easily automated, because the movement in the joints does not generate extra stress in the system. In contrast a statically indeterminate supporting system is difficult to automate. Except for the supporting system of ISOLDE, all other architectures found are statically indeterminate, they are indeed over-constrained. However, the motorized struts of ISOLDE allows an adjustment of only four degrees of freedom of the cold mass. Hence, the supporting system has not been fully automated. Therefore, a detailed solution for the support and complete alignment system of a body with an exact number of constrains has not been found in this literature analysis and is highlighted as an open knowledge gap that this thesis will consider.

2.4 Chapter conclusions

The literature analysis has highlighted the lack of documented solutions for the supporting system of cryogenic devices subject to highly variable loads in general and specifically for medical applications such as the gantry. The review has identified recurring design patterns for the supporting systems of cryogenic devices such as superconducting magnets and radio frequency cavities but only subject to static loads. Furthermore, all studies reviewed mention only FEAs as method of studying the system, highlighting the possible lack of mathematical modeling formalization in this field. A classification based on the system's geometrical architecture, cool-down behavior, and adjustability has been presented. Common design characteristics, such as the dimensions and weight of the suspended body, materials used for the supports, and current status, have been summarized in a table. A conceptual analysis of the feasibility of transferring these supporting systems to applications with highly variable loads (for example rotating medical machines) has been provided. This highlighted that none of the designs found have been specifically designed for applications with highly variable loads, indicating possible directions of

study for this thesis. Additionally, the literature analysis suggests that the eight-supports architecture is a viable statically indeterminate candidate to be re-designed in compliance with the requirements of the gantry application, or in general an application where load are highly variable. Furthermore, a statically determinate solution for the supporting system and 6DOFs alignment system has been highlighted as a subject where knowledge is completely missing. The evolution of this thesis, exploring the gaps highlighted can be valuable, especially in the case of medical superconducting machines for hadron therapy or other possible applications such as superconducting generators for wind turbines, superconducting radio frequency cavities, optical alignment systems for cryogenic devices such as high-energy physics experimental apparatus, and satellites.

3 RESEARCH FRAMEWORK FOR THE DEVELOPMENT OF SUPPORTING SYSTEMS OF CRYOGENIC DEVICES

As highlighted by the literature analysis in the previous chapter the supporting system of cryogenic devices subject to highly variable loads lack of a specific solution. Furthermore, the research field lacks in completeness because no statically determinate solution has been found in the literature analysis. Additionally, the research field seem to lack of general mathematical formalism to study the problem, with all studies found relying on FEAs. This chapter proposes a more structured approach to study the supporting system of cryogenic devices subject to highly variable loads and in the specific the study case of superconducting magnets on the rotating gantry.

First, this thesis aims at filling the lack of completeness by studying both statically determinate and indeterminate supporting systems as mentioned in the design objectives. Next, the optimization approach is discussed, this is crucial because of the possible human bias of deciding which of the two solutions is better. Then, the possible design requirements and load cases are listed taking as a study case the rotating gantry. Next, the methodology for the formulation of mathematical models is presented in order to fill the lack of mathematical formalism. Relevant comparison metrics are listed, in order to decide which of the two solutions is better. Finally, a list of tools used in the study is given.

3.1 Design objectives of the thesis

In structural mechanics, structures are classified as *statically determinate* or *statically indeterminate*. Statically determinate structures are defined as systems for which the number of equations match the number of unknowns, or physically, all the degrees of freedom of the system are exactly constrained. Generally, statically indeterminate structures are stiffer and stronger as well as intrinsically redundant. Thus, the failure is generally not catastrophic since alternative load paths are available. However, changes, such as displacements generated by thermal contraction typically generate additional stresses in the structure. Furthermore, the analysis of these systems requires additional information and numerical methods already at the calculation stage of reaction forces [94].

The literature analysis conducted [95] and reported in Chapter 2 highlighted the lack of completeness in designing the suspension system for a cryogenic device subject to a static load. The cases studied in the literature analysis show a tendency to use statically indeterminate (or over-constrained) suspension architectures instead of statically determinate (or exactly constrained). Some simple statically determinate cases found in literature have been judged non transferable to an application where loads are highly variable. With the aim of studying in a comprehensive way the suspension system of a cryogenic device subject to variable loads, this work will consider both statically determinate and indeterminate solutions discussing the possible architectures in Chapter 4.

3.2 Optimization approach of supporting systems

A crucial point in choosing the optimization approach is related to the structural nature and desirable characteristics of the architecture used: statically indeterminate architectures usually exploit a symmetric arrangement of the supports in order to maintain the cryogenic device in the same position through the cool-down phase. This design constraint is applied to the over-constrained architecture proposed in this work. However, the addition of symmetries reduces the number of free parameters that define the arrangement of supports up to the point that the optimization becomes easier even if manually-driven (sensitivity analysis), allowing the designer to have a greater understanding of the effect of each parameter. On the contrary, the arrangement for an exactly constrained architecture is defined by an higher number of parameters since there are less imposed symmetries. This makes difficult for a designer to have a clear understanding of the effect of each parameter. To conclude, the mentioned design choices for the architectures introduce a bias for the efficacy of the optimization process and then a bias in the comparison if the optimization is manually-driven. Given the substantial differences in the proposed architectures, this work will exploit a machine-driven optimization approach to ensure an unbiased comparison of the solutions.

In mechanics, the optimization approach can be based usually on two main methods:

- Finite Element Analysis (FEA): the standard tool to solve structures of non basic shapes with multi-bodies interactions,
- analytic models: commonly used applied to simple geometries and load cases.

The underlying idea behind FEAs is to subdivide the complex geometries into much smaller general shaped elements (meshing) and solve equilibrium equations inverting combined stiffness matrices of all elements. The computational cost as well as the accuracy of the solution highly depends on the number of elements of the mesh. An analytical model has the advantage to be much faster than a FEA since it also requires to solve equilibrium equations or matrix inversions but on a much smaller number of bodies: tens against tens of thousands or even hundreds of thousands. The optimization process, supposing to use the same computational resources, highly benefits from the use of an analytical models. Therefore, this thesis will explore the use of a machine-driven optimization based on analytical models.

3.3 Design requirements for supporting systems

Having chosen a machine-driven optimization base on analytical models it is important to analyze the minimum parameters to introduce in such models. Hence, the main requirements for the design are listed and described in Table 3.1 taking the study case of the gantry as example.

Table 3.1: *The basic requirements for the design of the suspension system of the superconducting elements on a gantry.*

Category	Requirement	Description	Priority
Functionality	Accuracy	The pose (position and rotation) of the cold mass, measured at its geometrical center must be within $\pm 0.6\,\text{mm}\,(3\sigma)$ or $\pm\,0.6\,\text{mrad}\,(3\sigma)$ for all the six Degrees of Freedom (DOF) at each gantry angular position	higher
	Alignment	The suspension system must be able to correct positioning errors of the geometrical center of the cold mass up to $\pm 20\,\text{mm}$ and $\pm 20\,\text{mrad}$ along any direction	high
	Thermal insulation	The suspension elements must insulate the cold mass from external environment conductive heat loads, minimizing these	high
Structural integrity	Mechanical resistance	The system must be able to withstand loads encountered during the life-cycle of the product	high
	Vibration	Natural vibrations frequencies of the suspension architecture must not be excited by expected external excitation	normal
	Environment compatibility	The system components must be able to operate at cryogenic temperatures (4.5 K) and in a radiation environment	high
Geometry	Compactness	The suspension system must not exceed 1.8 m in width	nice to have
	Lightness	The cryostat must be under 1.5 t	nice to have
Production	Feasibility	Standard manufacturing technologies should be applied and commercial parts used as much as possible	nice to have

The design requirements have been assigned a priority level for the satisfaction of requirements. The priority levels associated with each requirement has been listed in Table 3.1. For instance, the accuracy necessary to guarantee functionality for the treatment has the highest priority, followed by the requirements on mechanical resistance, environment compatibility, alignment, and thermal insulation.

3.4 Load cases

Functionality and structural integrity must be ensured for the following types of loads: nominal loads during the operation of the gantry, transportation or handling loads during the manufacturing and assembly phase, seismic loads and accidental loads. A description

of the loads is given in Table 3.2.

Table 3.2: *The expected load scenarios for the suspension system of the cold mass in a superconducting gantry*

Scenario	Description
Nominal	The suspension system is mainly subject to the weight of the suspended body. In the local reference frame of the suspension system, the weight is a force applied to the center of gravity of the supported body and its direction depends on the position of the gantry. Therefore, the suspension system is subject to cyclic loads during nominal operations. Electromagnetic interactions with adjacent magnets have been assumed negligible due to the drop in magnetic field strength already in the proximity of the magnet which should not influence the adjacent supported cold masses. The suspension elements may be subject to extra loads during cool-down if the architecture is statically indeterminate
Transportation and handling	The suspension system is subject to extra accelerations every time the cryostat is transported trough sites or moved by lifting devices.
Seismic	The suspension system is subject to extra accelerations in the eventuality of earthquakes.
Accidental	The suspension system is subject to accidental loads due to quench.

In this thesis, nominal loads are used to size the system against fatigue. For instance, similar applications registered in a period of 10 years a number of rotations of the gantry - fatigue cycles equal to 300000. Given an estimated life for the system of 30 years the number of cycles to be expected for the components of the supporting system is about one million. Other loads are used to verify the sizing of the system.

3.5 Formulation of analytical models

As mentioned in the section regarding optimization approach, the use of a FEAs is less favorable increasing the computational cost of the analysis. The development of analytical solutions is therefore preferred. Additionally, mathematical models developed in this thesis can help in filling the lack of mathematical formalism in the field. Analytical models formulated in this work must include all necessary boundary conditions and loads to accurately represent real-world conditions and allow the optimization of the suspension architecture. In particular models must include as input parameters:

- the spatial disposition of all supports,
- the geometry of the single support element,
- the material of the supports,
- the operating temperature.

The minimum output quantities of the model are the stress state of the supports to ensure mechanical resistance and the position (e_x, e_y, e_z) and orientation $(\theta_x, \theta_y, \theta_z)$ of the

cryogenic device in order to ensure to meet accuracy requirements. In order to study the different loading conditions the models must include:

- the effect of a generic load composed of forces and moments $\mathbf{F_s} = (F_x, F_y, F_z, M_x, M_y, M_z)$ acting on the cryogenic device,
- the effect of the cool-down or warm-up phases for the cryogenic device,
- the effect of pre-load,
- the effect of the insulation vacuum.

To compare the two architecture types both the influence of the vacuum vessel stiffness and the stiffness of supports must be included. For the optimization phase alone, the formulation of the models is restricted to the overall geometry of the support architecture without considering the vacuum vessel influence.

3.6 Comparison analysis metrics

The design methodology chosen foresees that the design candidates are compared against each other through a series of criteria based on the main highlighted requirements. The compliance to the structural integrity requirement is guaranteed by sizing the supports with the same safety factor on nominal loads. The quantitative comparison parameters are related to:

- the compliance to the functionality requirement judged on the basis of the maximum deviation from the nominal position of the cryogenic device. The deviation is compared for each of the six DOFs;
- the compliance to the functionality requirement judged on the basis of the heat-flux deposited on from the thermal shield to the cold mass (at 4.7 K) through the supports;
- the compliance to the structural integrity judged on the basis of the safety factor over transportation and handling loads;
- the sensitivity of the system to variations in manufacturing tolerances and pre-load;
- the natural frequencies of the system;

other qualitative factors are related to the ease of manufacturing, alignment and possible automation of the system.

3.7 IT tools used in the research

The following tools have been used:

- Google scholar for literature analysis,
- Wolfram Mathematica, for solving analytical models, computing, optimizations, sensitivity analysis and 3D figures and plotting;
- Solidworks for 3D modelling,
- *Ansys® Workbench, 2022 R2* for FEAs for validation and vibration analysis,
- Microsoft Excel for comparison tables.

4 SUPPORTING SYSTEM ARCHITECTURES AND POSSIBLE MATERIALS

As mentioned in the design objectives, this work aims generally at studying in a comprehensive way the supporting system for a cryogenic device subject to variable loads, and in particular the superconducting magnets on a rotating gantry for medical applications. This chapter gives context about the elements of the gantry beam line subject of this study (see Figure 4.1) and highlights the possible general characteristics of the two supporting systems that will be compared in this thesis. The two architectures proposed cover both the statically determinate (or exactly constrained) and the statically indeterminate (or over-constrained) options. Statically determinate and indeterminate proposed architectures are named respectively “6S” and “8S”.

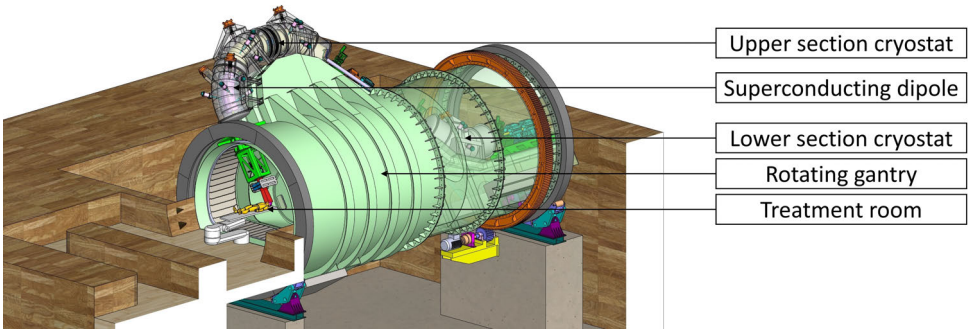

Figure 4.1: *View of the gantry hall and treatment room, the gantry main structure rotates around the patient carrying the gantry beam line. upper and lower section cryostats are some of the components of the beam line. Inside cryostats the superconducting dipoles are supported by their supporting system.*

4.1 Data and machine layout

The gantry beam line subject to this study [96] is represented in Figure 4.2, it consists of four superconducting dipoles (magenta) and five superconducting quadrupoles (blue) fixed rigidly to the dipoles ends. Bent superconducting dipoles have a curvature radius of 1.65 m and an estimated mass of 1.5 t, the cold-mass varies in weight from 1.5 t to 1.75 t depending on the number of quadrupoles fixed to the dipole. The gantry beam line with all the infrastructure needed for its operation is mounted on the gantry main structure (Figure 4.1), responsible of sustaining the beam line and rotating it 360° around the patient.

The gantry beam line consists of normal conducting elements and superconducting elements, the latter are hosted in two separates cryostats (lower and upper section cryostats in Figure 4.1). In order to minimize the heat-load to the cold-mass, the number of cold-warm transition has been minimized. Hence, the reason of having two separate cryostats

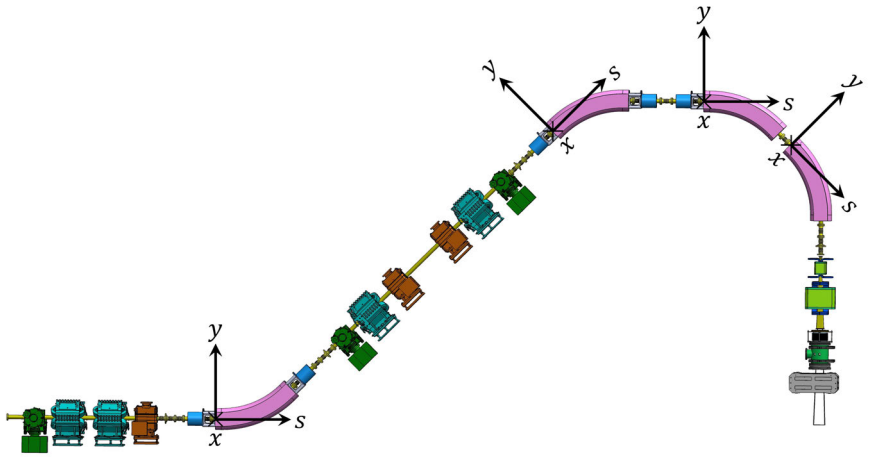

Figure 4.2: *Scheme of the gantry beam line for the gantry. Superconducting dipoles in magenta. Reference systems according to the MADx convention.*

instead of four. The upper section cryostat is composed of three modules to allow the maintenance of each separately and reduce possible machine downtime. Each cold-mass in each module is supported independently by its own supporting system.

4.2 Challenges for the supporting system and alignment system

Usually the design of the supporting system and alignment system are decoupled, and are heavily dependent on the loads for a specific application. Most of the applications found in the literature analysis are subject mainly to the load given by the own weight of the cryogenic device in nominal conditions. Hence the supporting and alignment systems are placed in a vertical arrangement. As mentioned, one of the challenges of a supporting system is to minimize heat-flux which require small cross-sections of the supports. The design paradigm for such systems aims at reaching first the mechanical resistance required (usually defined by a minimum safety factor). Then, the use of thermally insulating materials (like GFRE) enables to contain heat-loads as much as possible. This results usually in a support which is not very stiff, either because the material chosen has not an high elastic modulus (like GFRE), or because the cross-section chosen for the supports is the minimum required to satisfy mechanical resistance. The loads applied to such supports produce non negligible deformations if compared to the accuracy required to these applications. The alignment system can be used to correct this deformation as illustrated in Figure 4.3. However, in applications with highly variable loads, such as the gantry, compensation performed at one position (or at a given time if the load oscillates over time) is not only ineffective at other positions but is even detrimental. This can be seen looking at the last three images illustrated in Figure 4.3, where an initial compensation done for an error of $\delta = mg/k$ (mass m, gravity g, support axial stiffness k) when the load changes direction becomes an error of 2δ over the nominal position of the

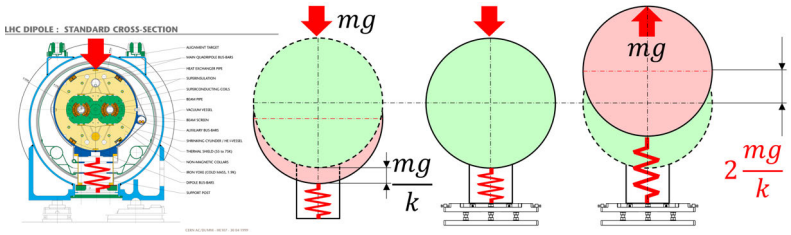

Figure 4.3: *Visual explanation of the role of stiffness in an application subject to variable loads. From left to right: image of a real application (LHC) courtesy of CERN, schematic of the compression on the supports for a real application, compensation of the deformation by mean of the alignment system, effect of a load swithing sign.*

cryogenic device. Therefore, the compensation system should not be used to compensate for elastic deformations in case of variable loads, but more importantly the stiffness of the supporting system is no longer negligible as the accuracy during operation δ depends solely on the stiffness k. In conclusion a change of paradigm is necessary and stiffness must be taken into account more during the sizing of the supports. This has an impact on the trade off with heat-loads and may require different considerations on material choices than those done in common applications subject to static loads only.

4.3 Statically determinate architecture "6S"

The "6S" architecture is inspired by a widely used kinematic design in robotics, commonly referred to as a hexapod. (Figure 4.4). As mentioned in the literature analysis reported in previous chapters, applications of this architecture to cryogenic devices have not been found. In this architecture the cold-mass is supported by six supports with a kinematic classified as a 6-PSU or 6-PSS fully parallel mechanism [97] (see Figure 4.4 for intuitive understanding of the differences). A 1D actuation of the prismatic (P) joints (warm joint in Figure 4.5) allows for the control of all 6 Degrees of Freedom (DOF). The spherical (S) warm joints connect the supports to the prismatic joints to the vacuum vessel interface while spherical or universal (S or U) joints connect the rods to the cold-mass. Spherical and universal joints are chosen so that the supports are loaded only axially. The exclusion of other internal actions allows the designer to reduce the size of the supports limiting the heat flux passing through them. Additional internal actions would increase the stress in the supports requiring to size larger cross-sections and as consequence accepting larger heat-loads. The baseline for the adjustment system foresees a single alignment at warm without vacuum performed by operators manually. The same architecture does not exclude the possibility to implement an automated system for an active alignment at cold in the future.

4.4 Statically indeterminate architecture "8S"

Architecture "8S" is inspired to the 8-support configurations found in literature as supports of superconducting elements [32, 34, 36–40]. All results found in literature are related to superconducting elements that are mounted on the ground and are not

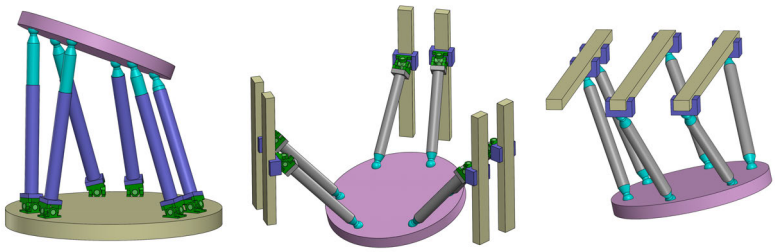

Figure 4.4: *Examples of a common hexapod architectures in robotics. From left to right: 6-UPS, 6-PUS, 6-PSS parallel mechanisms.*

subject to variable loads, thus even if inspired to this architecture, the design developed in this work is specifically designed to withstand the variable loads. Eight supports with spherical or universal joints at each end connect the cryogenic device with the vacuum vessel (Figure 4.5).

The 8S architecture is usually chosen for its "self-aligning" behavior, this is because the 8 supports are put in a symmetric configuration with respect to Cartesian planes that contain the reference point - a point arbitrarily chosen to measure the misalignments of the cold mass. Due to the theoretical symmetric configuration, assuming the same thermal gradients, same properties of the materials, and same geometrical dimensions, each supporting element should contract of the same amount without changing the alignment of the body between the room temperature state and the operational state (at 4.7 K). A 3D passive alignment of each warm joint is necessary to put the cold mass in its position at warm with the help of a temporary holding system.

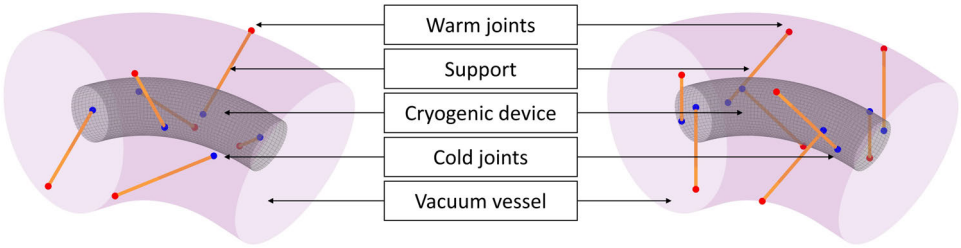

Figure 4.5: *Basic schematic of the 6S (left) and 8S (right) architecture with the cryogenic device (grey), its supports (orange), cold and warm joints (blue and red), and the vacuum vessel (pink).*

4.5 Other possible supporting systems

Single post solutions have been excluded because of the complexity associated with the variability of the loading direction. Additionally, a single supports requires a serial adjustment system to regulate the position of the cryogenic device, this coupled with the variable nature of the load adds complexity to the design of a backlash free and stiff alignment system.

Solutions with 7 supports have not been considered, on one hand because they cannot be symmetric like solution 8S and thus possibly negate the self-alignment behavior. On the other hand a 7-support architecture is not exactly constrained, negating the possible benefits related to a solution like the proposed 6S. As it will be demonstrated in Section 6.4, the models developed in this work can be applied for the study of the 7-support architecture or any other number of supports ($\geq$6) if future research explores that.

Solutions with more than eight supports have not been considered because of the increase of penetrations of the vacuum vessel and thermal shield that add complications to the assembly phase and heatloads on the shield/cold mass.

4.6 Proposed support geometries and materials

The geometry mostly used for the supporting elements can be either a cylindrical rod "R" or a double-band support "DB". With reference to the literature analysis conducted [95], three materials are the mostly used: Glass Fibre Reinforced Epoxy (GFRE), austenitic stainless steel SS304L and titanium alloy Ti-6Al-4V. Carbon Fibre Reinforced Polymer (CFRP) and Glass Fibre Reinforced Epoxy (GFRE) have been used more rarely. INVAR has been included in this analysis for completeness having a very low thermal contraction (desirable to maintain positioning during cool-down).

Table 4.1: *Possible combinations of support element geometry and material for each architecture.*

	GFRE	**CFRP**	**SS304L**	**Ti6Al4V**	**INVAR**
6S-R	-	-	YES	YES	YES
8S-R	-	-	YES	YES	YES
8S-DB	YES	YES	-	-	-

The possible combinations of geometry of the supporting elements and the material are reported in Table 4.1. As can be seen, not all combinations are deemed worth exploring: both 6S and 8S solutions with rod shaped supports built in CFRP or GFRE require complex interfaces with the end joints and the thermalization. This interfaces are critical regions when subject to multiple thermal and mechanical load cycles. Additionally, traditional ways of machining related to metals must be substituted with less standard manufacturing processes in order to not compromise the structural integrity of the support. R-CFRP variants have been abandoned due to the behavior of carbon fiber composite materials during thermal cycles between room temperature and 4.7 K. Over the machine's 30-year lifespan, 60 to 100 such cycles are anticipated and the choice of CFRP can be critical. During thermal cycles micro cracks develop in the resin matrix, even in regions far from the joint interfaces, reducing the mechanical properties of the material. Additionally, cross-ply differential thermal contraction may lead to shear stresses at the interfaces and consequent delamination. 6S-DB solutions have not been studied because the use of DB negates the possibility of having a support that works in compression which is a desirable characteristic during the alignment phase. CFRP or GFRE composites are good candidates for the "8S-DB" configuration because the band geometry allows to wrap

fibers around the interfaces in an unidirectional pattern. Hence the fibers would be loaded only axially, and always in tension during the rotation of the machine, due to pre-load and differential thermal contraction of supports and cold-mass. Micro-cracks in the matrix do not influence mechanical resistance properties of the composite in this case because the fibers are in the direction of the load, considering that generally the resistance of the composite is primarily given by the fibers. Cross-ply differential thermal contraction is absent because there is no need to have plies in directions that are different from the direction of the load. No advantage would be gained by having a 8S-DB in a metallic material rather than a 8S-R configuration since the stiffness, mechanical resistance and heat loads depend only on the cross section surface of the support and not its geometry.

The choice of the arrangement of each of the supports and of the geometry (rod or double band) and material of supports for both architectures requires to find an answer to the following questions:

- which is the support arrangement that maximizes the rigidity of the system, not only at one working position of the machine but overall during the complete rotation;
- which support arrangement distributes the loads most evenly across the supports, allowing for a smaller cross-section to meet mechanical resistance requirements and thereby minimizing heat loads;
- which is the support arrangement that enables a full recovery of backlash with the minimum amount of pre-load so that the loads on supports are minimized, minimizing again the heat-loads;
- which is the support arrangement that minimizes the extra-loads during cool-down for the over-constrained solution.

The solution space for possible support arrangements is extensive, with the general 6S and 8S configurations having 30 and 40 free parameters, respectively, that determine the support placement. No known examples of the 6S architecture have been identified, making it more challenging to define boundaries for the support arrangement and increasing the risk of overlooking viable solutions. In contrast, the 8S configuration has been intentionally designed with greater symmetry, to eliminate misalignments during cool-down, which restricts the solution space and simplifies the designer's ability to interpret the influence of each free parameter. In this thesis after having applied symmetries, solution 6S has 16 free parameters while solution 8S has 6. This introduces a human bias, as mentioned before, in the optimization and further comparison of the two architectures.

4.7 Chapter conclusions

In conclusion, two possible supporting architectures have been proposed, covering both statically determinate and indeterminate cases. Different geometries and materials for the supporting elements have been analyzed, with certain combinations excluded due to potential issues. Next, the need to thoroughly study the arrangement of supports has been highlighted, along with the potential limitations arising from human bias in comparing the two solutions. The use of a machine-driven optimization has been proposed to solve this issue and will be discussed in Chapter 7. This approach would be highly limited

by computational resources and/or solution time if Finite Element Analysis (FEA) are used to evaluate the rigidity of the system at a satisfactory number of machine positions, for a large number of support arrangements. Therefore, less computationally expensive semi-analytical models will be developed in Chapter 5 for both the statically determinate and indeterminate cases.

5 LUMPED PARAMETER MODELS

As mentioned in the previous chapter the development of analytical solutions is preferred to FEAs to reduce the computational costs of optimization, comparisons and other analysis. These models must include all necessary boundary conditions and loads to accurately represent real-world conditions and at the same time must be composed of a minimal number of parameters to be understandable. For these reasons such models will be referred to as Lumped Parameter Models (LPMs) hereafter.

The LPMs are developed to estimate the pose of the cryogenic device (e_x, e_y, e_z, $\theta_x, \theta_y, \theta_z$), union of position ($e_x, e_y, e_z$) and orientation ($\theta_x, \theta_y, \theta_z$), as well to estimate the axial internal actions on the supports. This chapter develops the LPMs both for an exactly constrained supporting system using six linking bars (a bar or linking element jointed only by spherical or universal joints) and for a generic over-constrained architecture of any number of linking bars.

In order to accurately represent the real-world behavior of the supporting system, the most relevant mechanical error sources contributing to the misalignment of the cryogenic are listed and classified hereafter. Mechanical errors that influence the pose of the cold-mass have been classified in systematic and random in Table 5.1. Systematic errors can be further classified as symmetric and non-symmetric. The frames of reference for these errors are those rotating with the gantry, the master frame $\{g\}$ and local frames $\{0\}$ for each cold mass in Figure 5.1. All frames are defined with respect to the master frame in the room $\{r\}$ (Figure 5.1).

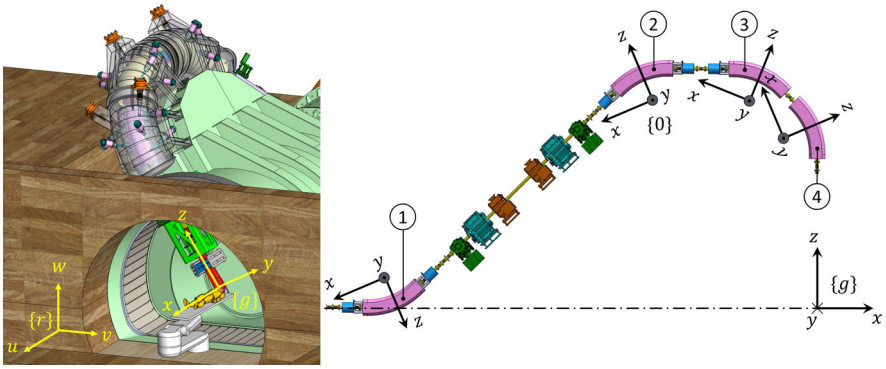

Figure 5.1: *Illustration of the frame of reference used. $\{r\}$ the master frame in the assembly room, $\{g\}$ the master frame rotating with the gantry, $\{0\}$ the local frame for each cold mass (right image). Numbering convention used for the cold masses.*

The non-symmetric errors can be thought as errors that during a 360° rotation of the machine have a non null mean. An intuitive example of non symmetric errors is represented by displacement of the cold mass during cool-down, this is assumed to be always reproducible and with a mean value for each DOF which is independent from the gantry position. Furthermore, the cool-down effect is only a constant non-symmetric

contribution to the overall error, the deformation of the vacuum vessel due to differential pressure is also a constant non-symmetric contribution. All other non-symmetric errors can be decomposed as a mean value and a symmetric error. The overall mean value can be measured and corrected during the alignment phase. The sum of all symmetric components of the various errors must satisfy requirements to ensure the stability of the pose of the cold-mass during operation.

Table 5.1: *List and classification of mechanical error sources that contributes to an error in the pose of the cold-mass during operation.*

Nature	Characteristics	Description
Systematic	Symmetric	Deformation of the support elements
		Deformation of the main structure
		Backlash
	Non-Symmetric	Deformation of the vacuum vessel due to cold-mass weight
		Deformation of the vacuum vessel due to own distributed weight
		Deformation of the vacuum vessel due to differential pressure
		Displacements due to the cool-down process

Random errors, related to uncertainties of thermal properties, the manufacturing tolerances, the uncertainty due to the accuracy of the alignment system and measuring system are treated in the sensitivity analysis in Section 9.1. In conclusion what must be compared to the error budget is the superposition of effects of all systematic symmetric errors (also the symmetric part of non symmetric errors). To this systematic components, the random errors resulting from the sensitivity analysis on the LPM must be added.

The main contributions and how they have been implemented in the LPMs are reported in the following sections. The deformation of the main structure does depend on the choice of the supporting system, it has been reported in Table 5.1 for sake of completeness but it is not considered in the formulation of LPMs. Effects contributions are reported hereafter consistently with the order in which should be implemented instead than following Table 5.1.

5.1 6S Lumped Parameter Model

The mathematical formalism of the LPM is based on modifications to Inverse Position Kinematics (IPK) and Direct Position Kinematics (DPK) - two mathematical tools that comes from robotics, in particular parallel mechanisms [97]. This section discusses the newly introduced modifications specifically made on the IPK and DPK of the so called Hexaglide [98] to be able to study all effects that were not present in the original model.

5.1.1 Deformation of the support elements

The resultant forces on the cold-mass can be written as:

$$\mathbf{F}_s = \mathbf{J}^T \mathbf{F}_q \tag{5.1}$$

where $\mathbf{J}$ is the geometrical Jacobian matrix and $\mathbf{F}_q$ is the vector of forces on actuated joints (Figure 5.2). In case of the parallel mechanism proposed the geometrical jacobian can be expressed by:

$$\mathbf{J} = \begin{bmatrix} w_{1x} & w_{1y} & w_{1z} & u_{1x} & u_{1y} & u_{1z} \\ \vdots & \vdots & \vdots & \vdots & \vdots & \vdots \\ w_{ix} & w_{iy} & w_{iz} & u_{ix} & u_{iy} & u_{iz} \\ \vdots & \vdots & \vdots & \vdots & \vdots & \vdots \\ w_{6x} & w_{6y} & w_{6z} & u_{6x} & u_{6y} & u_{6z} \end{bmatrix} \quad \text{with}$$

$$\mathbf{w}_i = \frac{{}^0\mathbf{M}_i - {}^0\mathbf{H}_i}{\|{}^0\mathbf{M}_i - {}^0\mathbf{H}_i\|} \quad \text{and} \quad \mathbf{u}_i = \mathbf{p}_i \times \mathbf{w}_i \tag{5.2}$$

with reference to Figure 5.2, $\mathbf{w}_i$ is the direction along the longitudinal axis of the i-th support while $\mathbf{p_i}$ is the position of an arbitrary point on the axis of the support and can be conveniently taken as $\mathbf{p}_i = \mathbf{r}_i$.

The force acting on the cryogenic device $\mathbf{F}_s$ contains the external forces and moments acting on the cold-mass:

$$\mathbf{F}_s = (m\mathbf{g}\,, \mathbf{r}_{COG} \times m\mathbf{g})^T \tag{5.3}$$

Note that the vector $\mathbf{g}$, expressing the magnitude and direction of gravity, is shown to have the same direction of $\hat{\mathbf{v}}$ in Figure 5.2. However, for later calculations it can be assumed as a rotating vector $\mathbf{g} = \mathbf{g}(\vartheta)$ to simulate the rotation of the gantry around the $\hat{\mathbf{u}}$ axis.

The effects on the cold mass position given by the deformation of supports is introduced in the IPK and DPK (Appendix A) by modifying the lengths of supports L_i in the following way:

$$L_i = L_{0_i}\left(1 + \frac{F_{q_i}}{AE}\right) \tag{5.4}$$

where L_{0_i} is the nominal length of supports, E is the Young's modulus of the material and A is the cross section area. Note that the Young's modulus E is assumed constant, that is not the case when one looks at the temperature gradient between warm and cold joints. However, this variation is assumed to be a second order effect and neglected in this model. Furthermore, the mathematical formulation given is completely general and a more detailed relation between E and the temperature considered as the integrated value can be added at any time in the future.

5.1.2 Deformation of the vacuum vessel due to cold-mass weight

Another error source to the final pose of the cold-mass is given by the flexibility of the vacuum vessel. Since the mathematical model requires different formulations, based

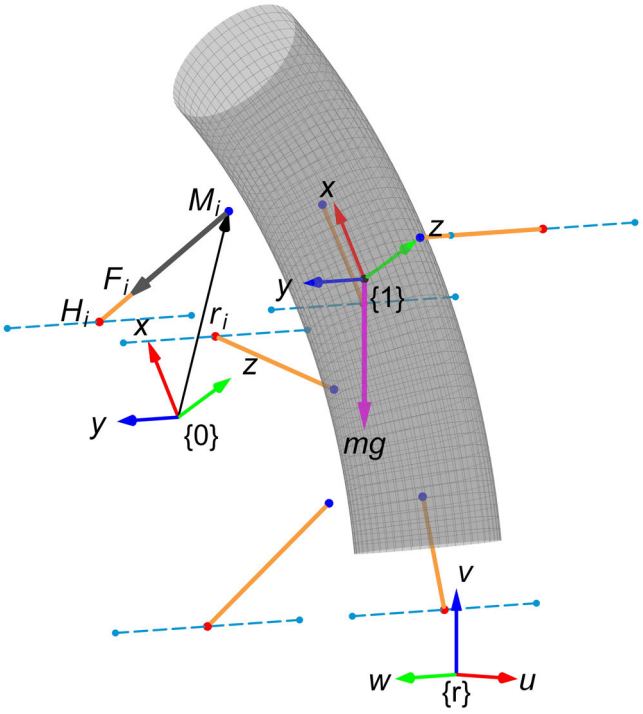

Figure 5.2: *Kinematic scheme of the cold-warm supporting system, reproducing the fourth dipole configuration and the forces acting on it.* $M\mathbf{g}$ *is the weight of the magnet applied to the center of gravity of the body while only one of the six forces acting on the magnet* $\mathbf{F}_{qi}$ *is displayed.*

on the nature of the load, it has been chosen to divide the error estimation in the three contributes:

1. due to cold-mass weight,
2. due to the weight of the vacuum vessel itself,
3. due to the differential pressure between vacuum and atmospheric.

A semi-analytic method is used combining measurements from FEA to define a flexibility tensor of the vacuum vessel $\mathbf{D}$. This method gives the possibility of checking the contribution of the vacuum vessel to the pose error at any angular position of the gantry, running only six FEA (one analysis for each support)

With reference to Figure 5.3, the displacement $\mathbf{\Delta}_i$ at each warm joint $\mathbf{H}_i$ can be expressed as a product of the tensor $\mathbf{D}$ and the vector of forces on actuated joints $\mathbf{F}_q$.

$$\Delta_{ij} = D_{ijk} F_q^k \quad \text{with} \quad \begin{cases} i = 1, \dots, 6 \\ j = 1, \dots, 3 \\ k = 1, \dots, 6 \end{cases} \tag{5.5}$$

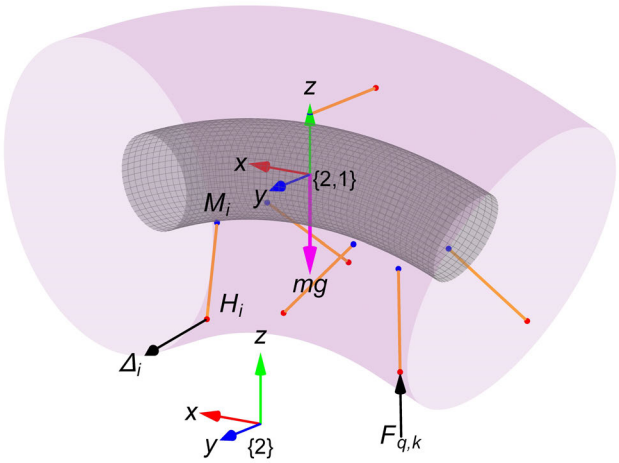

Figure 5.3: *Displacement $\mathbf{\Delta}_i$ at the interface $\mathbf{H}_i$ between the support (orange) and the vacuum vessel (in light purple) due to weight mg of the cold-mass. F_{q_k} is the force reaction developed by the rods on the vacuum vessel due to weight of the cold-mass.*

with the index i as the position at which the displacement is calculated, j for the component and k for the position where the reaction force is applied. This formulation is necessary because the displacement at one point of the vacuum vessel must consider the contribution to the deformation of the vacuum vessel given by a force applied at any of the warm interfaces. This is valid as long as deformations are small and the material is in the elastic range guaranteeing the applicability of the effects superposition principle.

The components of the flexibility tensor can be calculated by running six FEA, each one applying to the vacuum vessel a single arbitrary force in the direction of one of the support elements, changing each time the point of application. Each analysis gives as output the values of each component of the displacement Δ_{ijk} due to the application of the reaction force F_{q_k}. tensor components are calculated by normalizing the displacements of the vacuum vessel simulated in each of the 6 FEA by the force applied:

$$D_{ijk} = \frac{\Delta_{ijk}}{F_{q_k}} \tag{5.6}$$

Note that the components of the flexibility tensor are affected by the units in which the forces are applied and the displacements measured. Although an arbitrary value of the force could be used, the force must be small enough to not exceed the elastic range of the material. In contrast, to improve the accuracy of the definition of the tensor a non negligible force should be used. A force of 1000 N has been applied.

Summarizing, once the vacuum vessel flexibility has been characterized, displacements of the warm joints can be calculated at each position of the gantry, the missing step is related to the conversion of these displacements to the change in pose of the cold-mass. This is done by mean of the DPK replacing the target position of the warm joint ${}^0\mathbf{H}_i$ in Equation A.1 discussed in Section A.2 with a deformed configuration of joints ${}^2\mathbf{H}_i$

calculated as:

$$^{2}\mathbf{H}_{i} = {}^{2}\mathbf{H}_{0_i} + \mathbf{\Delta}_i + q_i\mathbf{h}_i \tag{5.7}$$

note that the direction of movement of the actuated joints does not require to be changed as the solution of the DPK is independent from the direction in which the warm prismatic joints are supposed to move. The initial joint vector containing q_i is calculated from the IPK on the deformed system.

5.1.3 Deformation of the vacuum vessel due to its own weight

The influence of the deformation of the vacuum vessel due to its own weight has been modelled using the same method described in the previous section. However, only two FEAs are performed for the vacuum vessel instead of six: the first being with gravity in vertical direction (gantry at position $\theta = 0°$) and the second with gravity in orthogonal direction with respect to the first analysis (gantry at position $\theta = 90°$).

$$\Delta_{ij} = D_{ijk}F_{g_k} \quad \text{with} \quad \begin{cases} i = 1, \ldots, 6 \\ j = 1, \ldots, 3 \\ k = 1, 2 \end{cases} \tag{5.8}$$

with the index i as the position at which the displacement is calculated, j for the component and k for the directions of gravity in the two simulations. The coefficients of the elasticity tensor are equivalent to the displacements measured on each warm joint from the two FEAs. Hence, $\mathbf{F}_g$ is a unit vector that describes the rotation of the gravity vector with respect to the reference system fixed to the cold-mass and F_{g_k} are its components:

$$\mathbf{F}_g = (Cos(\theta), Sin(\theta))^T \tag{5.9}$$

The modified positions of the actuated joints for the DPK is:

$$^{2}\mathbf{H}_{i} = {}^{2}\mathbf{H}_{0_i} + \mathbf{\Delta}_{CM_i} + \mathbf{\Delta}_{OW_i} + q_i\mathbf{h}_i \tag{5.10}$$

where the index "CM" and "OW" are used to differentiate the displacement contribution given respectively by the cold-mass weight and the own weight of the vacuum vessel.

5.1.4 Deformation of the vacuum vessel due to differential pressure

The effect of the deformation of the vacuum vessel due to the differential pressure is just taken as a measured displacement from an additional FEA with pressure as the only load on the vacuum vessel.

The modified positions of the actuated joints for the DPK is:

$$\begin{aligned} ^{2}\mathbf{H}_{i} &= {}^{2}\mathbf{H}_{0_i} + \mathbf{\Delta}_i + q_i\mathbf{h}_i \quad \text{with} \\ \mathbf{\Delta}_i &= \mathbf{\Delta}_{CM_i} + \mathbf{\Delta}_{OW_i} + \mathbf{\Delta}_{V_i} \end{aligned} \tag{5.11}$$

where the index "V" is used to differentiate the displacement contribution given by the differential pressure.

5.1.5 Backlash effect

Without any compensation method, the proposed supporting architecture will be subject to an error related to backlash of each of the 12 spherical joints. A 1D scheme of the effect of backlash can be seen in Figure 5.4.

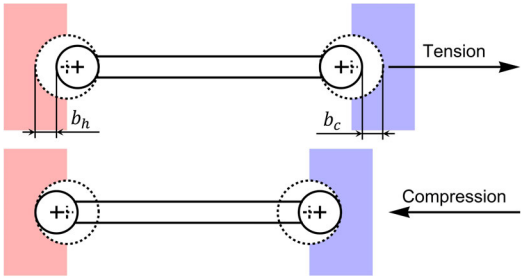

Figure 5.4: *1D representation of the effect of backlash for a support element under tension and compression respectively. In red the vacuum vessel and in blue the cold mass.*

As shown in the 1D scheme, assuming as the warm joint the red rectangle, the real position of cold joint (blue rectangle) depends on the sign of the reaction on the support. Generalizing to the 3D case, the real position of the joints (${}^{2,1}\mathbf{M}_{r_i}$ or ${}^{2}\mathbf{H}_{r_i}$) is assumed to be always on the line passing through the nominal joints (${}^{2,1}\mathbf{M}_{\mathrm{nom}_i}$ and ${}^{2}\mathbf{H}_{\mathrm{nom}_i}$):

$$ {}^{2,1}\mathbf{M}_{r_i} = \begin{cases} {}^{2,1}\mathbf{M}_{\mathrm{nom}_i} - \frac{b_c}{2}\mathbf{w}_i & \text{if} \quad F_{q_i} > 0 \\ {}^{2,1}\mathbf{M}_{\mathrm{nom}_i} + \frac{b_c}{2}\mathbf{w}_i & \text{if} \quad F_{q_i} < 0 \end{cases} \tag{5.12} $$

$$ {}^{2}\mathbf{H}_{r_i} = \begin{cases} {}^{2}\mathbf{H}_{\mathrm{nom}_i} + \frac{b_h}{2}\mathbf{w}_i & \text{if} \quad F_{q_i} > 0 \\ {}^{2}\mathbf{H}_{\mathrm{nom}_i} - \frac{b_h}{2}\mathbf{w}_i & \text{if} \quad F_{q_i} < 0 \end{cases} \tag{5.13} $$

where, b_c and b_h are the values of backlash (radial internal clearance) respectively of cold and warm joints; $\mathbf{w}_i$ gives the direction of the nominal support element as defined in Equation 5.2. Note that cold joints positions must be defined in the $\{2, 1\}$ frame fixed with respect to the cold-mass as shown in Figure 5.3. Note that the real position of joints is not well defined when the force on support is absent ($F_{q,i}(\theta_0) = 0$) because only two positions of the joints are stable as showed in Figure 5.4. In the implementation of the algorithm this can be fixed by calculating F_{q_i} for $\theta = \theta_0^-$ or $\theta = \theta_0^+$ in accordance with the rotation direction of the gantry.

The superposition of this effect with the others described before is done by running the DPK algorithm using for the warm joints Equation 5.13 assuming ${}^{2}\mathbf{H}_{\mathrm{nom},i} = {}^{2}\mathbf{H}_i$ where the right hand side comes from Equation 5.11. Then, both ${}^{2}\mathbf{H}_{r_i}$ and ${}^{2,1}\mathbf{M}_{r_i}$ replace ${}^{0}\mathbf{H}_i$ and ${}^{1}\mathbf{M}_i$ respectively in the DPK in Section A.2.

5.1.6 Displacements due to the cool-down process in solution 6S

In order to consider the cool-down effect for the 6S LPM, few modifications are needed. L_{0i} must be used as the length at cold by correcting it by a thermal contraction δ_s (see Equation 5.30 in Section 5.3). Additionally, the position of the cold joints ${}^{2,1}\mathbf{M}_{r_i}$ in the

local frame $\{2, 1\}$ (Figure 5.3) must updated to the position at cold as explained at the very end of Section 5.3. These changes must be done to all above mentioned equations.

5.2 Statically Indeterminate General Lumped Parameter Model

For the over-constrained suspension systems of cryogenic devices the application of concepts of DPK are not deemed possible, because DPK is based on a geometric solution. Even if the LPM for solution 6S introduces modification to it as the form of deformations or contractions of the supports, those are independent from a support to another. Indeed, being solution 6S the bodies can be seen as shortened bodies displaced only by rigid body motion. In a LPM for the statically indeterminate system the calculation of loads and consequently deformation must take into account that the stress and deformation state of each support is influenced by the state of all the others. A comprehensive review of the over-constrained parallel mechanisms [99], which were used for different applications, describes different methods to solve the statically indeterminate system associated to a parallel mechanism under external loads. However, the contribution of a thermal gradient on the supports is not considered. This is of paramount importance for the application of passive parallel mechanisms studied in this article. The solution provided in this chapter is based on an energy based approach such as the Principle of virtual work [100, 101]. A generic model based on this principle and applicable to any arrangement of any number of linking bar supports ($n > 6$) is formulated in this section.

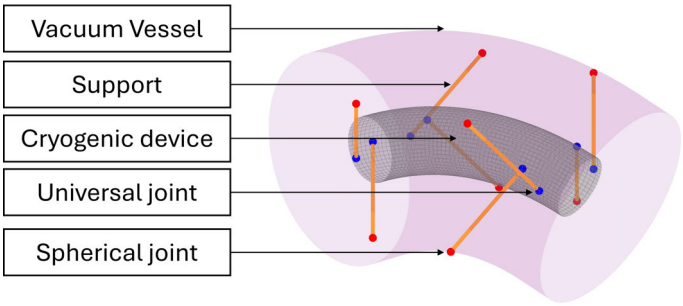

Figure 5.5: *Cryogenic device (gray) supported by eight supports (orange) joined to it by mean of universal joints (blue) and to the vacuum vessel (pink) by mean of spherical joints (red).*

The suspension system in Figure 5.5 is composed of n supports (a symmetric eight support architecture is shown for simplicity). Each of the $n+1$ bodies, one cold mass and n supports, has six DOFs in the 3D space, the full system has therefore $6(n+1)$ DOFs. The Model is limited to the use of spherical or a combination of spherical and universal joints at the end of each support. The choice of using only spherical and universal joints results in a support which gets loaded only axially, making it convenient to limit stresses allowing the designer to size a smaller cross section for the support reducing the heat-flux to the cold mass. Spherical joints lock the three translations of a body while universal joints lock three translations and one rotation. Different joint combinations would introduce bending, shear, or torque in the supports, necessitating bulkier supports to manage stress

levels, thereby increasing heat load . This system of joints is locking a total of $3n+4n = 7n$ DOFs, hence the system is $n-6$ times over-constrained. Substituting n universal joints with n spherical joints lowering the number of DOFs locked to $6n$ does not make the system exactly constrained. This is because the n DOFs that are freed are the rotations of the supports around their longitudinal axis, which are internal degrees of freedom. The cryogenic device would still have $n-6$ missing equations to find all reactions.

The selected and commonly used method for the solution of over-constrained systems is the Principle of virtual work [100, 101] which equates the virtual work done by internal actions $\mathcal{W}_{\text{int}}$ by the one done by external reactions $\mathcal{W}_{\text{ext}}$:

$$\mathcal{W}_{\text{int}} = \mathcal{W}_{\text{ext}} \tag{5.14}$$

Even if theoretically all internal actions contribute to the work, some contributions can be eliminated because of considerations on the joints used: the only load that can generate torque, shear and bending moments on the supports is external acceleration (in the example used is gravity). This contribution is negligible since the mass of supports is orders of magnitude smaller that the mass of the cryogenic device. All internal actions on the cryogenic device contribute minimally if the stiffness of the cryogenic device is much higher than the stiffness of the supports. The remaining actions contributing to the internal work are the eight axial actions of the supports.

The Principle of virtual work applied to over-constrained structures requires to find a compatible exactly-constrained structure where enough constraints are substituted with an equal number of variables. A total of $n-6$ X_m variables are introduced to eliminate the $n-6$ extra constrains resulting in the compatible structure represented in Figure 5.6.

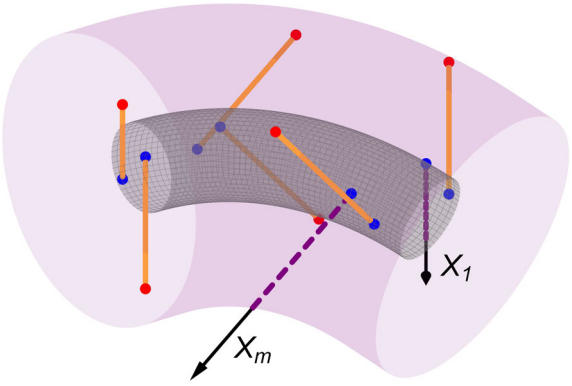

Figure 5.6: *Compatible exactly constrained structure with over-constrain variables $X_1, ..., X_m$. In purple the supports where constraints have been substituted with over-constrained variables*

The Principle of virtual work requires to find the internal actions for $n-5$ cases of the compatible structure, as clarified in the following list:

- one compatible structure where only external loads are applied, used to calculate $\mathbf{N}_0$: the vector containing internal actions on each support;

- $n-6$ compatible structures where the over-constrain variables X_m are applied one by one as unitary loads, used to calculate $\mathbf{N}_{X_m}$: the vector containing the internal actions on each support.

A system of $n-6$ equations must be written to calculate all $n-6$ over-constrain variables X_m, each equation of the form of Equation 5.15.

$$\sum_{i=1}^{n} \int_0^{L_i} N_{X_{mi}} \left(\frac{N_{0i} + \sum_{p=1}^{n-6} X_p N_{X_{pi}}}{E_i A_i} + \frac{\delta_i}{L_i} - \frac{\delta_{P_i}}{L_i} \right) ds = \mathcal{W}_{\text{ext}_{Xm}} \tag{5.15}$$

where δ and δ_P add the contributions respectively of the thermal differential contraction/-expansion (see Section 5.3) and the pre-load in terms of length adjustment. Additionally, each support is described by a unique length L_i, cross section A_i and material Young Modulus E_i.

The axial actions due to over-constrain variables can be written as:

$$N_{X_{mi}} = \begin{cases} \widetilde{N}_{X_{mi}} & \text{for} \quad i = 1, \dots, 6 \\ 1 & \text{for} \quad i = m+6 \\ 0 & \text{Otherwise} \end{cases} \tag{5.16}$$

all other components except for $i \leq 6$ and $i = m+6$ are null because the warm joints of respective legs in the compatible structure are not constrained axially. The i-th leg with $i = m+6$ has a unitary load deriving from the Principle of virtual work solving procedure. The compatible exactly constrained structure, composed of six supports, is known in robotics as hexapod. Equations developed in robotics [102] can be used to write in a compact form equilibrium equations for the compatible structure and find the internal actions on supports:

$$\widetilde{\mathbf{N}}_{X_m} = \mathbf{J}^{-T} \mathbf{F}_m \tag{5.17}$$

where:

$$\mathbf{F}_m = (-\mathbf{w}_{m+6}, -\mathbf{u}_{m+6})^T \tag{5.18}$$

$\mathbf{J}$ is the geometrical Jacobian matrix defined already in Equation 5.2. Note that $\mathbf{J}$ must be calculated on the compatible exactly constrained structure.

Similarly, for the axial actions due to external forces:

$$N_{0i} = \begin{cases} \widetilde{N}_{0i} & \text{for} \quad i = 1, \dots, 6 \\ 0 & \text{for} \quad i = 7, \dots, n \end{cases} \tag{5.19}$$

with

$$\widetilde{\mathbf{N}}_0 = \mathbf{J}^{-T} \mathbf{F}_s \tag{5.20}$$

the external work can be written as:

$$\mathcal{W}_{\text{ext}_{X_m}} = \mathbf{d} \cdot \mathbf{N}_{X_m} \tag{5.21}$$

with $d_i = -\boldsymbol{\Delta}_i \cdot \mathbf{w}_i$.

The different contributions to the warm joints displacement $\mathbf{\Delta}_i$ such as the deformation of the vacuum vessel due to the cold mass weight, due to the vacuum vessel own weight and the pressure difference between exterior and interior of the vessel are introduced as it follows:

$$\mathbf{\Delta}_i = \mathbf{\Delta}_{CM_i} + \mathbf{\Delta}_{OW_i} + \mathbf{\Delta}_{V_i} \tag{5.22}$$

where the index "CM", "OW" and "V" are used to differentiate the displacement contribution given respectively by the cold-mass weight, the weight of the vacuum vessel and the vacuum. The different terms of the warm joints displacement are calculated as follows:

$$\Delta_{CM_{il}} = D_{CM_{ilk}} \left(N_{0k} + \sum_{p=1}^{n-6} X_p N_{X_{pk}} \right) \tag{5.23}$$

$$\Delta_{OW_{il}} = D_{OW_{ilk}} F_{g_k} \tag{5.24}$$

with $\mathbf{F}_g = (Cos(\theta), Sin(\theta))$. $\mathbf{\Delta}_{V_i}$ is measured directly from FEAs as done for the 6S LPM and the compliance matrices D_{ilk} are defined in the same way as in Section 5.1.

Once all X_m are known, the Principle of virtual work can be applied again to extract the pose (position and rotation) $\mathbf{e} = (e_x, e_y, e_z, \theta_x, \theta_y, \theta_z)$ of the cryogenic device by solving six independent equations of the form: Equation 5.25. Each equation requires to calculate the internal actions $\mathbf{N}_j$ on each support when an unitary force/torque is applied to the compatible structure.

$$\sum_{i=1}^{n} \int_0^{L_i} N_{ji} \left(\frac{N_{0i} + \sum_{p=1}^{n-6} X_p N_{Xpi}}{E_i A_i} + \frac{\delta_i}{L_i} - \frac{\delta_{P_i}}{L_i} \right) ds = \mathbf{d} \cdot \mathbf{N}_j + e_j = \mathcal{W}_{\text{ext}_j} \tag{5.25}$$

where the internal actions $\mathbf{N}_j$ used for the calculation of the pose are found as:

$$N_{ji} = \begin{cases} \widetilde{N}_{ji} & \text{for} \quad i = 1, \ldots, 6 \\ 0 & \text{for} \quad i = 7, \ldots, n \end{cases} \tag{5.26}$$

and

$$\widetilde{\mathbf{N}}_j = \mathbf{J}^{-T} \mathbf{F}_j \tag{5.27}$$

where $F_{ji} = 1$ for $i = j$ and 0 otherwise.

5.3 Influence of the differential thermal contraction

In the LPM for the statically indeterminate systems, the thermal contraction of the cold mass and of the supports is introduced as a virtual internal strain on the supports $\varepsilon_T = \delta / L$. The thermal expansion δ originates from two contributions: the contraction of the cold mass δ_{CM} and the contraction of the support δ_s. In the LPM of solution 6S the contribution of δ_s is introduced to modify the length of the supports while δ_{CM} is introduced in Subsection 5.1.6 differently as explained in that section.

$$\delta = \delta_{CM} + \delta_s \tag{5.28}$$

The coefficient of linear expansion depends on the temperature, to get the length of a rod at a given temperature L_T the integral form of the coefficient is used:

$$L_T - L_{293} = I(T)L_{293} \tag{5.29}$$

The function of $I(T)$ for different material can be found on [81]. This is however the case of a rod that is initially at temperature $T = 293\,\mathrm{K}$ and it is cooled homogeneously at a given temperature T. In the study case this is not valid as there is a strong temperature gradient along the length of the supports where the cold end is at around $5\,\mathrm{K}$ and the warm end at $293\,\mathrm{K}$. Thus an integral form of Equation 5.29 must be used:

$$\delta_s = \int_0^L I(T(s))\,ds \tag{5.30}$$

the temperature along the length L of a rod with its extremities at temperatures T_0 and T_L can be found by solving differential equations of Fourier's law:

$$\frac{\partial}{\partial s}\left(k\frac{\partial T}{\partial s}\right) + \dot{q} = \rho c\frac{\partial T}{\partial t} \tag{5.31}$$

supposing to be in steady state $\dfrac{\partial T}{\partial t} = 0$ and that there are no heat sources within the support $\dot{q} = 0$, the Fourier's law becomes:

$$\frac{\partial k}{\partial T}\left(\frac{\partial T}{\partial s}\right)^2 + k\frac{\partial^2 T}{\partial^2 s} = 0 \tag{5.32}$$

where $k = k(T)$. Looking at the thermal conductivity of the possible materials for supports [81] their thermal conductivity appears to be proportional to $\sqrt{T}$ so that $k \simeq a\sqrt{T}$. Substituting in Equation 5.32 and solving the differential equations with boundary conditions $T(0) = T_0$ and $T(L) = T_L$ yelds:

$$T(s) = \left(-\frac{LT_0^{\frac{2}{3}} - T_0^{\frac{2}{3}}s + T_L^{\frac{2}{3}}s}{L}\right)^{\frac{2}{3}} \tag{5.33}$$

The real function $T(s)$ is written in a piece-wise form because of the presence of an intermediate thermalization T_{th} of length L_{th} between the warm T_a and cold T_c parts of the support of lengths L_w and L_c respectively:

$$T(s) = \begin{cases} \left(-\dfrac{L_w T_a^{\frac{2}{3}} - T_a^{\frac{2}{3}} s + T_{th}^{\frac{2}{3}} s}{L_w} \right)^{\frac{2}{3}} & \text{for} \quad 0 \leq s < L_w \\ T_t h & \text{for} \quad L_w \leq s < L_w + L_{th} \\ \left(-\dfrac{L_w T_{th}^{\frac{2}{3}} - T_{th}^{\frac{2}{3}}(s - L_w - L_{th}) + T_c^{\frac{2}{3}}(s - L_w - L_{th})}{L_c} \right)^{\frac{2}{3}} & \text{for} \quad L_w + L_{th} \leq s \leq L \end{cases} \tag{5.34}$$

Codes of numerical integration can be used to integrate Equation 5.30 with Equation 5.34 to get δ_s.

If the contraction of the support and the contraction of the cold mass are in opposite directions, due to the contraction of the cold mass a support of nominal length should stretch even more for the system to be in equilibrium. In equilibrium $L_e = \| {}^0\mathbf{M}_{c_i} - {}^0\mathbf{H}_i \|$ where $\mathbf{M}_{c_i}$ is the i-th cold joint position at cold. In order to have a coherent math $\delta_{CM} = L - L_e$, so that $\delta_{CM} + \delta_s$ represents the total elongation that the support should reach in equilibrium. Even if the contractions are in the same direction the math is coherent with this sign convention. The cold joints position at cold is calculated as it follows $\mathbf{M}_{c_i} = \mathbf{M}_i I(T_c)$ both in case of 6S and the over-constrained solutions.

5.4 Particularization of statically indeterminate LPM to solution 8S

For the particular case of the LPM for a suspension architecture that uses eight equal supports, the system is twice over-constrained. A system of two equations (equal to the number of over-constrain variables unknown) is written to solve for X and Y (Equation 5.35).

$$\begin{cases} \displaystyle\int_0^L \mathbf{N}_X \cdot \left(\frac{\mathbf{N}_0 + X\mathbf{N}_X + Y\mathbf{N}_Y}{EA} + \frac{\delta}{L} - \frac{\delta_P}{L} \right) ds = \mathcal{W}_{\text{ext}_X} \\ \displaystyle\int_0^L \mathbf{N}_Y \cdot \left(\frac{\mathbf{N}_0 + X\mathbf{N}_X + Y\mathbf{N}_Y}{EA} + \frac{\delta}{L} - \frac{\delta_P}{L} \right) ds = \mathcal{W}_{\text{ext}_Y} \end{cases} \tag{5.35}$$

The internal actions $\mathbf{N}_0$ given by an external load are calculated as:

$$N_{0i} = \begin{cases} \widetilde{N}_{0i} & \text{for} \quad i = 1, \ldots, 6 \\ 0 & \text{for} \quad i = 7, 8 \end{cases} \tag{5.36}$$

where $\widetilde{\mathbf{N}}_0 = \mathbf{J}^{-T}\mathbf{F}_s$

Similarly the axial reactions are written for the two virtual structure where each hyperstatic virtual load is applied:

$$N_{X_i} = \begin{cases} \widetilde{N}_{X_i} & \text{for} \quad i = 1, \dots, 6 \\ 1 & \text{for} \quad i = 7 \\ 0 & \text{for} \quad i = 8 \end{cases} \tag{5.37}$$

and

$$N_{Y_i} = \begin{cases} \widetilde{N}_{Y_i} & \text{for} \quad i = 1, \dots, 6 \\ 0 & \text{for} \quad i = 7 \\ 1 & \text{for} \quad i = 8 \end{cases} \tag{5.38}$$

where:

$$\widetilde{\mathbf{N}}_X = \mathbf{J}^{-T}\mathbf{F}_{X_s} \quad \text{and} \quad \mathbf{F}_{X_s} = (-\mathbf{w}_7, -\mathbf{u}_7)^T$$

$$\widetilde{\mathbf{N}}_Y = \mathbf{J}^{-T}\mathbf{F}_{Y_s} \quad \text{and} \quad \mathbf{F}_{Y_s} = (-\mathbf{w}_8, -\mathbf{u}_8)^T$$

Once X and Y are known, the Principle of virtual work can be applied to extract the pose (position and rotation) $\mathbf{e} = (e_x, e_y, e_z, \theta_x, \theta_y, \theta_z)$ of the cryogenic device by solving six independent equations of the form: Equation 5.39.

$$\int_0^L \mathbf{N}_j \cdot \left(\frac{\mathbf{N}_0 + X\mathbf{N}_X + Y\mathbf{N}_Y}{EA} + \frac{\delta}{L} - \frac{\delta_P}{L} \right) ds = \mathcal{W}_{\text{ext}_j} \tag{5.39}$$

the internal actions used for the calculation of the pose are found as:

$$N_{ji} = \begin{cases} \widetilde{N}_{ji} & \text{for} \quad i = 1, \dots, 6 \\ 0 & \text{for} \quad i = 7, 8 \end{cases} \tag{5.40}$$

and

$$\widetilde{\mathbf{N}}_j = \mathbf{J}^{-T}\mathbf{F}_j \tag{5.41}$$

where $F_{ji} = 1$ for $i = j$ and 0 otherwise.

6 VALIDATION OF THE LUMPED PARAMETER MODELS

The models developed in Chapter 5 have been validated by comparing their results with thermo-mechanical simulations obtained from a widely used FEA software(*Ansys® Workbench, 2022 R2*). The validation of both models developed in this work has been conducted separately, as outlined below.

1. the first two studies are done in order to validate the general formulation of the model for any number of supports and a generic disposition of those (model described by Equation 5.15 and Equation 5.25). In these studies a generic eight support geometry and a generic eleven support geometry have been used as geometries.
2. the validation of the 6S LPM is done directly on the case study of the gantry. An initial benchmark analysis examines the effects of gravity, pre-load, temperature, and pressure on the pose of the magnet during the rotation of the gantry. A second benchmark is conducted to validate the section of the LPM that describes the influence of backlash on the pose of the magnet.
3. finally, a benchmark analysis examines the solution 8S applied to the study case of the gantry with the same methodology used for the LPM of solution 6S.

6.1 Validation of the generic over-constrained LPM

Similarly to what has been done for the LPM of solution 6S, static steady state thermo-mechanical analysis are used to benchmark the LPM proposed for generic over-constrained supporting systems. The materials used, loads applied and boundary conditions of the models are explained in the following paragraphs:

- **Geometry**:
  Eight or eleven supports constitute the supporting system of a generic cryogenic device Figure 6.1. The supports connect the cold mass to the external vacuum vessel. The disposition of supports has been randomly generated for the 11-supports configuration to prove that the mathematical model developed can be adapted to non-symmetrical configurations too. The 8-supports configuration is the same of the 11-supports were three supports have been suppressed. Eleven has been chosen as an arbitrary number greater than eight (one of the most common supporting architecture [95]).
- **Material**:
  Temperature dependent coefficient of thermal expansion and thermal conductivity of Stainless steel 304 [81] are being used to define the properties of the steel material applied to supporting elements. Isotropic instantaneous coefficient of thermal expansion and isotropic coefficient of thermal conductivity are used in material model definition (Figure 6.2).

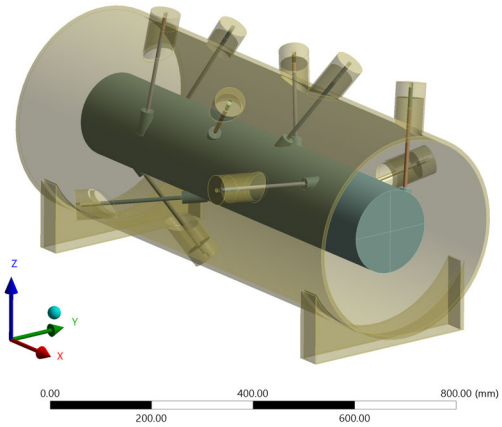

Figure 6.1: *Model used for the validation of the LPM. 11 supporting rods attached to the vacuum vessel and the cold mass. The model used for the validation of eight supports is the same as for the eleven rods with three random rods suppressed. Images used courtesy of ANSYS, Inc*

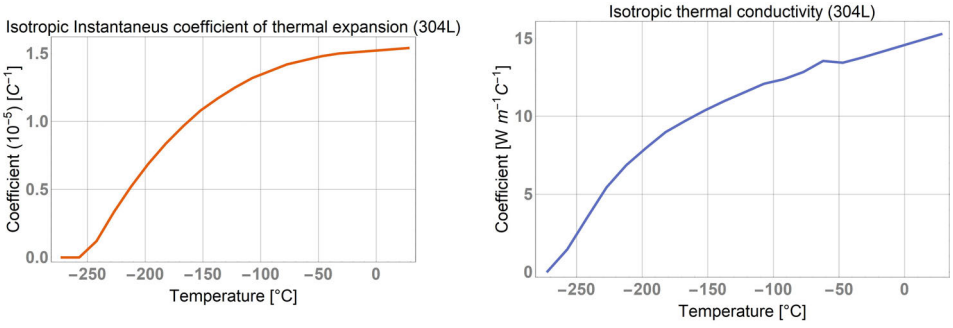

Figure 6.2: *Data used to define thermal expansion and conductivity.*

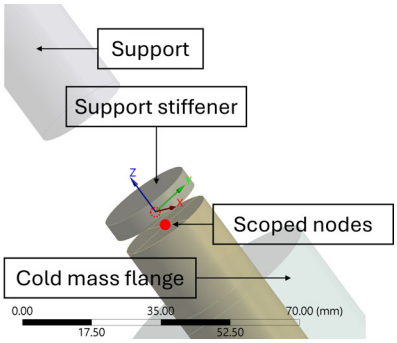

Figure 6.3: *Support stiffeners section and joint definition in ANSYS. Images used courtesy of ANSYS, Inc*

- **Interactions**:
  Spherical joints and bushing joints (general Ansys joint defined by stiffness parameters) have been used to simulate the joints between the supports and the vacuum vessel or supports and cold-mass. Both types of joints have been scoped to single nodes on the surfaces of the bodies to join (see Figure 6.3). A short section of supports act as stiffener (see Figure 6.3), this section is assigned with a 1000 times stiffer steel, it avoids the elements near the nodes scoped for the joints to deform excessively. Bushings are used to formulate an universal joint by defining the stiffness associated with the degrees of freedom to lock between the nodes, a value of $1 \times 10^9\,\mathrm{N\,mm^{-1}}$ is assigned to stiffen the relative translations along x, y and z (longitudinal axis of the supports) and a value of $1 \times 10^7\,\mathrm{N\,mm/deg}$ assigned to the stiffness of rotations around z (simulating the universal joints). The selected stiffness values, in relation to the expected loads on supports, result in negligible deformations at the joints simulating an ideal spherical or universal joint. The different stiffness values between translational and rotational DOFs have been set to solve FEA convergence problems that were present if the same value was used.
- **Loads**
  To validate the general validity of the model, six different loading conditions have been applied in this simulation: forces F_x, F_y, F_z and moments M_x, M_y, M_z are applied separately in each of the six steps (Table 6.1). The values of F_x, F_y, F_z have been chosen proportional with the mass of the drawn cold mass (about three times), while M_y, M_z have been chosen by applying the same value of force of F_x, F_y, F_z at a distance from the center proportional to the diameter of the drawn cold mass. Note that M_x is five times lower than other applied moments because otherwise, one support would buckle under compression, rendering the results of the FEAs and LPM drastically different. Given that the scope of this model is not to assess the position of a cryogenic device with supports in buckling conditions, the validation is not impacted. The vacuum of $-0.1\,\mathrm{MPa}$ is applied to the vacuum vessel's internal surfaces. Pre-load has been applied by defining translation joints and applying joint load as displacement ($\delta = 0.5\,\mathrm{mm}$). Both vacuum and pre-load are applied before

Table 6.1: *Loading conditions the validation models.*

Step	F_x kN	F_y kN	F_z kN	M_x kN m	M_y kN m	M_z kN m
1	5	0	0	0	0	0
2	0	5	0	0	0	0
3	0	0	5	0	0	0
4	0	0	0	0.4	0	0
5	0	0	0	0	2	0
6	0	0	0	0	0	2

step 1 together with Temperature stationary boundary conditions of 22 °C on the vacuum vessel and −268 °C on the cold mass.

The pose of the cryogenic device has been calculated by means of the LPM. The qualitative agreement with the LPM is reported in Figure 6.4. Table 6.3 and Table 6.2 report the values of all pose components for each loading case (see Table 6.1) as simulated by FEAs. Additionally, figures of merit such as the absolute error Err = LPM − FEA and relative error %Err = |Err|/FEA ∗ 100 are calculated to express the accuracy of the developed model with respect to FEA. The maximum absolute error between the two models in estimating the position of the supported object is 13 µm and 26 µm, while for rotations is 52 µrad and 99 µrad. For the pose, there is the same issue in estimating the overall accuracy of the model as for the internal actions. Specifically, a high relative error is shown for d_y during the sixth load case in Table 6.2. Here, the absolute disagreement between the two models is very low: about 2 µm for a nominal value of 10 µm thus the high relative error. In a real application, displacements so small are fully within the required accuracy of the system (see Table 3.1) and are even outside of the sensitivity of measurement instruments. Therefore, the model's accuracy has been characterized using the median of all calculated relative errors. Even though some high errors appear in particular cases, the median of all errors is only about 0.6% and 1.4% respectively for the eight and eleven support study cases, confirming for the pose a very good agreement of the developed model with FEAs. The accuracy slightly decreases for the model with eleven supports but is still accurate enough to be used in optimization processes, the comparison of different material and dimensional solutions, and sensitivity analysis.

Internal actions on supports are calculated from LPM using $N_{0,i} + \sum_{m=1}^{n-6} X_m N_{X_m,i}$; the values of all over-constrained variables X_m are calculated from Equation 5.15. The same internal actions are evaluated from FEA by probing joint loads. As mentioned in Table 6.1, loads are applied in six different steps of the simulation. The values calculated with the LPM are in good agreement with those simulated by FEAs for both the eight and eleven support study cases (Figure 6.5).

Table 6.4 and Table 6.5 report values of internal axial load on each support for each loading case simulated with FEA. Similarly, as it was performed for the pose, the same tables report the absolute error Err and relative error %Err. The maximum absolute error found is relatively low, about 360 N and 400 N if compared to a maximum force of 37 kN and 51 kN respectively for the eight and eleven supports study cases. Maximum absolute

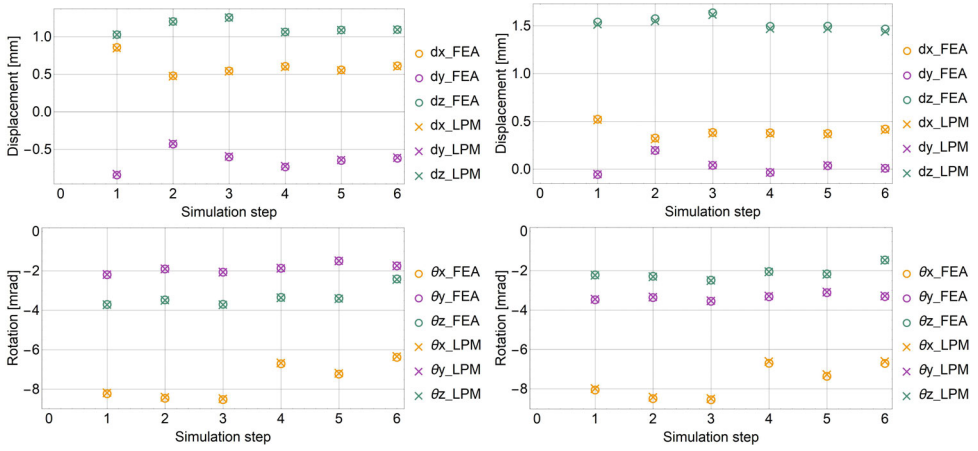

(a) *eight supports.* **(b)** *eleven supports.*

Figure 6.4: *Comparison of the pose (displacement and rotation) of the cold-mass between the LPM (cross) and FEA (circle).*

Table 6.2: *Errors for each DOF for the model with eight supports.*

	Step	dx mm	dy mm	dz mm	θx mrad	θy mrad	θz mrad
FEA	1	0.86	−0.84	1.03	−8.23	−2.19	−3.7
	2	0.48	−0.43	1.2	−8.46	−1.91	−3.48
	3	0.55	−0.6	1.26	−8.53	−2.07	−3.7
	4	0.61	−0.74	1.06	−6.72	−1.88	−3.35
	5	0.56	−0.65	1.09	−7.24	−1.5	−3.39
	6	0.61	−0.62	1.09	−6.39	−1.75	−2.42
Err	1	−0.011	0.013	−0.001	0.045	0.01	−0.016
	2	−0.007	0.009	−0.004	0.052	0.006	−0.019
	3	−0.007	0.01	−0.004	0.051	0.008	−0.017
	4	−0.009	0.012	−0.002	0.046	0.007	−0.016
	5	−0.008	0.011	−0.002	0.046	0.004	−0.017
	6	−0.008	0.01	−0.003	0.048	0.006	−0.02
% Err	1	1.2	1.6	0.1	0.6	0.5	0.4
	2	1.4	2	0.3	0.6	0.3	0.5
	3	1.4	1.6	0.3	0.6	0.4	0.5
	4	1.4	1.6	0.2	0.7	0.4	0.5
	5	1.4	1.7	0.2	0.6	0.3	0.5
	6	1.4	1.7	0.2	0.8	0.4	0.8

Table 6.3: *Errors for each DOF for the model with eleven supports.*

	Step	dx mm	dy mm	dz mm	θx mrad	θy mrad	θz mrad
FEA	1	0.52	−0.06	1.54	−8.06	−3.47	−2.21
	2	0.33	0.2	1.57	−8.49	−3.37	−2.29
	3	0.38	0.04	1.64	−8.56	−3.55	−2.48
	4	0.38	−0.04	1.49	−6.7	−3.32	−2.04
	5	0.37	0.04	1.5	−7.36	−3.12	−2.16
	6	0.42	0.01	1.47	−6.7	−3.31	−1.46
Err	1	−0.008	0.002	−0.024	0.071	0.028	−0.018
	2	−0.009	0.004	−0.024	0.072	0.032	−0.017
	3	−0.008	0.003	−0.021	0.063	0.026	−0.022
	4	−0.009	0.002	−0.025	0.092	0.03	−0.014
	5	−0.009	0.003	−0.026	0.085	0.035	−0.015
	6	−0.009	0.002	−0.026	0.099	0.031	−0.007
% Err	1	1.4	3.7	1.6	0.9	0.8	0.8
	2	2.8	2	1.5	0.8	0.9	0.7
	3	2.1	8.9	1.3	0.7	0.7	0.9
	4	2.3	6.6	1.6	1.4	0.9	0.7
	5	2.5	9	1.8	1.2	1.1	0.7
	6	2.2	24.1	1.8	1.5	0.9	0.5

errors occur for high values of the internal actions; therefore, the relative error is relatively small. High relative errors (%Err = |Err|/FEA ∗ 100) can be found for those supports that are minimally loaded; for example, on the seventh rod of the eight support supporting system for the sixth load case. The two models, in this particular case, disagree by only 52 N in absolute terms. The axial load is around 100 N for that support; thus, the relative error is high. The same issue is highlighted for the eleven support supporting system (Table 6.5). In this case rod 3 shows a very small disagreement of 7 N but on a nominal value of about 14 N, consequently the relative error is high. While sizing supports, the engineering focus is more on the maximally loaded supports, where the model shows lower relative errors. An overall figure of merit chosen to describe the accuracy of the model is, therefore, the median of all relative errors (used from now on), which is about 1.1% and 1.4% respectively for the eight and eleven support study case. This quantitatively confirms the very good agreement of the model with FEAs. Although the accuracy slightly decreases with a larger number of rods, the model can be judged reliable.

The validation highlights the ability of the model to correctly estimate interesting quantities such as loads and position of objects in a general way. The validation proves the effectiveness of the model in predicting those quantities, even for support configurations that are highly non-symmetrical.

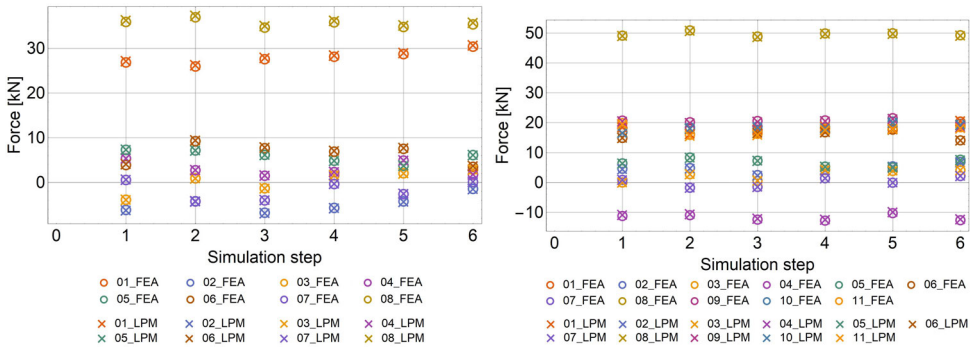

(a) *eight supports.* **(b)** *eleven supports.*

Figure 6.5: *Comparison of the force on each support between the LPM (cross) and FEA (circle).*

Table 6.4: *Absolute and relative errors of internal actions on each support for the eight supports study case.*

	Step	rod 1	rod 2	rod 3	rod 4	rod 5	rod 6	rod 7	rod 8
FEA (kN)	1	26.8	−6.2	−3.9	5.4	7.3	3.9	0.6	35.9
	2	25.9	−4.2	0.9	2.7	7.2	9.2	−4.3	36.9
	3	27.6	−6.8	−1.3	1.5	6.1	7.6	−4.0	34.6
	4	28.1	−5.7	1.6	2.3	4.8	6.9	−0.4	35.8
	5	28.7	−4.3	2.0	4.9	3.7	7.5	−2.6	34.8
	6	30.4	−1.4	2.9	1.8	6.1	3.5	0.1	35.4
Err (N)	1	274.9	−79.6	0.7	21.2	−2.5	176	43	360
	2	271	−75.3	−33.6	42.7	−10.2	173.5	62	352.4
	3	273.5	−74.9	−28.2	41.5	−3.2	166.7	54.2	357.9
	4	265	−76.7	−6.8	24.6	−6	172.7	47.5	347
	5	269.6	−75.1	−21.9	35.4	−4.8	168.5	52.6	350.9
	6	273.5	−78.4	−13.6	26	−7.2	177.7	51.6	350.6
% Err	1	1	1.3	0	0.4	0	4.5	7.6	1
	2	1	1.8	3.7	1.6	0.1	1.9	1.5	1
	3	1	1.1	2.2	2.8	0.1	2.2	1.4	1
	4	0.9	1.3	0.4	1.1	0.1	2.5	13.3	1
	5	0.9	1.8	1.1	0.7	0.1	2.2	2	1
	6	0.9	5.5	0.5	1.5	0.1	5.1	61.9	1

Table 6.5: *Absolute and relative errors of internal actions on each support for the eleven supports study case.*

	Step	rod 1	rod 2	rod 3	rod 4	rod 5	rod 6	rod 7	rod 8	rod 9	rod 10	rod 11
FEA (kN)	1	18.2	4.6	0.0	−11.2	6.4	14.9	0.9	49.1	20.7	16.9	19.9
	2	16.0	4.9	2.7	−10.9	8.3	18.0	−1.8	50.9	20.1	18.5	15.9
	3	17.5	2.5	0.6	−12.4	7.3	16.6	−1.5	48.8	20.6	18.7	16.2
	4	18.4	4.2	4.2	−12.7	5.3	16.8	1.4	49.9	20.8	18.5	17.9
	5	17.9	5.4	3.9	−10.2	5.1	17.6	0.0	49.9	21.5	20.4	18.2
	6	20.4	6.9	4.1	−12.6	7.6	14.1	2.2	49.3	18.8	19.6	18.5
Err (N)	1	177.4	−172.7	7.1	304.7	−75.2	−14	−7.5	−160.4	−296	−348	−377.3
	2	183	−160.6	13.9	308.5	−92.4	−11.9	−2.5	−179.2	−296.1	−364.4	−382.4
	3	174.3	−171.8	6.5	310.3	−64.1	−9.7	−0.9	−145.2	−292.7	−328.6	−374.5
	4	177.9	−168.9	26.1	301.7	−84.6	−11.7	−14.6	−184.1	−304.3	−363	−383.3
	5	178.3	−160.8	24.1	307.8	−92	−5.6	−13.4	−192.2	−300.6	−368.3	−383.8
	6	188.4	−158.2	40.4	296.3	−97.2	−11.7	−15.6	−191.9	−298.9	−376.6	−393.3
% Err	1	1	3.8	51.4	2.7	1.2	0.1	0.8	0.3	1.4	2.1	1.9
	2	1.1	3.3	0.5	2.8	1.1	0.1	0.1	0.4	1.5	2	2.4
	3	1	6.9	1	2.5	0.9	0.1	0.1	0.3	1.4	1.8	2.3
	4	1	4.1	0.6	2.4	1.6	0.1	1	0.4	1.5	2	2.1
	5	1	3	0.6	3	1.8	0	34.8	0.4	1.4	1.8	2.1
	6	0.9	2.3	1	2.3	1.3	0.1	0.7	0.4	1.6	1.9	2.1

6.2 Performances of the LPM models and possible advantages with respect to FEAs

This section analyses the performances of the LPM with respect to the FEA, highlighting quantitative as well as qualitative advantages of the mathematical model with respect to the more classic FEA approach. The same machine has been used to run both LPM and FEAs using respectively Wolfram Mathematica and Ansys. This ensures that the results are not influenced by different computing capabilities of different machines. The LPM used for the comparison is the general formulation, and in particular applied to the eleven support 3D model already used to assess the accuracy of the developed model.

The solution time is chosen as a quantitative parameter to characterize the performances of the two approaches. The reference value for the solution time of the FEA models has been taken as the result of a structured analysis hereafter explained.

Two different sets of FEAs have been run, the first set with supports modeled with beam elements and the vacuum vessel modeled with shell elements; the second set of FEAs with all components modeled by solid elements (see Table 6.6 for a list of the main elements used in the two sets of simulations). Each set of FEAs has been run at different levels of mesh refinement to reach asymptotic values for the results (position and rotation of the cryogenic device). The number of mesh elements spans from 16000 to 800000 elements for the model with only solid elements and from 4700 to 320000 elements for the model with beams and shells (see Figure 6.6 for an idea of the mesh refinement range).

Looking at Figure 6.7 is clear that both sets of models (continuous and dashed lines), converge to a similar asymptotic value after a certain level of mesh refinement. The use of different element types greatly influences the solution time as can be seen in Figure 6.8. The solution time for the model with beam and shell mesh elements is much lower than that of the fully solid meshed model. Therefore, the performance of the LPM is compared to that of the beam and shell model.

Simulated data for the position and rotation of the cryogenic device, as function of the number of mesh elements, have been fitted with an expression of the form $a/x^b + c$ to find the asymptotic value c (where a and b have no direct physical meaning). This value of c is the estimated real value of the position or rotation of the device. The reference solution time is then calculated as the time that gives a 1% difference of the results from the asymptotic value. The number of elements x_0 of a simulation that provides a result that differs by 1% from the asymptotic value is first calculated thanks to the following equation:

Table 6.6: *Characteristics of element used in the two sets of FEAs according to Ansys nomenclature.*

	Type	Nodes	Order
Full solid	SOLID185	8	Linear
Mixed	SOLID185	8	Linear
	BEAM188	2	Linear
	SHELL181	4	Linear

Table 6.7: *System information and simulation time performances of the FEA and LPM.*

OS Name	Microsoft Windows 10 Pro	
Version	10.0.19045 Build 19045	
System Model	HP Z4 G4 Workstation	
Processor	Intel(R) Xeon(R) W-2155 CPU @ 3.30GHz, 3312 Mhz, 10 Core(s), 20 Logical Processor(s)	
RAM	64.0 GB	
Study case	11 supports	
Program	Ansys 2022 R2 Build 22.2	Wolfram Mathematica 13.0
Elements	11000	
Time	25 s	1.19 s
Cores used	10	10

$$\left| \frac{c - \left(\frac{a}{{x_0}^b} + c \right)}{c} \right| = 0.01 \tag{6.1}$$

The number of mesh elements x_0 needed to reach the 1% difference, calculated with the previous expression, is then used as input in Figure 6.8 to find the associated solution time. The result of fitting process done for each DOF is slightly different and the mean value is taken. The solution time reference for the FEA model is about 25 s. This will be the value used to compare the performances of the LPM to those of the FEA.

Hence, the solution time by means of the developed LPM code shows an improvement of about 20 times from FEAs, which is a great reduction in case of optimization studies where the focus is on choosing the most appropriate support configuration. In such studies, supposing to explore a configuration space of 100000 solutions, even if beam and shell models are used in FEA, the solution time is still around 29 days, which would be greatly reduced if the LPM is used instead (1.45 days).

Although the time cost of a single simulation is in the order of 25 s, which at first glance does not seem to justify the use of the mathematical model, comparison analysis to define the dimensions or material often need additional user-time to configure materials, change dimensions in pre-processing software and extract results in post-processing software. This is not quantifiable but it is reasonable to affirm that the LPM developed offers advantages in pre-processing and post-processing time being these processes easily handled all within the same code. Additionally, the LPM requires only one FEA study to assess the stiffness of the vacuum vessel itself, making it possible to simulate statically one component of the assembly, instead of setting up thermomechanical simulations that require to well define the properties of the multiple interactions between all components which can be sources of errors if properties are not set correctly. Additionally, the developed mathematical model provides a means to cross-check the results of FEA simulations, which can be highly sensitive to incorrectly chosen simulation settings and boundary conditions. This greatly decouples the expertise of the designer or analyst from achieving reliable results for the simulation.

Computational performances and system information are reported in Table 6.7 to facilitate reproducibility of results.

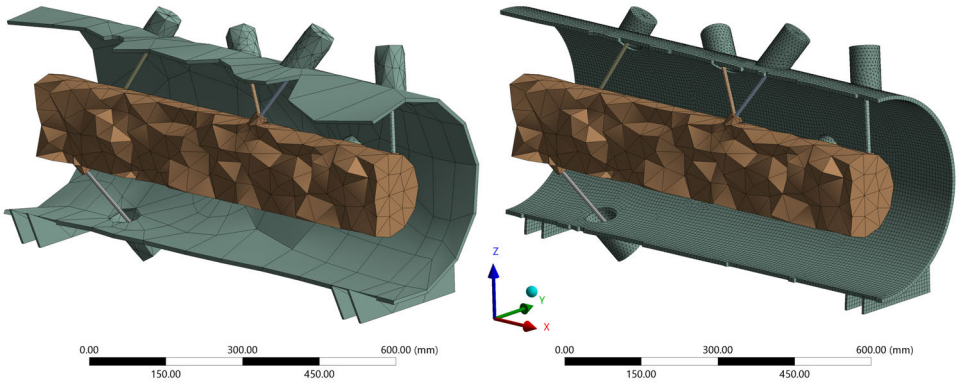

Figure 6.6: *Different models with different mesh refinement levels in evaluating the FEA performances with respect to the LPM.*

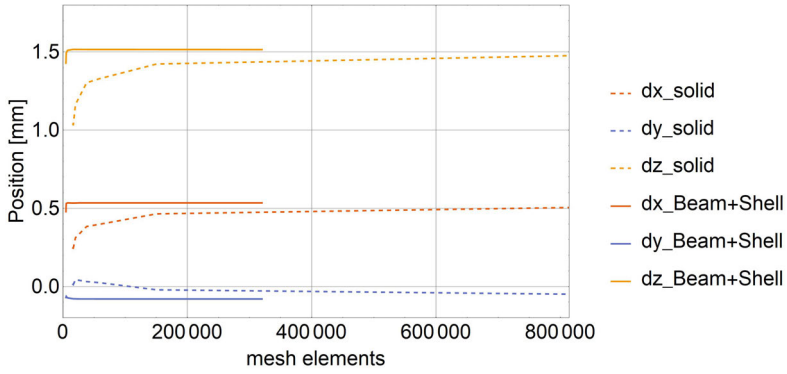

Figure 6.7: *Convergence of results by refining the mesh quality both for the full solid model and for the beam and shell model.*

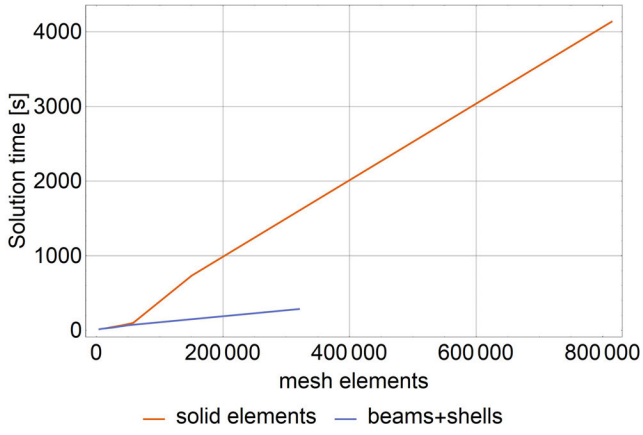

Figure 6.8: *Solutions time refining the mesh quality both for the full solid model and for the beam and shell model.*

Table 6.8: *Error sources considered in the first benchmark (S0), and in the second benchmark (S1).*

	S0	S1
Support deformation - cold-mass weight	YES	-
Support deformation - pre-load	YES	-
Vacuum vessel deformation - cold-mass weight	YES	-
Vacuum vessel deformation - pre-load	YES	-
Vacuum vessel deformation - vacuum	YES	-
Vacuum vessel deformation - own weight	YES	-
Cool-down	YES	-
Backlash	-	YES

6.3 Validation of the LPM for 6S applied to the gantry study case

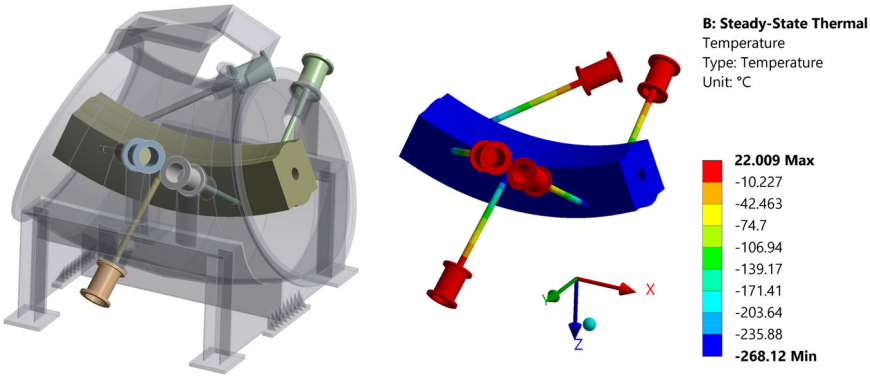

Figure 6.9: *Geometry of the 3D model used in FEAs to benchmark the LPM (left). Temperature distribution on the supporting system (right). Images used courtesy of ANSYS, Inc.*

A series of linear static steady state thermo-mechanical anslysis have been done by mean of the cited FEA software. The simulations consider contributions to the displacement of the cold mass related both to the deformation of supports and deformation of vacuum vessel, as well as the effect of cool down. Each contribution is explicitly reported in Table 6.8. The main parameters used in the simulations are given in the following paragraphs:

- **Geometry**:
  Simulations use the first cold mass of the transfer line for the geometry (number one in Figure 5.1). Six supports support the superconducting dipole inside the vacuum vessel (Figure 6.9). The supports are positioned accordingly to the geometry output from optimization routines discussed in a later stage (Chapter 7). Each support is connected to the vacuum vessel and to the cold mass respectively by a spherical joint and an universal joint. For validation purposes no thermalization has been used to break supports in half.

Table 6.9: *Load imposed at each step for the benchmark simulation ot the 6S LPM.*

Step	Temperature	Preload	Pressure	Acc. X $\mathrm{mm\,s^{-2}}$	Acc. Y $\mathrm{mm\,s^{-2}}$	Acc. Z $\mathrm{mm\,s^{-2}}$
1	Active	Inactive	Inactive	Inactive	Inactive	Inactive
2	Active	Active	Active	Inactive	Inactive	Inactive
3	Active	Active	Active	3754.1	0	−9063.3
4	Active	Active	Active	3468.4	−3754.1	−8373.4
5	Active	Active	Active	2654.6	−6936.7	−6408.7
6	Active	Active	Active	1436.6	−9063.3	−3468.4
7	Active	Active	Active	0	−9810	0
8	Active	Active	Active	−1436.6	−9063.3	3468.4
9	Active	Active	Active	−2654.6	−6936.7	6408.7
10	Active	Active	Active	−3468.4	−3754.1	8373.4
11	Active	Active	Active	−3754.1	0	9063.3

- **Material**:
  Same as in Section 6.1.
- **Interactions**
  Same as in Section 6.1.
- **Loads**
  The first step simulates the behavior of the cold mass during cool-down, cooling the cold mass from 22 °C to −268 °C with no other load active; in a second step a pre-load of 22 kN is applied as remote force acting on the center of gravity of the magnet and with the opposite direction of gravity in the third step. The pre-load is set to 22 kN to ensure that each support remains consistently either in compression or in tension throughout the rotation of the gantry effectively removing backlash. Additionally, in the same step a vacuum pressure (−0.1 MPa) is applied to internal surfaces of the vacuum vessel. Finally, a varying acceleration is applied in steps 3 to 11, as in Table 6.9, to simulate the loads given by gravity during half a rotation of the gantry (180°) by increments of 22.5°. Other loads remain active during these steps.
- **Other**
  The option "large deflection" is turned ON in the analysis settings because large deflections are expected during the cool-down step.

The total displacement of the magnet as a result of the FEA performed is shown in Figure 6.10 for one position of the gantry. Qualitative results are reported in Figure 6.11, a very good correlation between the LPM and FEA has been found. Qualitatively, all pose components evolve consistently in both models during gantry rotation.

To further compare the results with those from the LPM, the magnet's pose must be extracted from the FEA result data. Conclusions about the accuracy of the developed model can only be drawn afterward.

Information about the pose is stored in the matrix ${}^{0}_{1}\mathbf{T}$. Recalling that Equation A.5 allows to transform a vector from one frame to the other:

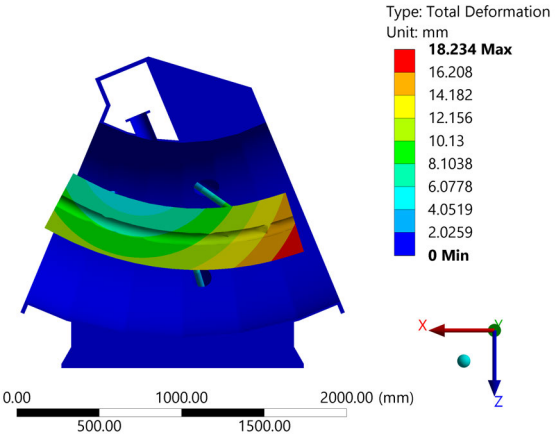

Figure 6.10: *Finite element analysis on the cryostat assembly of dipole 1, total deformation when the gantry is at* 180°. *Images used courtesy of ANSYS, Inc.*

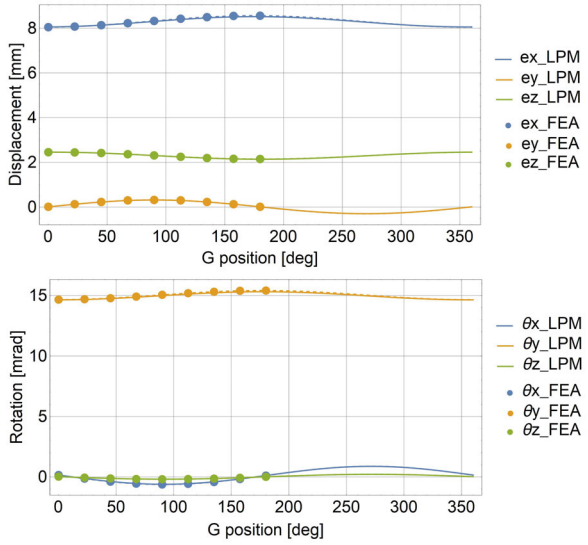

Figure 6.11: *Evolution of the pose* $(e_x, e_y, e_z, \theta_x, \theta_y, \theta_z)$ *during the rotation of the gantry as calculated from LPM (continuous lines) and from FEAs (points and dotted lines).*

$$\begin{bmatrix} {}^0\mathbf{P} \\ 1 \end{bmatrix} = {}^0_1\mathbf{T} \begin{bmatrix} {}^1\mathbf{P} \\ 1 \end{bmatrix} \tag{6.2}$$

${}^1\mathbf{P}$ and ${}^0\mathbf{P}$ represent the position of a point on the rigid body respectively before and after the deformation. This is valid as long as the stiffness of the magnet is much higher that the one of supports and the deformation can be considered as rigid body motion. The following relation is also true and more useful:

$$
\begin{aligned}
{}^{0}\hat{\mathbf{P}} &= \begin{bmatrix} {}^{0}\mathbf{P}_1 & {}^{0}\mathbf{P}_2 & {}^{0}\mathbf{P}_3 & {}^{0}\mathbf{P}_4 \\ 1 & 1 & 1 & 1 \end{bmatrix} = \\
&= {}^{0}_{1}\mathbf{T} \begin{bmatrix} {}^{1}\mathbf{P}_1 & {}^{1}\mathbf{P}_2 & {}^{1}\mathbf{P}_3 & {}^{1}\mathbf{P}_4 \\ 1 & 1 & 1 & 1 \end{bmatrix} = {}^{0}_{1}\mathbf{T}\, {}^{1}\hat{\mathbf{P}}
\end{aligned}
\tag{6.3}
$$

where ${}^{1}\mathbf{P}_1 \dots {}^{1}\mathbf{P}_4$ are the positions of four arbitrary nodes of the mesh in the FEM before the application of the load and ${}^{0}\mathbf{P}_1 \dots {}^{0}\mathbf{P}_4$ are the positions of the same nodes after the load are applied. Both set of data can be extrapolated by the Ansys probe tool. The matrix ${}^{0}_{1}\mathbf{T}$ can be computed as ${}^{0}_{1}\mathbf{T} = {}^{0}\hat{\mathbf{P}}({}^{1}\hat{\mathbf{P}})^{-1}$. The three positional displacements and three rotations are then extracted from the matrix (using Equation A.4).

The pose evolves during the rotation of the gantry following a sinusoidal behavior (Figure 6.11). This is used to fit a sinusoidal function to data and then using parameters of the sinusoidal functions to draw conclusion on the accuracy. The sinusoidal functions can be described by equations of the form $f(\theta_G) = V_{\text{shift}} + A\sin(\theta_G + \theta_0)$ where V_{shift} is the average value of the function during a full rotation of the gantry, A is the amplitude, θ_0 the phase, and θ_G the angular position of the gantry (this definition will be used for axial internal actions). Values of A and V_{shift} are listed in Table 6.10 together with the absolute and relative disagreement between the two models, respectively calculated as $\Delta_V = V_{\text{shift,LPM}} - V_{\text{shift,FEA}}$, $\Delta_A = A_{\text{LPM}} - A_{\text{FEA}}$, $\Delta_V/\text{FEA} = 100\,\Delta_V/V_{\text{shift,FEA}}$ and $\Delta_A/\text{FEA} = 100\,\Delta_A/A_{\text{FEA}}$.

Maximum absolute disagreements, both in terms of V_{shift} and amplitude, are measured for e_x and θ_y. These are also the parameters that show the biggest shift in pose for the magnet during cool-down, 8.3 mm and 15 mrad. As expected, the larger is the absolute value the larger can be the absolute disagreement between the two models. Although the absolute disagreement for these two parameters is the highest, respectively 17 µm and 57 µrad, these values are well below the required accuracy for this application (see Table 3.1) and therefore judged acceptable. Although large relative disagreements for V_{shift} are observed for e_y and θ_x, their absolute values remain smaller than those for e_x and θ_y, which have already been deemed acceptable based on the accuracy requirements. The same comment can be done for the disagreements in terms of amplitudes for e_x and θ_y where high relative disagreements are measured, respectively 9.5% and 11.6%.

Internal actions are also an important outcome of the developed model. These are benchmarked from the same simulation by surveying the forces exchanged in the joints in the FEA model. Results plotted in Figure 6.12 show a good agreement between the models. In terms of V_{shift}, maximum absolute differences are about 250 N over absolutes values of 7.7 kN resulting in maximum relative errors of about 3.6%. In terms of amplitudes, maximum absolute differences are about 150 N over absolutes values of 7.7 kN resulting in maximum relative errors of about 2.7%. The small load difference is deemed absolutely acceptable if compared to a representative load for the application given by the weight of the cold mass ($\simeq$ 15 kN). All supports in the supporting system show similar results, meaning the error may be systematic in the formulation of the LPM or choices for simulation options in FEAs.Various analyses have been conducted to isolate the cause,

Table 6.10: *List of absolute and relative errors on the pose calculated as difference LPM − FEA. Errors are reported as differences between the vertical shifts (V-shift) and amplitudes of the sinusoidal functions (see Figure 6.11).*

DOF	e_x	e_y	e_z		θ_x	θ_y	θ_z	
$V_{\text{shift,LPM}}$	8.29	0.01	2.30	mm	0.13	14.98	0.01	mrad
$V_{\text{shift,FEA}}$	8.30	0.01	2.30	mm	0.13	15.04	0.01	mrad
Δ_V LPM - FEA	17.07	0.29	2.80	µm	4.78	56.96	0.04	µrad
Δ_V/FEA	0.21	2.61	0.12	%	3.68	0.38	0.26	%
Amplitude LPM	0.23	0.31	−0.16	mm	−0.74	−0.33	−0.20	mrad
Amplitude FEA	0.25	0.31	0.15	mm	−0.75	0.38	−0.20	mrad
Δ_A LPM - FEA	−24.14	−3.76	4.22	µm	−11.29	−44.12	−4.25	µrad
Δ_A/FEA	−9.48	−1.22	2.74	%	−1.50	−11.66	−2.10	%

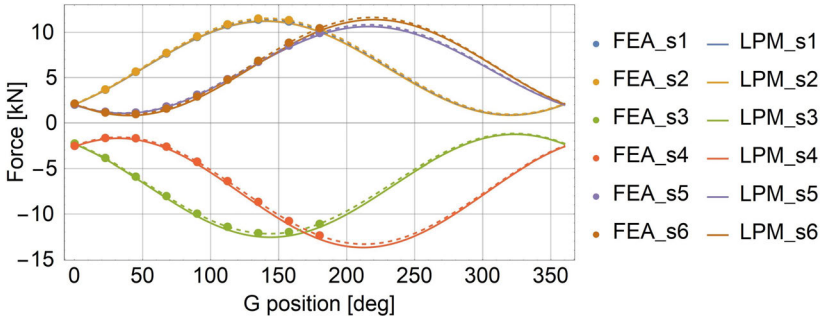

Figure 6.12: *Internal actions on all six supports of solution 6S: LPM results (continuous lines), FEA results (points), FEA fitted curves (dashed lines).*

but none have yielded a conclusive result.

Overall the absolute disagreements are at least one order of magnitude smaller than the accuracy required to the application. Hence the model is proven perfectly suitable for comparative studies, optimization studies, sensitivity studies. For alignment campaigns, without additional experimental testing, the models are considered at least as accurate as FEAs in providing initial values for the alignment.

Additional 13 structural mechanics FEA have been conducted to validate the backlash effect formulated in the 6S LPM. The error sources considered in this analysis, named S0, are limited to the backlash contribution only (as summarized in Table 6.8). All elements in the FEAs are considered as rigid bodies. The backlash causes a jump of the pose of the cold-mass whenever internal actions in supports switch sign as can be seen from Figure 6.13. Between consecutive jumps, the pose remains constant as each joint settles into its newly found equilibrium position. As shown in Figure 6.13, there are 13 such intervals, which motivated the decision to perform FEA simulations for each of them.

FEA using contacts between spherical elements of the rod-ends had been attempted, however results were computationally costly and simulations hard to converge. A faster approach has been proposed by simulating the backlash in the spherical joints by introducing three longitudinal springs (one for each transnational DOF) between the rod end

Table 6.11: *List of absolute and relative errors for the internal actions of 6S solutions. Errors are reported as differences between the means and amplitudes of the sinusoidal functions shown in Figure 6.12.*

Support	1	2	3	4	5	6	
$V_{\text{shift,LPM}}$	6.05	6.05	−6.91	−7.69	5.85	6.11	kN
$V_{\text{shift,FEA}}$	6.16	6.25	−6.67	−7.45	5.97	6.29	kN
Δ_V LPM-FEA	109.12	196.74	238.50	246.70	118.74	177.53	N
Δ_V/FEA	1.77	3.15	3.58	3.31	1.99	2.82	%
Amplitude LPM	5.17	5.20	−5.66	−6.00	4.79	5.29	kN
Amplitude FEA	5.25	5.29	−5.51	−5.88	4.87	5.35	kN
Δ_A LPM-FEA	−85.47	−95.49	149.41	127.71	−81.13	−63.86	N
Δ_A/FEA	−1.63	−1.80	2.71	2.17	−1.67	−1.19	%

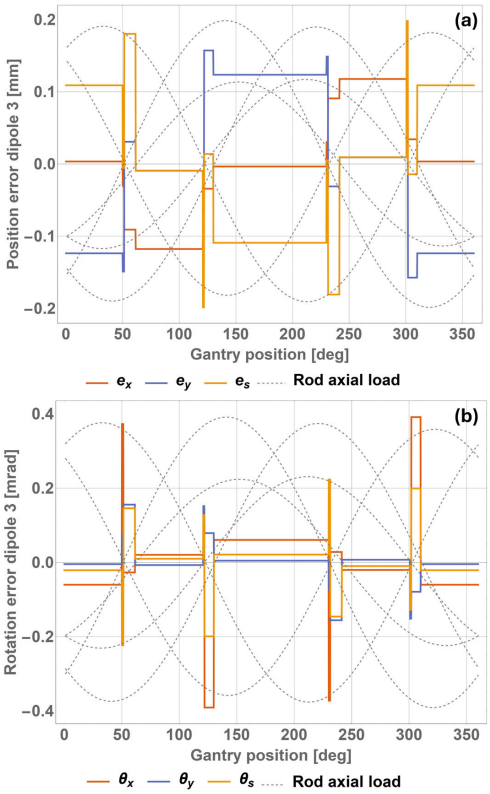

Figure 6.13: *Relation between the discontinuity in the pose and the sign of the axial load on the supports varying the position of the gantry. The axial load in gray dotted lines has been normalized to fit in the plots. (**a**) error on the position and (**b**) error on the rotation of the cold-mass.*

bearing and the rod end body Figure 6.14, excluding the need of introducing contacts in the simulation of joints. The behavior of springs have been modified with an Ansys

APDL command using a COMBIN39 element that allows the description of springs with non linear stiffness. A force-elongation curve has been defined as in Figure 6.15.

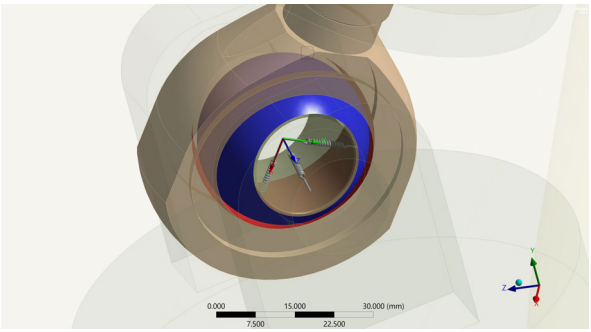

Figure 6.14: *Implementation of 3 non linear springs to simulate the backlash effect on spherical joints. Images used courtesy of ANSYS, Inc.*

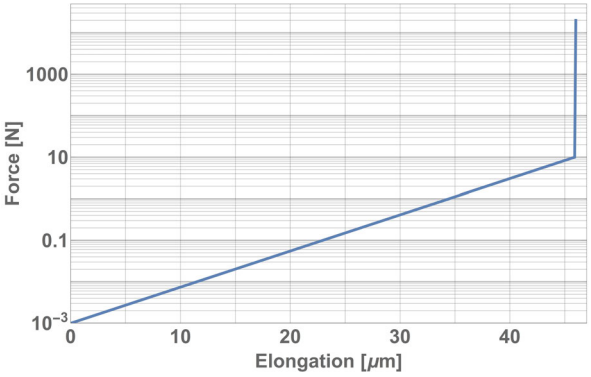

Figure 6.15: *Elongation-Force curve used to define a non linear spring in Ansys APDL.*

The non linear definition of the spring in Figure 6.15 allows to approximate the backlash behavior because even a small force results in an elongation close to $b_c/2 = 46\,\mu\text{m}$ and $b_h/2 = 46\,\mu\text{m}$ (b_c and b_h values are taken from SKF catalogue [103] for steel/bronze rod ends). In contrast, a large force does not produce an elongation greater than those values, 20 kN for the 4th point (Figure 6.15) has been chosen after checking that the forces on supports never exceed this value during the rotation of the gantry.

Results of the FEAs to validate the backlash behaviour are reported in Figure 6.16. Few mismatches between LPM and FEA have been found at around 50° and 230° which are points at which the reaction force on one of the supports happens to be almost zero (see Table 6.12). Thus, just in this interval, the non linear springs elongate less than the value of backlash generating unreliable results from the FEA side. In conclusion, the modification to the DPK described for the LPM are proven effective in estimating the pose of the cold-mass during a rotation of the gantry if joints present backlash.

6.4 Validation of the 8S LPM applied to the gantry study case

Table 6.12: *Force and elongations of axial spring for one of the supports of dipole 1 during the rotation of the gantry. Data from FEA.*

Angle deg	**Force** N	**elongation** µm
25.1	−2369	−46
50.6	−61	−46
51.7	−0.7	−30
87.8	3174	46
124.3	5112	46
127.6	5203	46
180	4183	46
230.6	61	46
231.7	0.7	30
267.8	−3174	−46
304.3	−5112	−46
307.6	−5203	−46
334.8	−5202	−46

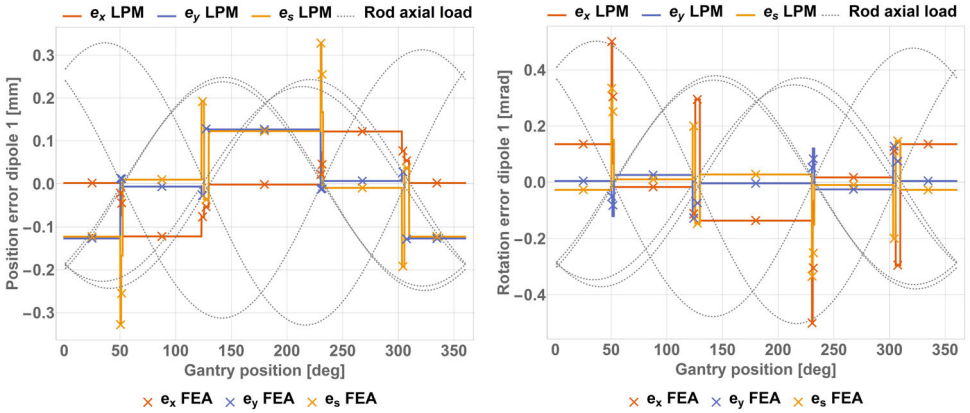

Figure 6.16: *Position and Rotation errors in the MADx frame of reference for the solution S0. Continuous lines show results as calculated from the LPM, points are values obtained by structural FEA.*

The LPM for over constrained supporting systems has been particularized to the study case of the gantry. This benchmark follows the same methodology used in Section 6.3. The materials used, loads applied and boundary conditions of the model are explained in the following paragraphs:

- **Geometry**:
  Eight supports support the superconducting dipole inside the vacuum vessel (Figure 6.17). The supports are positioned in a symmetric way in order to have a self-aligning contraction of the system. Each support is connected to the vacuum vessel and to the cold mass respectively by a spherical joint and an universal joint.

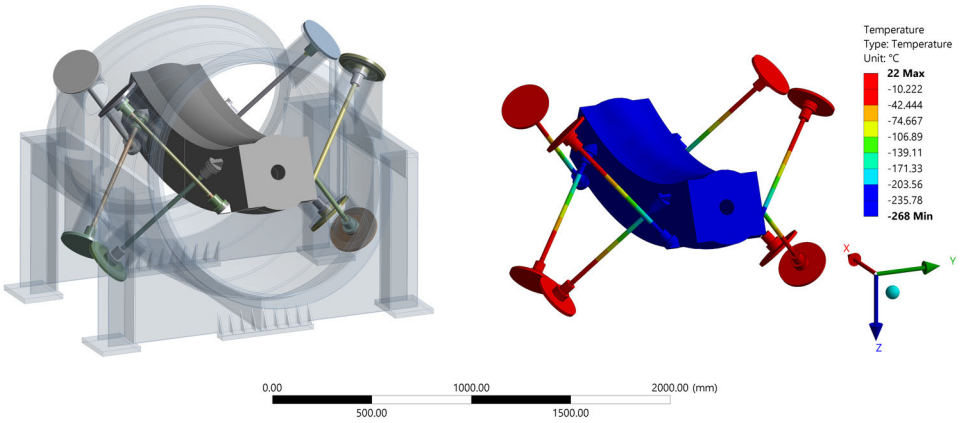

Figure 6.17: *Model used for the validation of the LPM. Distribution of temperature from the steady state thermal analysis. Images used courtesy of ANSYS, Inc*

- **Material**:
  Same as in Section 6.1.
- **Interactions**
  Same as in Section 6.1.
- **Loads**
  Results of steady state thermal analysis have been used as imported loads in a static structural study for FEAs. Pre-load has been applied by defining translation joints and applying joint load as displacement ($\delta = 0.5\,\text{mm}$) corresponding to a load of $35.7\,\text{kN}$ (after having considered the deformation of the vacuum vessel). Acceleration has been added to simulate the rotation of the assembly in the gravitational field. A negative Pressure of $0.1\,\text{MPa}$ has been applied to internal surfaces of the vacuum vessel to simulate the insulation vacuum. A concentrated remote force of components $(5, 2, 0)\text{kN}$ has been applied at position $(-700, 200, -300)\text{mm}$ to simulate an asymmetric response of the system to ensure a more general validation of the model.

Using the methods described in Section 6.3, the pose (position and rotation) of the dipole is calculated from FEA results and then compared to the one calculated with the LPM using Equation (5.39). Results for a series of positions of the gantry are shown in the plot in Figure 6.18, points show the results of FEAs, dotted lines are sinusoidal functions fitted to the FEAs, and continuous lines are the results of the LPM. As done in Section 6.3, the sinusoidal functions are described by equations of the form $f(\theta_G) = V_{\text{shift}} + A\sin(\theta_G + \theta_0)$ where V_{shift} is the average value of the function (force, position or orientation) during a full rotation of the gantry, A is the amplitude, θ_0 the phase, and θ_G the angular position of the gantry. The LPM demonstrates strong qualitative agreement with the FEA, as illustrated in Figure 6.18.

The differences in average position and rotation between the two models, in the worst case, are about $4\,\mu\text{m}$ and $1.6\,\mu\text{rad}$. The relative differences for average position and

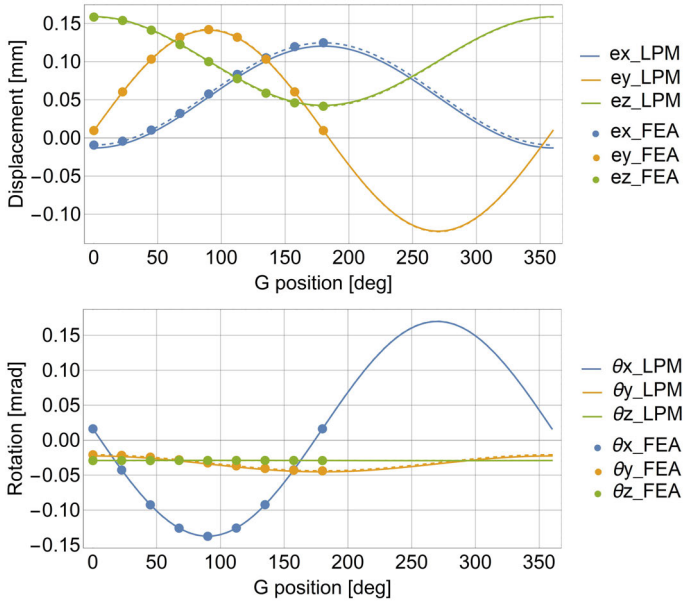

Figure 6.18: *Comparison of the pose (displacement and rotation) of the cold-mass between the LPM (continuous lines) and FEA (points).*

Table 6.13: *List of absolute and relative errors on the pose calculated as difference LPM − FEA. Errors are reported as differences between the vertical shifts (V-shift) and amplitudes of the sinusoidal functions (see Figure 6.18).*

DOF	e_x	e_y	e_z		θ_x	θ_y	θ_z	
$V_{\text{shift,LPM}}$	0.054	0.010	0.101	mm	0.016	−0.034	−0.029087	mrad
$V_{\text{shift,FEA}}$	0.058	0.010	0.100	mm	0.016	−0.032	−0.029085	mrad
Δ_V LPM - FEA	4.065	0.073	0.789	µm	0.036	1.586	0.002143	µrad
Δ_V/FEA	7.045	0.754	0.789	%	0.219	4.904	0.007369	%
Amplitude LPM	0.067	0.132	0.058	mm	0.154	0.011	0.000187	mrad
Amplitude FEA	0.067	0.132	0.058	mm	0.154	0.011	0.000052	mrad
Δ_A LPM - FEA	0.303	0.661	0.318	µm	0.201	0.106	0.135	µrad
Δ_A/FEA	0.452	0.499	0.544	%	0.131	0.928	NR	%

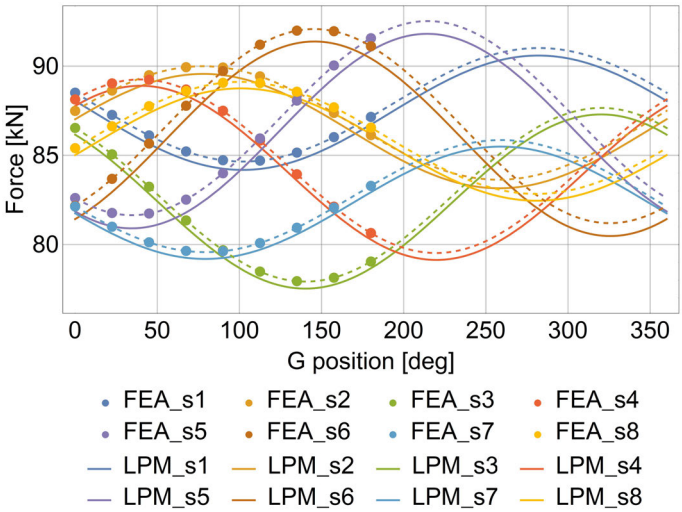

Figure 6.19: *Comparison of the force on each support between the LPM (continuous lines) and FEA (points).*

rotation are respectively 7% and 4.9% of the absolute values calculated by FEAs.

Position and rotation amplitude absolute difference between the two models is respectively 0.66 µm and 0.2 µrad. Relative differences are respectively about 0.54% and 0.93%. As can be seen from Figure 6.18, the absolute amplitude of the rotation around z is almost null. This results in a high relative percentage error when dividing the small absolute difference (0.13 µrad) by an almost null value (0.052 µrad). This high value is non-relevant for the assessment of the accuracy of the LPM.

These values are completely acceptable since the absolute values of 4 µm and 1.5 µrad are much lower than the usual range of accuracy required for these machines (see Table 3.1).

The internal actions on each support have been probed at the joints for the FEA and calculated by Equation 5.35 for the LPM. The plots in Figure 6.19 demonstrate strong agreement between LPM and FEA results. The differences between the two models are reported in Table 6.14, where they are separated in differences of average force $V_{\text{shift,LPM}} - V_{\text{shift,FEA}}$ and differences in the force amplitudes $A_{\text{LPM}} - A_{\text{FEA}}$. The average force differs, in the worst case, by 0.73 kN between LPM and FEA, which is about 0.83% on the average force of 87 kN measured from FEAs. The force amplitudes differ, in the worst case, by 24.6 N or 0.77% in relative terms. These values confirm a good accuracy of the LPM model, with respect to standard simulation methods, to predict forces for an over-constrained architecture. Given their proven accuracy in estimating both pose of the device and the loads on the supports, the developed models are considered applicable to the over-constrained study case.

6.5 Chapter conclusions

Table 6.14: *List of absolute and relative errors on the forces for each support, calculated as difference LPM − FEA. Errors are reported as differences between the means and amplitudes of the sinusoidal functions (see Figure 6.19).*

Support	1	2	3	4	5	6	7	8	
$V_{\text{shift,LPM}}$	87.39	86.36	82.41	84.02	86.36	85.93	82.34	85.61	kN
$V_{\text{shift,FEA}}$	87.83	86.82	82.79	84.39	87.09	86.64	82.71	85.98	kN
Δ_V LPM - FEA	0.45	0.46	0.38	0.37	0.73	0.71	0.37	0.37	kN
Δ_V/FEA	0.51	0.53	0.46	0.44	0.83	0.82	0.45	0.43	%
Amplitude LPM	3.21	3.21	4.88	4.88	5.45	5.45	3.15	3.15	kN
Amplitude FEA	3.18	3.18	4.87	4.87	5.44	5.44	3.14	3.14	kN
Δ_A LPM - FEA	23.35	24.57	14.87	16.63	11.81	12.73	7.38	7.69	N
Δ_A/FEA	0.73	0.77	0.31	0.34	0.22	0.23	0.23	0.24	%

To conclude, the models of an exactly constrained supporting system and an over-constrained supporting system have been validated against Ansys 2022. The results show that the developed models are in good agreement with FEA results. An important achievement in the validation process has been the validation of the generic formulation of the LPM, model that can be used for supporting systems with many supporting rods (≥ 6), arranged in a configuration that may be not necessarily symmetric, and dimensions and material can be different for each rod. These studies estimate an agreement between FEAs and the developed LPM of 99.4% and 98.6% (calculated on simulations of 8 and 11 supports configurations). The developed code based on LPMs outperformed FEAs by around 20 times in computing time as demonstrated in Section 6.2. Additionally, the use of the developed LPM, which are much simpler than FEA in the number of parameters needed to setup a simulation can establish a more insightful overview of the mechanical response of a complex system, allowing designers and analysts to have a clearer grasp on the relationships between the results and the most relevant input quantities. In contrast, FEAs, based on a large number of options and input parameters, require extensive studies to map the relationship between relevant input parameters and output quantities, with a great dependence on the experience of the user and the correct settings of the many options. All above mentioned results makes the developed model interesting also for other cryogenic applications different from the medical application studied in this work, as radio frequency superconducting cavities, optical positioning systems at cold, satellites, superconducting generators or motors.

The models agree with FEA results with an accuracy of 97% and 98.5% for the 6S and 8S gantry solutions respectively. The difference is mainly related to the fact that in 6S the magnet is displaced more during cool-down. This has an impact for example on force equilibrium, internal actions that react to external loads are oriented slightly differently than in the undeformed geometry and LPMs do not update iteratively. Overall even when relative agreement are higher than the average value, absolute agreement are at least one order of magnitude smaller than the required accuracy for the application. Consequently, the models developed are completely adequate for comparative analysis of materials, dimensions etc... Considering the computational advantage the codes can

give, the disagreement of 1.5–3% becomes even less significant if the models are used for optimization routines or sensitivity analysis where a large number of configurations must be checked, as it will be done in this work in following chapters.

7 OPTIMIZATION

Each of the supports of both supporting systems proposed in this thesis (illustrated in Figure 4.5) can be described by five free parameters: three for the position of the cold joint $\mathbf{M_i} = (M_{xi}, M_{yi}, M_{zi})$ and two angles α_1, α_2 that identify the axial direction of the supporting element. The angle α_3 can be defined as the angular position of the support relative to its longitudinal axis. Since the architecture is independent of this angle, it has been omitted. Thus, the two architectures can have up to 30 and 40 independent variables. After the introduction of symmetries for both solutions, considering the self alignment characteristic of the over-constrained solution, the final architectures have respectively 16 (statically determinate) and 6 (statically indeterminate) free parameters. As mentioned in Chapter 4, the aim of the optimization is to find an answer, to the following questions, in the form of the arrangement of supports:

- which is the support arrangement that maximizes the rigidity of the system, not only at one working position of the machine but overall during the complete rotation;
- which is the support arrangement that minimizes the heat-loads by having each support less loaded, requiring less cross-section for the same safety factor;
- which is the support arrangement that enables a full recovery of backlash with the minimum amount of pre-load so that the loads on supports are minimized, minimizing again the heat-loads;
- which is the support arrangement that minimizes the extra-loads during cool-down for the over-constrained solution.

This is an optimization problem that requires the definition of an objective function and depending on its definition the maximization/minimization of the same. The proposed optimization method is the implementation of Genetic Algorithms (GAs) [104] given the large number of free variables and the presence of a large number of constraints, required for example to ensure a sound manufacturing of the cryostat. GAs are biologically inspired algorithms that relies on four keystones: initialization, evaluation, selection and genetic recombination.

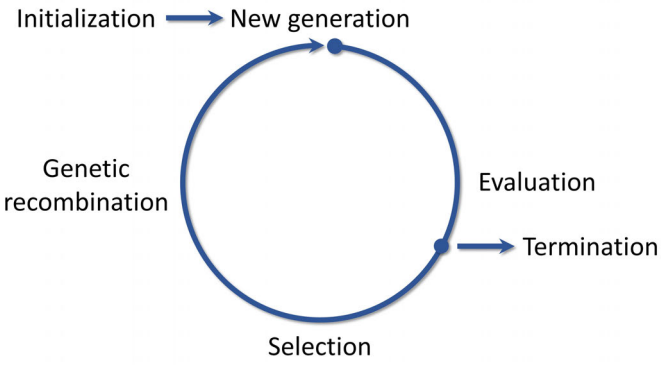

Figure 7.1: *Basic genetic algorithm keystones.*

With reference to Figure 7.1, the algorithm starts usually by randomly initializing a set of individuals, the so called population; the population is evaluated, ranked by what is referred to as a "fitness function" (objective function); individuals are selected accordingly to the evaluation criteria; the population undergoes a genetic recombination that classically is intended as a combination of crossover between individuals and mutation giving a new generation. The algorithm cycles through these steps, except initialization, until a termination condition is met usually after a fixed number of steps. GAs generally converge fast to local optimums. To avoid the algorithm to be stuck in local optimums and to favor the exploration of the solution space the class of GAs used in this work is the so called "island model" [105] which is a class of parallel genetic algorithms. Only the part of LPMs related to displacement of the cold mass due to the deformation of supports is included in the fitness function and therefore in the optimization algorithm, without optimizing the vacuum vessel geometry because its stiffness can be increased without an impact on the heat-loads, and a minor impact on the toal weight of the machine.

7.1 General Boundaries

The geometry defines the individual in the population as the set of six couple of points $(\mathbf{M}_i, \mathbf{H}_i)$ representing respectively cold joints and warm joints. The basic rule that each individual must satisfy is $\|\mathbf{M}_i - \mathbf{H}_i\| = L$ where L is the length of support rods.

Additionally, rules 1-9 listed below must be satisfied by a valid individual, these are based on manufacturing and integration of the supports within the cryostat:

1. two couples of supports are symmetric with respect to the longitudinal symmetry plane of the magnet to simplify the problem and reduce the number of variables,
2. the supports, must not compenetrate the cold-mass volume (in cyan),
3. cold joints $\mathbf{M}_i$ (blue spheres in Figure 7.2) must be placed only on the sides of the magnet at a given distance y_0, this is to simplify the design and assembly within the cryostat,
4. an intermediate point $\mathbf{Ts}_i$ on each support must be contained in the vacuum vessel volume to allow the integration of the thermalization (magenta spheres contained

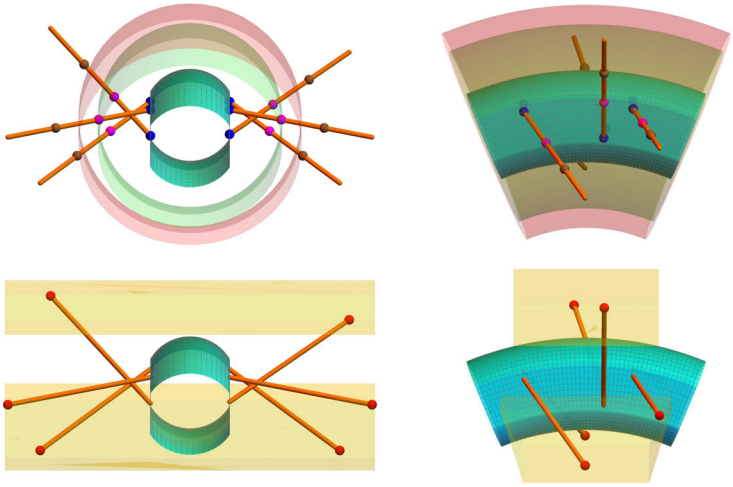

Figure 7.2: *Side and front view of the cold-mass (cyan), supports (orange), cold joints* $\mathbf{M}_i$ *(blue spheres), thermalization interface* $\mathbf{Ts}_i$ *(magenta spheres), reinforcement interface* $\mathbf{A}_i$ *(brown spheres), thermalization valid volume (green) and reinforcement invalid volume (red).*

in the green volume in Figure 7.2),

5. an intermediate point $\mathbf{A}_i$ on each support must be outside the vacuum vessel and at a certain distance from its external surface (brown spheres not contained in the red volume in Figure 7.2), to allow the welding of reinforcements to the assembly interface between the alignment system and the vacuum vessel,
6. the points $\mathbf{A}_i$ on two different symmetric supports must be on the same semi-space of their respective cold joints (they must have the same sign for x),
7. the six supports must be further than a minimum distance from each other, at any point, to avoid compenetrations and to facilitate assembly.
8. supports end (in red in Figure 7.2) must belong to a given volume (in yellow) to allow the manufacturing of interfaces between the vacuum vessel and the gantry, and the strengthening of reinforcement interfaces $\mathbf{A}_i$ onto the vacuum vessel.

7.2 Fitness evaluation and penalty functions

The performance of each individual is quantified defining a scalar value the so called "fitness" of the individual. The fitness for this problem is a figure of merit related to the overall pose error (position and rotation) described in Chapter 5 limited to the deformation of supports.

The pose error $\mathbf{dS} = (e_x, e_y, e_z, \theta_x, \theta_y, \theta_z)$, limited to the deformation of supports, depends on the external forces $\mathbf{F}_s$:

$$\mathbf{dS} \simeq \mathbf{J}\mathbf{D}_q\mathbf{J}^T\mathbf{F}_s = \frac{1}{k}\mathbf{J}\mathbf{J}^T\mathbf{F}_s \tag{7.1}$$

where $\mathbf{D}_q$ is the actuated joint flexibility matrix and if all supports have the same stiffness

it can be simplified as $\mathbf{D}_q = \mathbf{I}/k$.

In the frame of reference of the magnet the external force varies with components that follows a sinusoidal relation with the position θ of the gantry (as shown in Chapter 6). The error for each of the six DOFs can then be described by $e_i = \mu_i + \sigma_i \sin(\theta + \phi_i)$ where μ_i is the mean error, σ_i its amplitude and ϕ_i the phase. The three free parameters can be evaluated for each individual by solving Equation 7.1 for three different gantry positions. The max error during the rotation is then $\tilde{e_i} = |\mu_i| + \sigma_i$. The raw fitness is calculated by:

$$f = \frac{1}{\sqrt{\mathbf{P_e} \cdot \mathbf{P_e}}} \quad \text{with} \quad \mathbf{P_e} = (\tilde{e_1}, \cdots, \tilde{e_6}) \tag{7.2}$$

Hence, a larger value of f characterizes an individual that shows overall less pose error than another.

The addition of pre-load requires to evaluate not only the pose performance but also the evolution of axial reaction in the supports. To avoid backlash, each axial reaction must be either always positive or negative for a given value of pre-load. In this model this condition has been obtained by scaling the fitness f by penalty functions. p_1 is the penalty applied to the raw fitness to decrease the final value whenever an individual does not show forces on supports that are either always positive or negative for the given pre-load:

$$p_1 = \begin{cases} 1 & \text{if} \quad \text{Min}(\beta_i) > 0 \\ \text{Exp}\left(-\frac{1}{2}\left(\frac{\text{Min}(\beta_i)}{\sigma_b}\right)^2\right) & \text{if} \quad \text{Min}(\beta_i) \leq 0 \end{cases} \quad \text{with} \quad p_1 \in (0, 1] \tag{7.3}$$

where, $\sigma_b = 0.05$ and $\beta_i = 1 - \sigma_{q,i}/|\mu_{q,i}|$, with $\sigma_{q,i}$ and $\mu_{q,i}$ are respectively amplitude and mean value of F_{qi}, the i-th axial reaction force on supports $F_{qi} = \mu_{q,i} + \sigma_{q,i} \sin(\theta + \phi_{q,i})$. An illustration of the loads on supports for a non ideal support configuration and an ideal support configuration are given in Figure 7.3. The non ideal configuration has two supports clearly switching sign from compression to tension and back to compression during the rotation of the gantry. Indeed, $\text{Min}(\beta_i) = -3$ and $p_1 < 1$ meaning that this configuration will get penalized by the algorithm. The ideal configuration is not penalyzed since it has supports loaded either always in tension or compression, thus $\text{Min}(\beta_i) > 0$ and $p_1 = 1$.

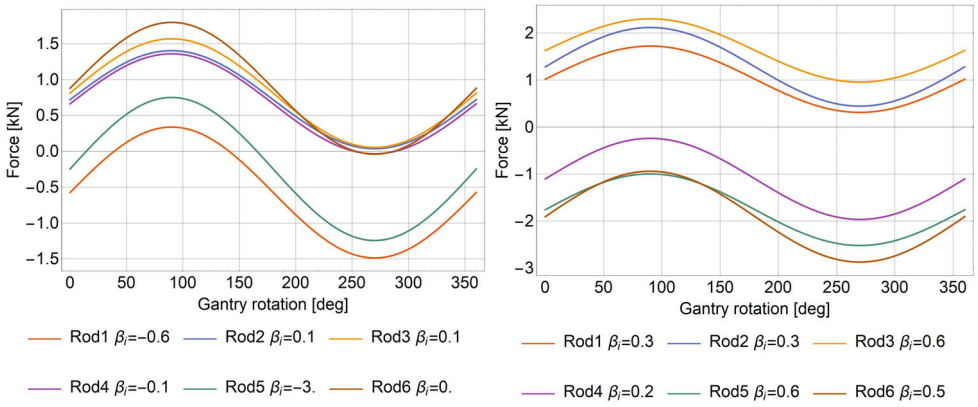

Figure 7.3: *Example of possible load conditions of the supports for two different support arrangements.*

A second penalty p_2 is applied if the amplitude of forces is bigger than a given value:

$$p_2 = \begin{cases} 1 & \text{if} \quad \gamma < \mu_a \\ \text{Exp}\left(-\frac{1}{2}\left(\frac{\gamma - \mu_a}{\sigma_a}\right)^2\right) & \text{if} \quad \gamma \geq \mu_a \end{cases} \tag{7.4}$$

with $\gamma = \text{Max}(|\mu_{q,i}| + \sigma_{q,i})$, $\mu_a = 18\,\text{kN}$ and $\sigma_a = 1.5\,\text{kN}$. These values are selected to minimize the loads on the supports, ensuring a uniform distribution of the cold mass weight and the pre-load across all supports. The penalty based on force amplitude is related to the minimization of heatloads. To satisfy the condition of a minimum given safety factor, higher amplitude forces would require a larger cross-section of the supports thus conducting more heat. Applying the mentioned penalty functions to Equation 7.2, the final fitness function is:

$$\tilde{f} = f p_1 p_2 \tag{7.5}$$

7.3 Genetic recombination: mutations

Mutation is a process that disturbs an individual helping to cover the search space to find solutions. Mutation is based on random changes, the strength of the disturbance is known as “step size”. Mutations helps to make the algorithm converge to optimums, a common way to do it is to have a degree of freedom to adjust the step size. Usually, and also in this work, the step size is reduced when refining the search for the local optimum, a process called “exploitation”. While the step size is bigger in the so called “exploration”, when other local optimums are sought in the attempt to find the global optimum. The step size can be linked to the fitness value of the individual so that most fit individuals are used for exploitation while others serve for exploration.

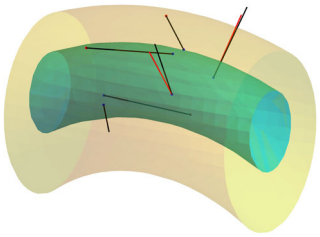

(a) *Rotation mutation of symmetric supports.*

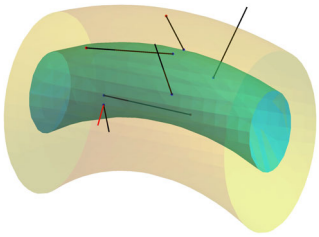

(b) *Rotation mutation of non-symmetric support.*

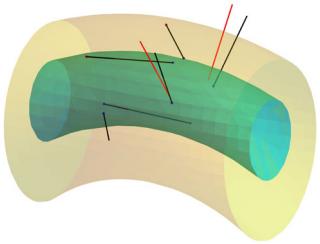

(c) *Roto-translation mutation of symmetric supports.*

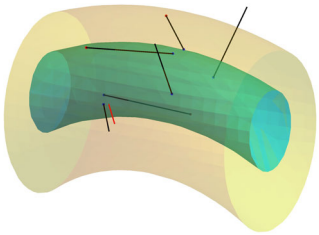

(d) *Roto-translation mutation of non-symmetric support.*

Figure 7.4: *Example of the mutation operators applied to an individual where the mutated supports are highlighted in red.* ***a*** *and* ***b*** *show a rotation only mutation of a symmetric and non-symmetric support respectively.* ***c*** *and* ***d*** *show a roto-translation mutation.*

For the study case of cold-warm supports the most classic bit-flipping mutation cannot be applied as it can generate an individual that does not satisfy the constraints necessary to make an individual mechanically functional. The mutation operators defined must work synergically with constrains. Therefore, it has been chosen to define the two following operators:

- The rotation operator (Figure 7.4a and Figure 7.4b) adjusts the position of the warm joint of one of the supports while keeping its corresponding cold joint fixed. Additionally, this operator ensures that the mutated individual complies with rules 1 to 8.
- The roto-translation operator (Figure 7.4c and Figure 7.4d) generates a new cold joint on the magnet, followed by the calculation of a new warm joint. This operator applies both translation and rotation, ensuring compliance with rules 1 to 8 during the second rotational step.

Both mutations occurs randomly on one of the six supports, paying attention when the support is symmetric replacing also the mirrored one as illustrated in Figure 7.4. The choice to apply one or the other operator is based on a random choice for each individual

of the population. Another common mutation operator is "crossover", this has not been used in this code because in the island model chosen there is no communication between the islands and the reproduction chosen follows a mitosis type, by copying the elite of the island and then applying mutations to the copies.

7.4 Overall GA algorithm

The overall developed routine is illustrated in Figure 7.5.

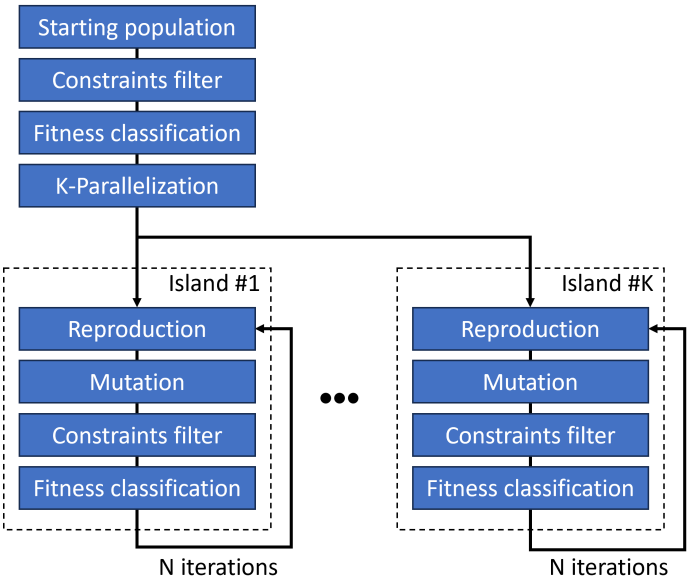

Figure 7.5: *Flowchart of the Genetic algorithm used in this thesis.*

The steps are here summarized:

1. A starting population of n individuals gets randomly generated respecting the basic rule $\|\mathbf{M}_i - \mathbf{H}_i\| = L$;
2. constrains are applied to the population to filter for valid individuals that respect rules 1-9 stated in Section 7.1;
3. the fitness of the individuals of the starting population is evaluated and individuals are classified accordingly;
4. the first k individuals of the starting population become the first generation elites and are separated into k islands;
5. the population of the island reproduces by mitosis, copying the support arrangement of the elite;
6. the population of the island is subject to random mutations;
7. constrains are applied to the population of the island to filter for valid individuals that respect rules 1-9 stated in Section 7.1;
8. the fitness of the individuals of the starting population is evaluated and individuals are classified accordingly.

Additional rules are imposed to the algorithm:

- Steps 5-8 for each island happen in parallel;
- the most fit individual of an island is added to the next iteration of the same island to eliminate the random deterioration of the overall fitness of the island, preventing it from drifting away from the local maximum;
- no cross-island interaction is programmed, no new islands are generated. Both measures are put in place to avoid genetic diversity loss;
- at the end of each iteration the fitness of all islands is compared between them to tune hyper-parameters: an island with low maximum fitness gets mutated more intensely and with a larger number of individuals. This promotes exploration of the solution space. In contrast high max fitness islands are used for exploitation being mutated less.

The convergence of the algorithm is shown in Figure 7.6 for 10 runs of the code for the same group of magnets initializing each time a different random population and running the code for 300 iterations.

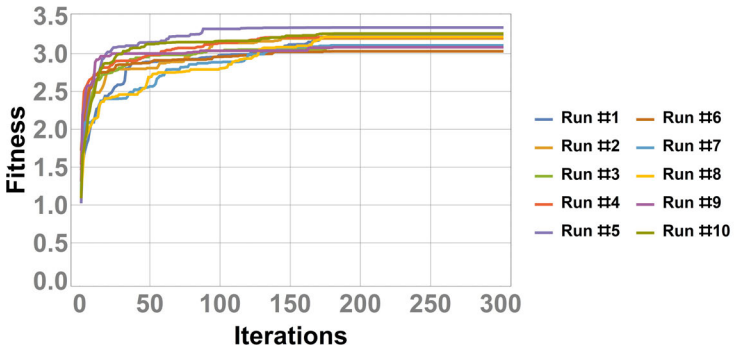

Figure 7.6: *Convergence plot of the best fit value during successive iterations.*

The advantage of having implemented the "island model" parallel algorithm is illustrated in Figure 7.7. The evolution line of island 13 (in green in the figure) shows that before the 100th iteration the solution could get discarded in a non parallelized genetic algorithm, because already at iteration 50 almost all other solutions perform better. After 100 iterations island 13 dominates on all other islands. The parallel algorithm offers an improved method for preventing the issue of becoming completely trapped at a sub-optimal level of performance by ensuring that temporarily non optimal solution can explore or exploit the solution space, retaining genetic diversity. Otherwise, if only one island exists, this would be quickly dominated by the first elite, with the set of rules defined in this algorithm.

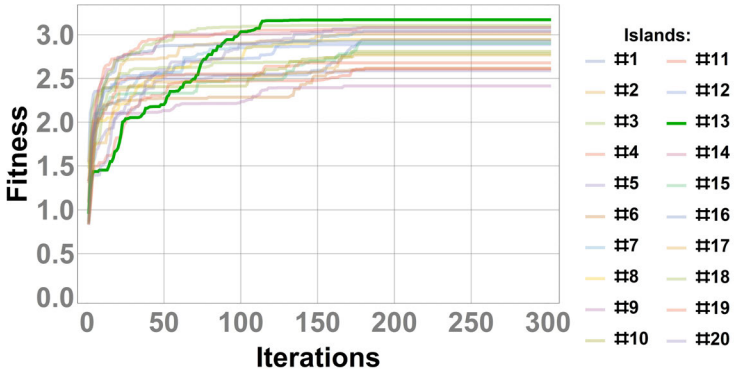

Figure 7.7: *Best fit values of each island for a single run of the algorithm.*

8 DESIGN OF THE SUPPORTING SYSTEMS: THE GANTRY CASE STUDY

This chapter reports the final design choices done for each supporting system (6S and 8S). First, the advantages of the proposed optimization strategy of the arrangement of supports is presented. This is done consistently for both solutions following the routine discussed in Chapter 7 but shown only for solution 6S. Secondly the LPMs are used to perform a comparison analysis of different materials and cross-section dimensions of supports in order to identify the combination that minimizes heat-loads while having enough stiffness to satisfy accuracy requirements for the supporting system. Additional design choices such as the use of the pre-load backlash removal system and the design of the alignment system are discussed.

8.1 6S Optimization results

Two comparison analysis have been done, the first aiming at demonstrating the effectiveness of the optimization routine and the second one aiming at demonstrating the advantages of having a backlash recovery system trading it with higher loads on supports. In the first comparative analysis solution S1 is compared with solution S2:

- S1 being the beam line where the supporting systems of the four superconducting dipoles are those originally designed without the use of computer aided optimization,
- S2 being the beam line where the supporting systems of the four superconducting dipoles are those designed with the proposed computer aided optimization.

In the second analysis, solution S3 is compared with solution S4:

- S3 being the beam line where the supporting systems of the four superconducting dipoles are subject to backlash and no pre-load system is used,
- S4 being the beam line where the pre-load system has been implemented in supporting systems of the four superconducting dipoles.

Since initial support configuration S1 did not consider restrictions adopted in the latest stage of the study (rules 3, 5, 6, 7, 9 in Chapter 7), the influence of a much advanced vacuum vessel design has not been included in this comparison. Table 8.1 lists the error sources considered in the comparison analysis presented.

Table 8.2 shows the efficacy of the optimization algorithm described in Chapter 7 using the models developed in Chapter 5 and validated in Chapter 6 Values in Table 8.2 for $e_x, \ldots, \theta_z$ are the maximum measured during a complete revolution and over the four cold masses. The pose accuracy has been improved by average of 16% between S1 and S2, the major and most improvement is seen for θ_x, improving by 83% reaching an acceptable value of 10 mrad. This has been also a crucial improvement since the maximum value of 0.6 mrad for θ_x in S1 was already at the limit of requirements (Table 3.1). This leaves

Table 8.1: *Error sources considered for the initial design with pre-load (S1), the optimized system with pre-load and without other elastic components (S2), the optimized system with backlash and elastic components (S3) and the optimized system with pre-load (S4).*

	S1	**S2**	**S3**	**S4**
Support deformation - cold-mass weight	YES	YES	YES	YES
Support deformation - pre-load	YES	YES	-	YES
Vacuum vessel deformation - cold-mass weight	-	-	YES	YES
Vacuum vessel deformation - pre-load	-	-	-	YES
Vacuum vessel deformation - vacuum	-	-	YES	YES
Vacuum vessel deformation - own weight	-	-	YES	YES
Backlash	-	-	YES	-

margin for the additional displacements related to the deformation of the vacuum vessel that are not considered in the comparison between S1 and S2. Also e_y sees a significant improvement of 45% passing from 0.27 mm to 0.15 mm. The deterioration of 87% for e_x although high is acceptable considering that beams are less sensible to errors introduced along the longitudinal axis. Additionally, the spike of e_x can be seen only localized to the 4th dipole looking to the full plots of the pose during rotation Figure 8.1 (all other plots for this analysis are reported in Appendix D). On the bottom of the plots is represented with rectangles the transfer line: in gray warm elements, not considered in this study; in red superconducting quadrupoles and in blue superconducting dipoles. The horizontal axis shows the number associated to the transfer line element. The vertical axis shows values of the position or rotation error. The colors of the curves show the errors with respect to a specific position of the gantry. This plotting convention is used through the rest of the thesis. The 4th dipole is the hardest to optimize due to the combination of gravity being directed almost as the longitudinal direction x and the choices of design of the vacuum vessels. Indeed supports can be placed only to the sides of the cold mass, which offer less reaction to a load that is almost longitudinal. As mentioned the initially designed supporting systems for S1 did not consider an advanced design of the vacuum vessel.

Values of the raw fitness $\mathbf{f}$ (Equation 7.2) for S1 and S2 reflect the improvement cited above. The fitness corrected with penalty functions $\tilde{\mathbf{f}}$ highlights a much higher overall improvement, not only for the pose accuracy but also in terms of thermal insulation capabilities. This is due to the decrease of the required pre-load, $1.32mg$ instead of the initial $2.75mg$. This is a significant result of the optimization routine written, as the fitness function $\tilde{\mathbf{f}}$ requires an optimal solution to have low axial loads on supports, being possible only by re-arranging the supports such that only a minimal pre-load is needed to recover backlash. This lowered consequently the reaction load on each support by 44%, lowering the required cross-section to achieve the same safety factor. Hence a proportional reduction by 44% of the conductive heat-load to the cold-mass has been achieved. Although a difference of 0.55 W per dipole may seem small in common mechanical applications, the power required to extract this heat at 4.7 K using cryocoolers (with the SHI RDK-415D2 4K as an example) is around 2.6 kW, leading to a reduction of approximately 2.2 kW in

Table 8.2: *Absolute errors and percentile improvement for each DOF for an initial support configuration and the optimized one.*

DOF	Initial (S1)	Optimized (S2)		Improvement
$\mathbf{e_x}$	0.18	0.34	mm	−87%
$\mathbf{e_y}$	0.27	0.15	mm	45%
$\mathbf{e_z}$	0.20	0.19	mm	3%
$\theta_\mathbf{x}$	0.60	0.10	mrad	83%
$\theta_\mathbf{y}$	0.10	0.05	mrad	55%
$\theta_\mathbf{z}$	0.07	0.07	mrad	−1%
$\mathbf{f}$	(3.1, 1.6, 2.0, 2.0)	(4.3, 5.2, 4.8, 2.7)		
$\tilde{\mathbf{f}}$	$(\approx 0, \approx 0, \approx 0, \approx 0)$	(4.3, 5.2, 4.8, 1.2)		
$\mathbf{F_{q,max}}$	35.5	19.8	kN	44%
bulk diameter	24	18	mm	
safety factor	12	12.2		
heat-load @ 4.7 K	1	0.55	W	44%
compressor input power	4.8	2.6	kW	44%

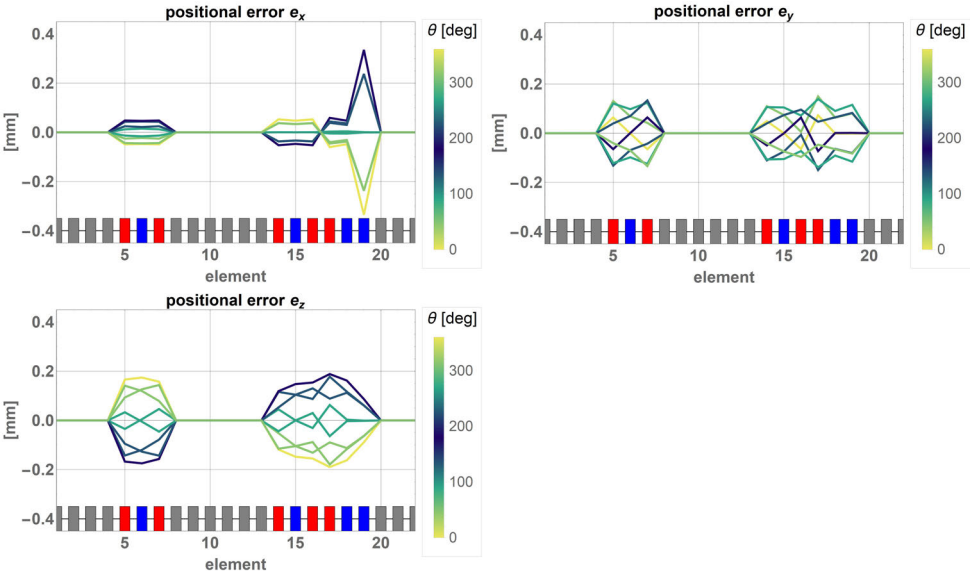

Figure 8.1: *Displacement of the elements of the gantry beam line during rotation with supporting systems of the 4 dipoles as result of the optimization.*

the required power.

The optimization routine proposed in this work demonstrates useful also to extrapolate conclusions on basic design choices. For example, the 6S solution has been formulated with a symmetry only of 4 out of the 6 supports with respect to xz plane (that can be seen from Figure 8.2) while the two remaining supports could have been placed randomly by the random population generator. After running the algorithm for 10 times (each time with a different initial population) results seem to converge in moving the two non-

symmetric supports in a symmetric manner as illustrated in Figure 8.3. The algorithm can help designers to introduce the symmetry also on the remaining supports. In the specific case of the gantry, this can be linked to the symmetry conditions of the application: the external load on the supported element is identical whether the gantry is at position $-\theta$ or at position θ relative to the vertical position.

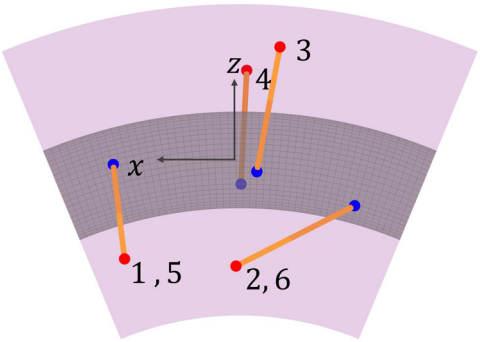

Figure 8.2: *Symmetric supports in solution 6S. The two couples of symmetric supports on the left and right are seen as one because the image is projected on their symmetry plane. The two supports in the middle are not symmetric.*

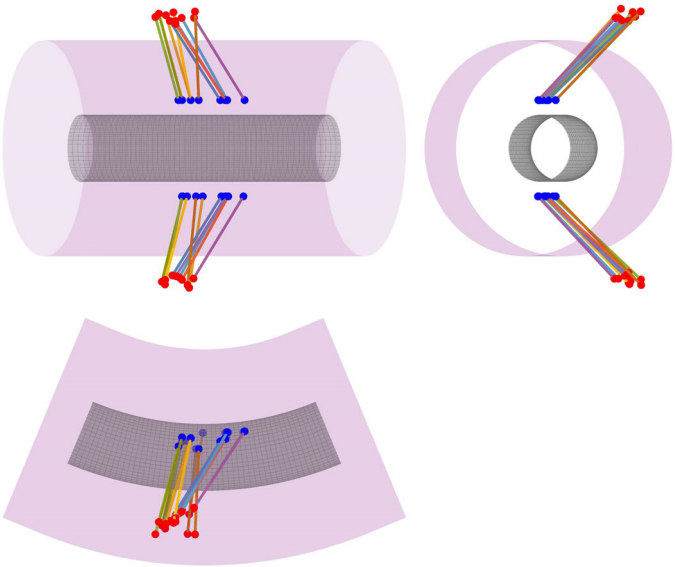

Figure 8.3: *Position of the initially non-symmetric supports after 10 runs of the genetic algorithm. Only the supports left initially unconstrained by symmetry are shown.*

8.2 6S Backlash and pre-load system

This section discusses the second comparison analysis for solution 6S, where solution S3, which accepts backlash in the joints, is compared with solution S4, which compensates for backlash through pre-load and higher loads. The impact of backlash in the joints have been considered by using realistic data from manufacturer of standard components such as rod ends. The radial internal clearances in cold and warm joints respectively, $b_c = 92\,\mu m$ and $b_h = 92\,\mu m$ (see SKF catalogue for steel/bronze rod ends [103]), have been introduced in the error model as explained in the Section 5.1. Results related to the influence of backlash only are reported in Figure 8.4 taking as example the third dipole of the line Figure 4.2. This influence is very discontinuous in relation to the gantry position. The discontinuity is expected since each joint has been modeled to be in two possible positions depending on the force. Indeed, whenever there is a change in the sign of the load on any of the supports (dashed lines crossing the horizontal axis) there is a corresponding jump in all the six DOF of the cold-mass.

The backlash introduces an error on the pose which is not sinusoidal as found from the LPM. however the error is still periodic with respect to the rotation of the gantry, hence after 360° the misalignment is the same of the one at the starting position, with the exception of positions where the axial load on one of the supports is exactly zero. In this case the value could be different due to the discontinuity and it is related to the load history, which is the clockwise or counterclockwise rotation of the machine. Having a supporting system with backlash has a few disadvantages:

- at net of other load contributions, the pose is constant in between one pose discontinuity and the other. This interval can be broader or tighter, depending on the arrangement of the rods. For example around 50° the interval between two discontinuities is extremely tight (Figure 8.4). In such cases, due to the uncertainty in the position of the gantry, the elements of the transfer line may be in a non reproducible position and the machine may not operate as expected;
- the jump in the cold-mass position from one side to the other of the discontinuity can results in shock impacts in the joints, with the risk of premature failures of bearing components;
- friction has not been considered in this study. its presence can result in a stick-slip behavior in the joints which could aggravate the uncertainty of the position of the cold-mass around discontinuity points;
- the absolute values of pose errors due to backlash alone are comparable to the combined deformations of the vacuum vessel and its supports. Therefore, efforts should be made to minimize backlash to avoid the need for oversizing other components to meet accuracy requirements.

In conclusion, two solutions can be taken respectively to mitigate or eliminate completely the backlash issues:

1. a geometric optimization of the architecture: a new fitness function can be introduced in the optimization routine highly based on the influence of backlash in order to reduce its effects.

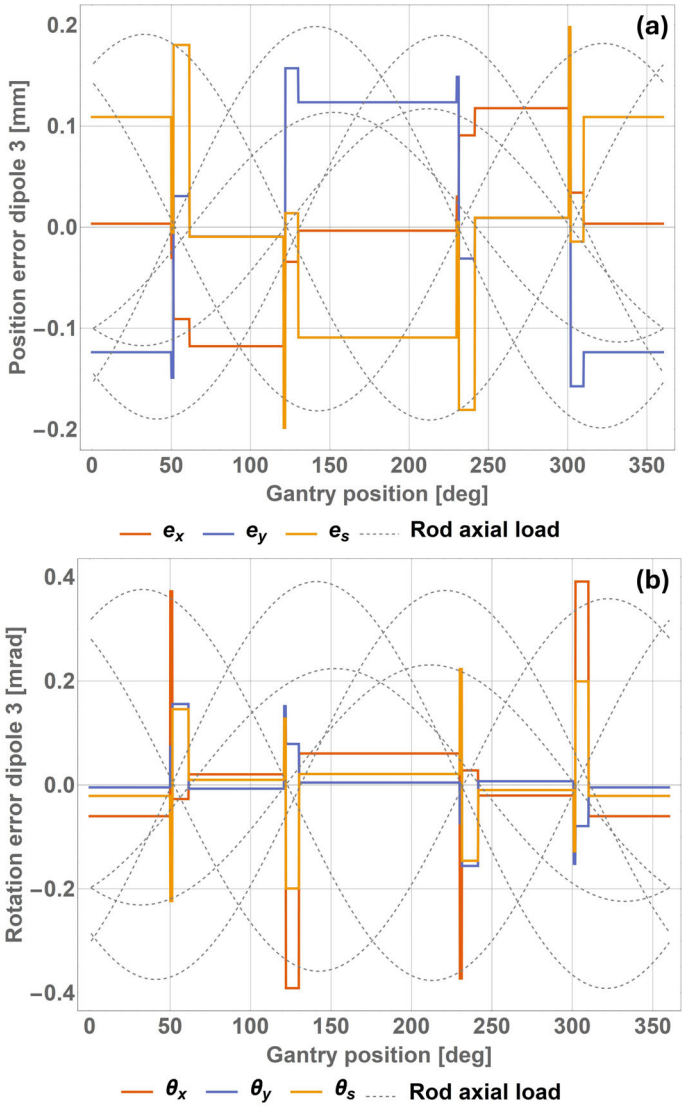

Figure 8.4: *Relation between the discontinuity in the pose and the sign of the axial load on the supports varying the position of the gantry. The axial load in gray dotted lines has been normalized to fit in the plots. (**a**) error on the position and (**b**) error on the rotation of the cold-mass.*

2. the addition of a pre-load system: the pre-load can shift the axial reactions in the supports so that the same support is either always under tension or under compression (Figure 8.5), therefore the joints are always in the same position during the rotation of the gantry. The recovery of backlash with a tension system will put under higher stress the supports of the cold-mass and the vacuum vessel. The increase of pose error due to the pre-load may be less than the pose error given by

backlash, making this a highly advantageous solution. The arrangement of supports can be optimized by requiring that the minimum pre-load is needed to eliminate backlash.

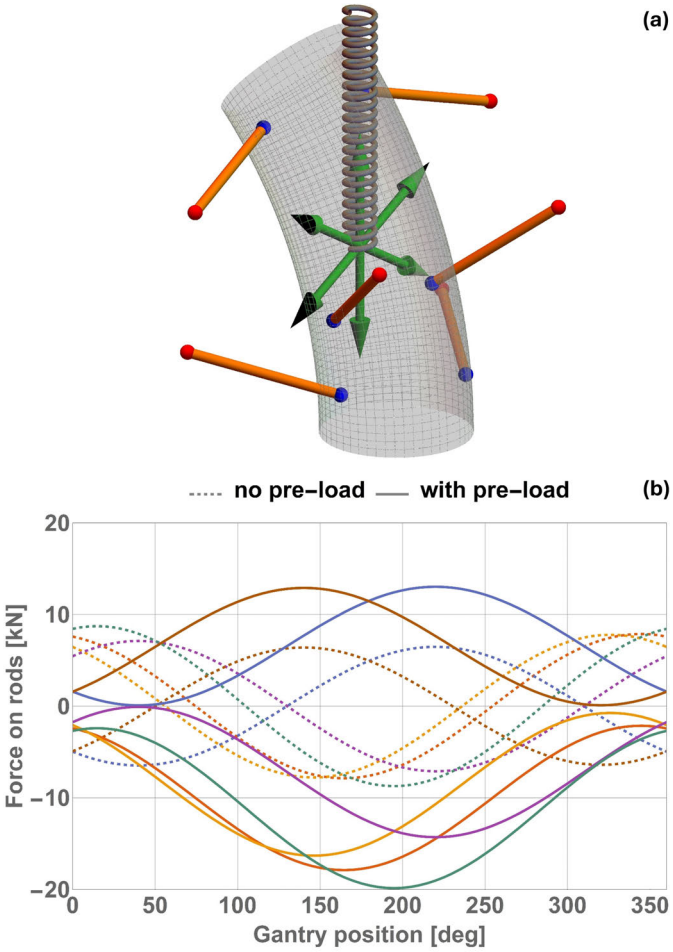

Figure 8.5: *(**a**) conceptual scheme of the pre-load represented by the red arrow and gravity load in green during the rotation of the gantry. (**b**) Effect of pre-load on rods internal actions in relation to the gantry position.*

The concept of the pre-load system is illustrated in Figure 8.5. A constant force is applied in a given direction (gray spring) aligned with the variable load at a given time (gravity in the case of the gantry). While the gantry rotates, the gravity load (green arrow) belongs to a plane with respect to the cold-mass and varies direction. The pre-load has been applied so that it belong to such plane. The idea, based on common sense, is that for some positions the pre-load overcomes the pull of gravity. In this way, the cumulative force has always a positive component in the direction of the pre-load. As confirmed in Figure 8.5, applying a pre-load is sufficient to have the supporting rods

either under tension or compression only. The minimum value of applied pre-load to reach this condition is $1.32mg$, this is true with almost no margin on the sign flip for the reactions on supports. With g the gravity and m the mass of the supported body, 1.32 is a value that resulted from the optimization of the geometric configuration of the supporting system. The pre-load of $1.32mg \simeq 23\,\text{kN}$ can be handled by commercial 6 bar pneumatic cylinders still with a margin of 7 kN. The use of pneumatic actuators is convenient due to the low stiffness of compressed air, so that small misalignments in the cold-mass do not produce excess forces with respect to the target pre-load. The backlash recovery systems has been proven effective, in this case the joints always stay in the same equilibrium position regardless of the gantry angular position reducing the error on the alignment of magnets and therefore increasing the beam performances.

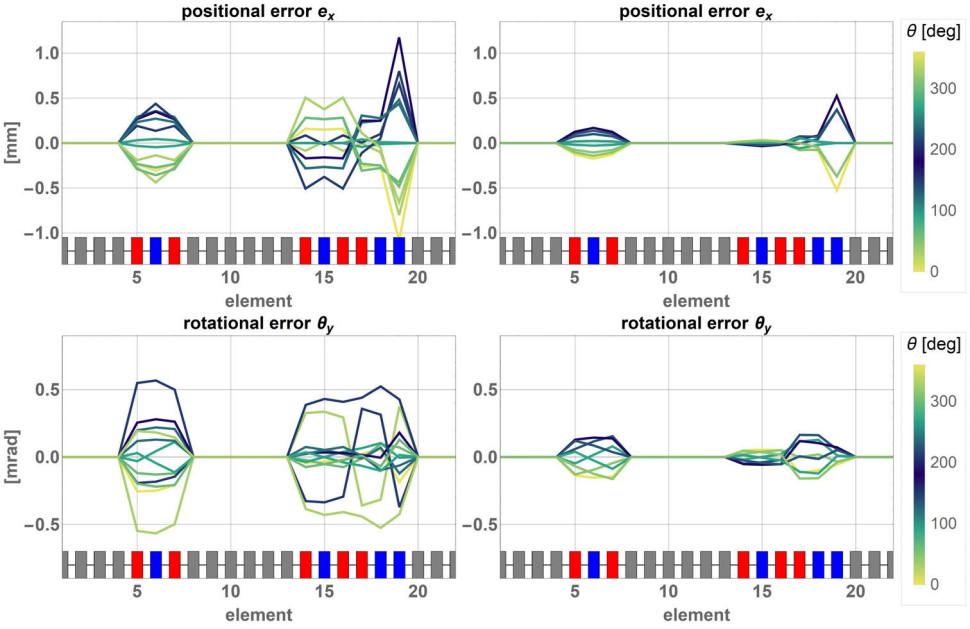

Figure 8.6: *(**a**) - (**c**), show results of position and rotation error due to backlash, elasticity of supports and elasticity of vacuum vessel, considering both gravity and vacuum differential pressure (S3). (**b**) - (**d**), show results of position and rotation error in the backlash recovery solution. Where, backlash effects are eliminated by a pre-load, all previous contributions to the error have been considered (S4). Angular color scale (yellow to blue) applies to all graphs.*

Figure 8.6 shows the comparison of the error in a supporting system with backlash (S3 in **a** and **b**) and in a system with the backlash recovery system applying a pre-load (S4 in **c** and **d**). These are plots of the two DOF where the biggest improvement has been achieved (All other plots available in Appendix D). The results have been calculated with the Lumped Parameter Model described in Chapter 5, considering the error contributions reported in Table 8.1. As can be seen from Table 8.3, five DOFs have been improved by $46 - 71\%$ while the error on θ_x shows only a little decrease in accuracy. The same safety factor $N_3/A_3 = N_4/A_4$ has been used in solution S3 and S4 in order to have a

fair comparison (N_3 the maximum load in solution S3, A_3 the cross section of supports in solution S3). The two-fold increase of the load on supports $N_4 = 2N_3$ from S3 to S4 translates in about a two-fold increase of the conduction heat-load to the cold-mass (proportional to A). The conduction heat load goes from about 0.25 W to 0.55 W to 4.7 K, cumulative for all six supports. Thanks to the pre-load system and the geometry optimized accordingly, the variations in pose during the rotation are now within the requirements, at the cost of an increase of 120% of heat loads, which are still within the limits (1 W at 4.7 K for each cryomodule).

Table 8.3: *Absolute errors and percentile improvement for each DOF for a supporting system with backlash and with a pre-load backlash recovery system. Positive percentile values are related to improvements.*

DOF	With backlash (S3)	With pre-load (S4)		Improvement
$\mathbf{e_x}$	1.18	0.52	mm	55%
$\mathbf{e_y}$	0.67	0.33	mm	52%
$\mathbf{e_z}$	0.93	0.39	mm	59%
$\theta_\mathbf{x}$	0.50	0.54	mrad	−8%
$\theta_\mathbf{y}$	0.57	0.16	mrad	71%
$\theta_\mathbf{z}$	0.31	0.17	mrad	46%
$\mathbf{F_{q,max}}$	8.7	19.8	kN	-130%
bulk diameter	12	18	mm	
safety factor	12	12.2		
heat-load @ 4.7 K	0.25	0.55	W	-120%
compressor input power	1.2	2.6	kW	-120%

8.3 6S Material and dimensions choice

Once the arrangement of supports has been optimized and essential strategies to minimize the impact of backlash have been defined as done in the previous section the geometry is fixed for each dipole of the line. In the next phase of the design process the baseline material and dimensions of the supports have been chosen by analyzing three figures of merit:

- a structural integrity figure of merit related to the safety factor on the static load (Figure 8.7) (reference values used for the material properties [106, 107] are listed in Table 8.4). Properties at room temperature have been used in favor of safety, as the general trend for metals is to be stronger and more rigid when cooled to cryogenic temperatures [106]. Additionally, a thermal gradient is present on the rod, therefore a region close to the vacuum vessel has lower mechanical properties than the region of the rod closer to the cold-mass.
- a functionality figure of merit (Figure 8.8) related to the accuracy of the system during operation. This is the main parameter required so that the system is functional. Calculated on the base of Equation 7.2 including the deformation of the vacuum vessel. This figure of merit is the same as that used for the optimization fitness evaluation without penalty functions and is reported here for the sake of readability:

$$f = \frac{1}{\sqrt{\mathbf{P_e} \cdot \mathbf{P_e}}} \quad \text{with} \quad \mathbf{P_e} = (\tilde{e_1}, ..., \tilde{e_6}) \tag{8.1}$$

where $(\tilde{e_1}, ..., \tilde{e_6})$ are the maximum error of each DOF during the rotation of the gantry.

- a functionality figure of merit related the conductive heat-load (Figure 8.9) passing from the thermalization to the cold-mass, it has been calculated using thermal conductivity integrals [81, 82] supposing to have the thermalization exactly at the midpoint of the support lengthwise which has been verified being not far from the optimum configuration that minimizes the cost of cryogenics [108].

Table 8.4: *List of material properties for the compared materials for solution 6S and 8S.*

	Ti6Al4V	SS304L	Invar 36	CFRP	GFRE	
Yeld strenght	950	205	483	2000	300	MPa
Young's modulus	114	195	148	130	30	GPa

The sizing and choice of material of the support is done by imposing as sizing condition a minimum safety factor of 12 (value chosen to account for the high cycle fatigue). The safety factor of the supporting element with cross section A, loaded with a force F and made of a material with yeld strength R_y is calculated as $\text{sf} = R_y \frac{A}{F}$. Since the shape of the cross section does not enter in the previous equation the support shape can be considered as round and an equivalent diameter d_{eq} used to identify the cross-section $A = \pi \frac{{d_{eq}}^2}{4}$. Plots of the three figures of merit mentioned above in relation to the equivalent diameter are reported in Figure 8.7, Figure 8.8, and Figure 8.9.

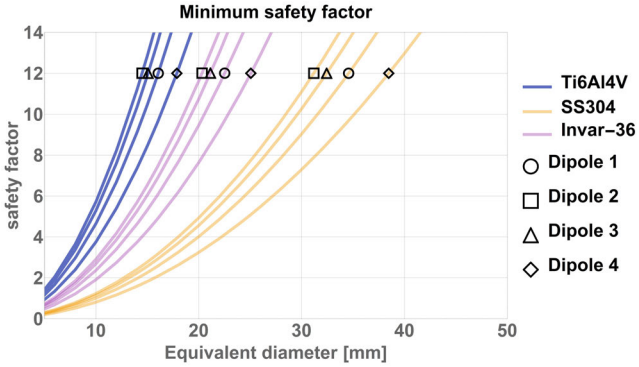

Figure 8.7: *Relation between the minimum safety factor over static loads and the equivalent diameter for each dipole (different markers) using different materials (different colors). The markers show the minimum diameter that satisfies the requirement of a minimum safety factor of 12.*

Figure 8.7 shows the safety factor in relation to the equivalent diameter for all four dipoles of the transfer line (identified by a different marker in the plot) and for the different

materials (identified by a different color). Different dipoles, assuming supports of the same material, are loaded in a different manner since their orientation on the transfer line with respect to the direction of gravity is different (see Figure 4.2). This is reflected in the different lines for the same material shown in Figure 8.7. Since the load does not depend on the elastic modulus of material for exactly constrained architecture, dipole 4 is in the most critical condition independently of the material chosen. This is evident when examining the lines of the same color in Figure 8.7, where dipole 4 requires a larger diameter to ensure a safety factor of 12. Considering the potential for series production of supports, the most straightforward approach is to adopt the support dimensions of dipole 4 for all dipoles along the transfer line. Hereafter, the values of other figures of merit are based on this assumption. The selected values for the safety factor and equivalent diameter are presented in Table 8.5.

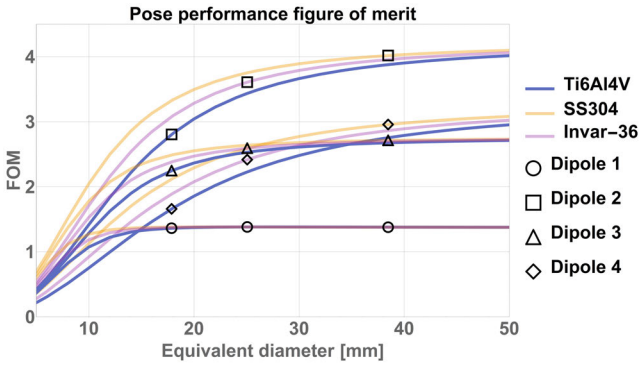

Figure 8.8: *Comparison of rigidity figure of merit for the different materials and different equivalent diameter.*

Pose performance figure of merit depends on the equivalent diameter, material of the supporting element, and the arrangement of supports with respect to the load. As can be seen from Figure 8.8 the pose performance of each dipole will set asymptotically to a finite value for large equivalent diameters. This is because when the stiffness of the supports increases the pose performance becomes a function of the rigidity of the vacuum vessel and arrangement of supports with respect to the load. On average the pose figure of merit is of the same order of magnitude ranging from 2 to 2.8 respectively for titanium supports and stainless steel supports (see Table 8.5). Only from the perspective of pose performance stainless steel would be preferable.

Table 8.5

Cryomodule	d_{eq} mm	Material	Safety factor	Heat flux to 4.7 K W	Compressor IN power kW	FOM
1	18	Ti6Al4V	15	0.54	2.6	1.36
2	18	Ti6Al4V	18	0.54	2.6	2.8
3	18	Ti6Al4V	17	0.54	2.6	2.25
4	18	Ti6Al4V	12	0.54	2.6	1.66
Total				2.16	10.2	
Average			15.5			2.02
1	38	SS304	15	4.96	23.4	1.38
2	38	SS304	18	4.96	23.4	4.02
3	38	SS304	17	4.96	23.4	2.71
4	38	SS304	12	4.96	23.4	2.96
Total				19.84	93.8	
Average			15.5			2.77
1	25	Invar-36	15	1.82	8.6	1.38
2	25	Invar-36	18	1.82	8.6	3.61
3	25	Invar-36	17	1.82	8.6	2.59
4	25	Invar-36	12	1.82	8.6	2.42
Total				7.28	34.4	
Average			15.5			2.5

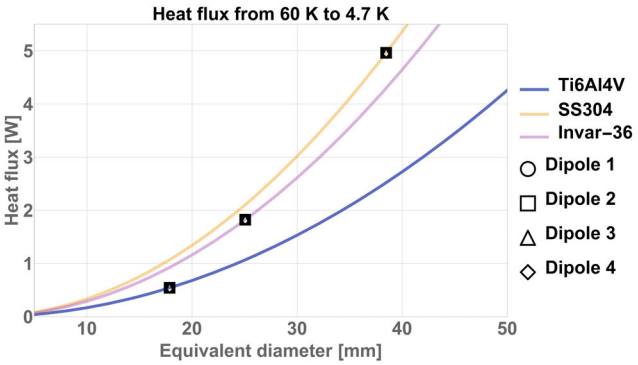

Figure 8.9: *Comparison of conduction heat load to* 4.7 K *with thermalization at* 60 K*. Cumulative value for six supports.*

Looking at the heat-flux from 60 to 4.7 K (Figure 8.9), this figure of merit does not depend on the arrangement of supports with respect to the load, so the different lines for the same material and different dipole overlap. The supports made of titanium conduct less heat for any equivalent diameter. Having sized the supports to satisfy mechanical resistance with a safety factor of 12 makes titanium 3 times more convenient than invar and 9 times more convenient than stainless steel. In conclusion, the baseline material chosen is Ti6Al4V which guarantees the bast tradeoff of all comparison figure of merits.

8.4 6S Mechanical design

This section outlines how the support arrangement obtained from the optimization routine, along with the sizing and geometry choices done in this chapter, are technically integrated into the mechanical cryostat 3D drawing with the aim of evaluating the impact of choices made and possibility to manufacture the designed system. Six tubular shaped titanium supports are used to suspend the cold mass (see Figure 8.10). Tube shaped metallic structures have a low manufacturing complexity, welding and bolting techniques can be used reliably, the same would not be true if composites are used. The supports are intercepted at mid-length by a high thermal conducting material to intercept conduction heat-flux at an intermediate temperature. Spherical joints at each end ensure to not over-constrain the system. A prismatic joint (linear guide) at the warm end allows to move the six warm joints independently. The prismatic joint is moved by mean of a lead screw turning the rotation of a screw into the linear motion. The movement of the six warm joints allows to control the position of the cold mass about all six degrees of freedom.

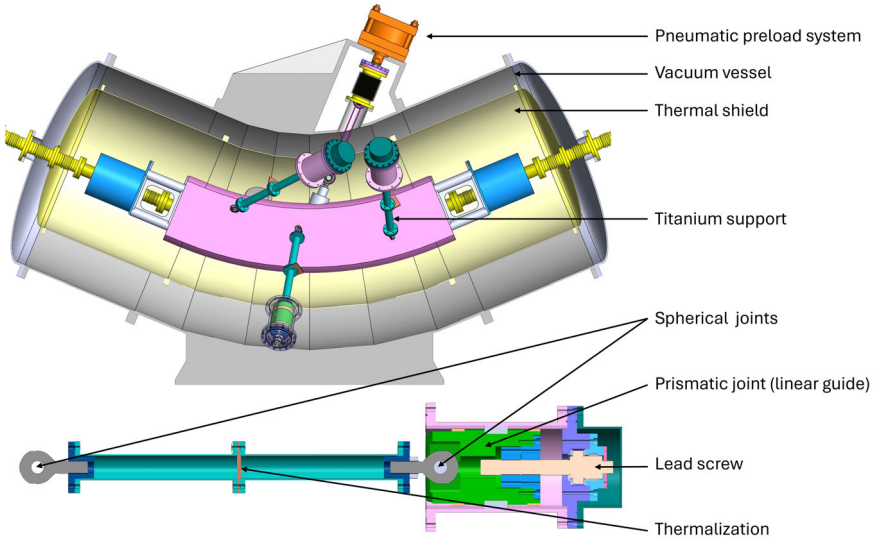

Figure 8.10: *3D model showing the main components of the parallel supporting system.*

The alignment range has been designed starting by an assessment of possible misalignements of the cold mass due to assembly and manufacturing tolerances. Monte Carlo methods have been used to estimate the distribution of errors and then a 3-sigma range of misalignements has been assumed. From this range it has been calculated the maximum travel of any warm joint in order to correct the extreme cases (Figure 8.11). A lead-screw assembly capable of moving linearly the warm joints by the calculated required amount has been designed.

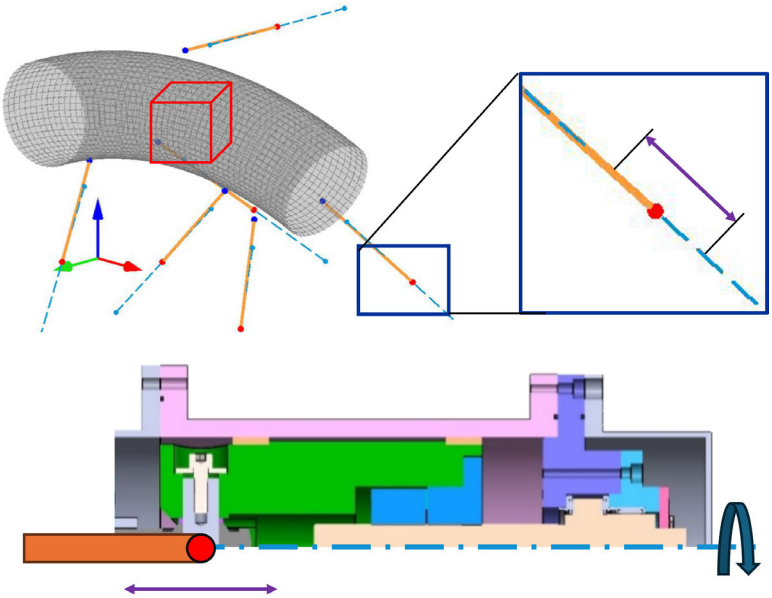

Figure 8.11: *Design of the alignment system range.*

Turning the screws manually with simple wrenches has been calculated to require too high torque, torque multiplying wrenches must be used instead (ratios between 1:5 and 1:25 are commercially available). Assuming that the lead screw thread pitch is about 1 mm and that a human can turn the wrench with a sensitivity of a quarter of a turn, the achievable sensitivity on the positioning of the magnet can be estimated to be around 0.05 mm and 0.05 mrad (at 3σ).

A pneumatic pre-load system is implemented into the supporting system and powered by standard pressurized systems (max pressure. 6 bar). The pre-load is applied to the supports to make sure a given support is constantly either in tension or in compression, never switching from one state to the other during the rotation of the machine. This system is necessary to eliminate the losses of accuracy due to backlash in the joints as discussed in Section 8.2.

8.5 8S Material and dimensions choice

The optimization of the arrangement of the supports in the 8S architecture is carried out with the same algorithm used for the 6S supporting system and reported in Chapter 7. The only difference is in the LPM used to calculate the pose of the magnet that enters in the fitness function. A different hypothesis impacting the material comparison is that backlash is recovered at warm applying sufficient pre-load simultaneously to all supports instead than using the pneumatic system.

Once the arrangement of supports had been optimized the baseline material and dimensions of the supports have been chosen by analyzing the same three figures of merit used for the sizing of the supports of the 6S solution related to the safety factor over

static loads, accuracy of the system during operation and conductive heat-loads though the supports.

Figure 8.12 shows the safety factor in relation to the equivalent diameter for all four dipoles of the transfer line (identified by a different marker in the plot) and for the different materials (identified by a different color). In contrast of the 6S supporting system, where the load doesn't depend on the elastic modulus of material, for the over-constrained architecture 8S the load depends on the stiffness of the support and also on the effect of differential thermal contractions. This can be seen from the plot since the functions are not anymore simple quadratic functions (very evident for titanium supports). The dipole in the most critical condition does depend on the material chosen unlike solution 6S. GFRE and stainless steel solutions satisfy the condition of sf $>$ 12 only for large equivalent diameters 83 mm and 147 mm respectively.

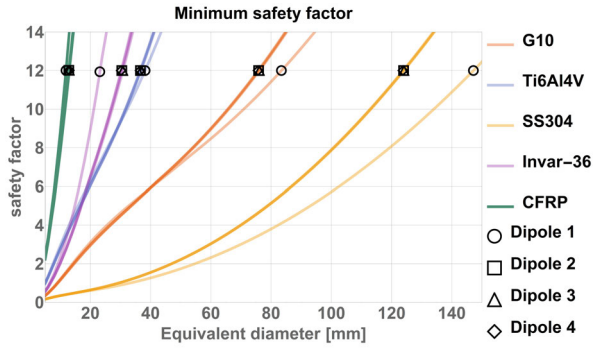

Figure 8.12: *Relation between the minimum safety factor over static loads and the equivalent diameter for each dipole (different markers) using different materials (different colors). The markers show the minimum diameter that satisfies the requirement of a minimum safety factor of 12.*

Figure 8.13 highlights again the effects of the over-constrained nature of the 8S architecture, in particular the figure of merit for the pose performance has maximum values before decreasing and setting asymptotically to a finite value (evident from the peak in the stainless steel curves). This effect is related to the stiffness and thermal contraction of the supports, as the stiffness of the supports increases the deformation due to thermal contraction generates higher internal loads.

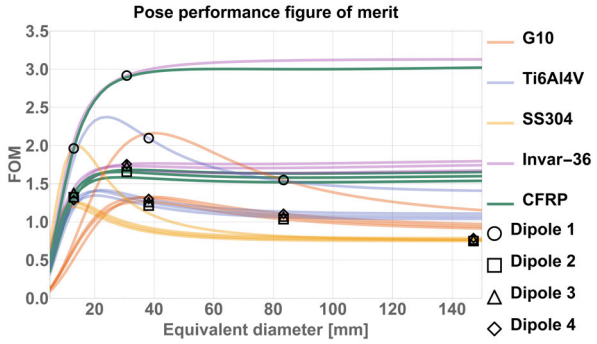

Figure 8.13: *Comparison of rigidity figure of merit for the different materials and different equivalent diameter.*

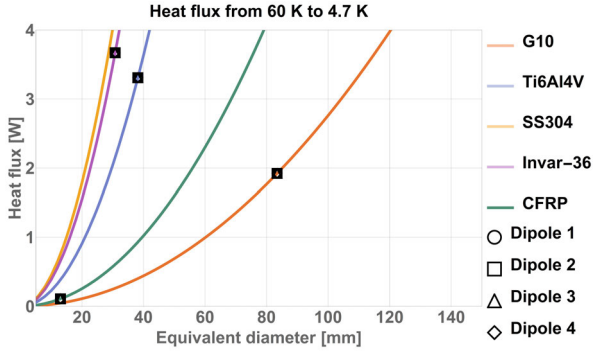

Figure 8.14: *Comparison of conduction heat load to* 4.7 K *with thermalization at* 60 K. *Cumulative value for six supports.*

(Figure 8.9) illustrates the heat-flux from 60 to 4.7 K in relation to the size and material of supports. As for solution 6S, this figure of merit does not depend on the arrangement of supports with respect to the load, so the different lines for the same material and different dipole overlap. The supports made of CFRP conduct less heat for any equivalent diameter. Having sized the supports to satisfy mechanical resistance with a safety factor of 12 makes CFRP 17 times more convenient than GFRE which is the second best alternative is terms of heat-loads.

Given the results summarized in Table 8.6, all solutions satisfy the minimum safety factor coefficient required (12). As a result of the series oriented production, some of the supporting systems of the beam transfer line are over-sized, thus the average safety factor is always greater than 12. The figure of merit for the rigidity of the system ranges between 0.77 to 2.02 respectively for SS304 and Invar-36. If it is assumed that all DOFs are at their limit value (0.6 mm or 0.6 mrad as from requirements), $f_{\min} = 0.68$. Another limit case, although highly unrealistic, considers only one of the DOF at its limit value, resulting in $f_{\min} = 1.66$. A more realistic limit is defined by the condition where two

DOF reach their extreme values. Considering the gantry rotation around the z-axis, the cold mass undergoes an equal displacement first in x at a certain angular position of the gantry and then in y when the gantry has moved of 90°. Under this scenario, the limit is given by $f_{\min} = 1.18$. For these reasons support solutions in SS304 and GFRE are deemed critical, having a an average $f <= f_{\min}$ while other solutions are still good candidates. The solution in CFRP outperforms by 17 times the second best solution in terms of heat flux to 4.7 K, therefore it has been chosen as baseline for the 8S supporting system design.

Table 8.6

Cryomodule	d_{eq} mm	Material	Safety factor	Heat flux to 4.7 K W	Compressor IN power kW	FOM
1	83	GFRE (G10)	12	1.92	9.07	1.55
2	83	GFRE (G10)	14	1.92	9.07	1.04
3	83	GFRE (G10)	14	1.92	9.07	1.07
4	83	GFRE (G10)	14	1.92	9.07	1.11
Total				7.68	36.3	
Average			13.5			1.19
1	38	Ti6Al4V	12	3.31	15.64	2.1
2	38	Ti6Al4V	13	3.31	15.64	1.21
3	38	Ti6Al4V	13	3.31	15.64	1.26
4	38	Ti6Al4V	13	3.31	15.64	1.3
Total				13.24	62.59	
Average			12.75			1.47
1	147	SS304	12	96.78	457.49	0.77
2	147	SS304	17	96.78	457.49	0.75
3	147	SS304	17	96.78	457.49	0.77
4	147	SS304	17	96.78	457.49	0.79
Total				387.12	1829.99	
Average			15.75			0.77
1	31	Invar-36	19	3.67	17.35	2.92
2	31	Invar-36	12	3.67	17.35	1.66
3	31	Invar-36	12	3.67	17.35	1.73
4	31	Invar-36	12	3.67	17.35	1.76
Total				14.68	69.39	
Average			13.75			2.02
1	13	CFRP	14	0.11	0.52	1.96
2	13	CFRP	12	0.11	0.52	1.32
3	13	CFRP	12	0.11	0.52	1.38
4	13	CFRP	12	0.11	0.52	1.29
Total				0.44	2.08	
Average			12.5			1.49

8.6 8S Mechanical design

The supporting system design represented in Figure 8.15 makes use of the double band design for the supporting element (see Figure 8.16). This design solves issues of junctions between metallic joints and composite supports. Thanks to the band geometry the fibers can be laid uni-directionally, exploiting most of their strength, without creating critical

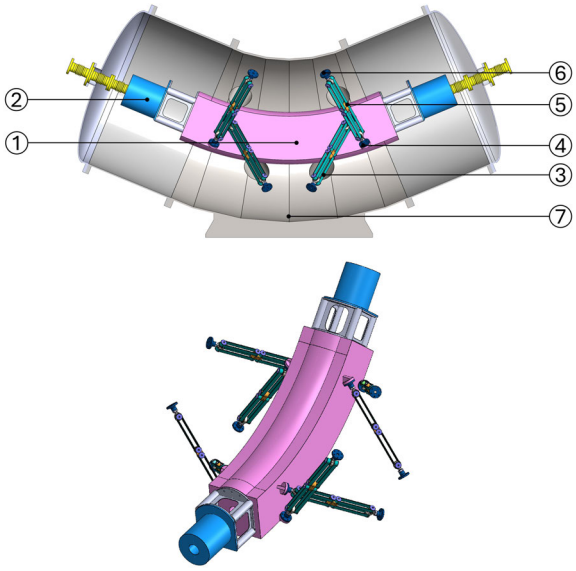

Figure 8.15: *3D model of the support architecture. (1) superconducting dipole (2) superconducting quadrupole (3) support (4) cold joint (5) thermalization (6) warm joint with 3D alignement system (7) vacuum vessel.*

points for concentration of shear stress and delamination. An intuitive example where the double-band support design is preferable to the rod-shaped design for composites is the interface between the supports and the thermalization. Ideally, for maximum effectiveness, the thermalization should split the support into two parts. This would necessitate connecting the tubular support to the thermalization using mechanical fittings or glued joints, which are critical points of failure after repeated thermal cycles. The double band geometry completely solves the problem as seen in Figure 8.16 by having the composite material free to contract without generating extra stress concentration.

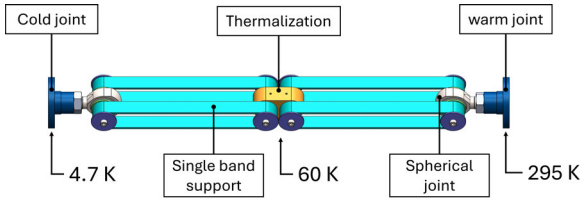

Figure 8.16: *Proposed over-constrained support sub-assembly: cold joint at* 4.7 K*, (2) single band shaped support, thermalization, rod end, warm joint at* 295 K*.*

A possible alignment strategy for solution 8S is here proposed:

1. the position of the cold mass at room temperature is assumed as nominal, the misalignment of the position of the cold mass at operating temperature is calculated by mean of the LPM;

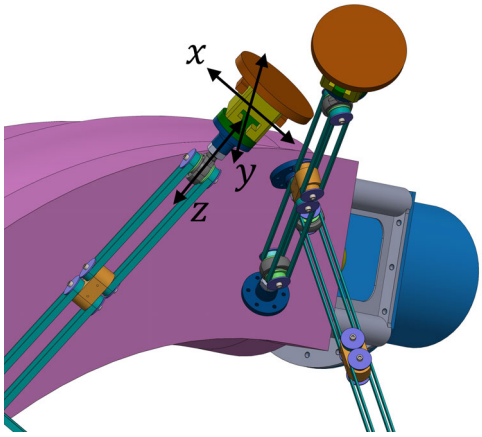

Figure 8.17: *Schematic illustration of a possible positioning system of the warm joints for solution 8S.*

2. the target position of the cold mass at room temperature is shifted accordingly to the misalignments calculated at step 1;
3. the cold mass is positioned within the vacuum vessel at the target position (step 2) at the best of the position measurements uncertainty of an external positioning stand;
4. the eight supports are connected to the warm joint 3D positioning system (Figure 8.17), assuming there is no internal load on supports;
5. minimum pre-load is applied to recover backlash, internal load is monitored;
6. the external positioning stand is removed;
7. full pre-load is applied.

A possible limitation of this procedure is related to the need of alignment of the cold mass whit the use of an external positioning stand, an operation easier to perform on the ground rather than on the machine. This means that first the reference system of each cryostat must be located with respect to the reference frame on the machine to take into account the manufacturing tolerances of the gantry. Next, the cryostat is lowered on the ground and the cold mass positioned according to the previously generated frame on the cryostat thanks to the external positioning stand, which must have on its own alignment capabilities. Finally the cold mass assembled cryostat is assembled on the machine.

9 COMPARATIVE ANALYSIS OF THE SUPPORTING SYSTEMS IN THE GANTRY STUDY CASE

This chapter presents the comparison of the exactly constrained supporting system (6S) and the over-constrained one (8S). The best combination of material and dimensions for each configuration has been discussed in Chapter 8, here the comparison of the two optimal solutions is given. The following figures of merit or comparison criteria are used for the final assessment:

- a figure of merit for the accuracy for each DOF calculated as the maximum error along the beam transfer line (for all cold elements),
- a figure of merit related to structural integrity, calculated as the safety factor over static nominal loads,
- a figure of merit related to the heatflux through supports from the thermal shield to the cold mass,
- a figure of merit related to the sensitivity of the system to variations in geometry and material properties, calculated as the standard deviation of the pose of the cryogenic device,
- a figure of merit related to the structural integrity, calculated as the safety factor over transportation and handling loads, assumed as static,
- a comparison of the natural frequencies of the two solutions

The figures of merit associated with the accuracy performances, nominal structural integrity and heat-flux are compared in Table 9.1. The other three comparisons are done in the following sections.

For the final assessment presented in this chapter, the sole figure of merit f Equation 7.2, used in previous chapters, can be deceiving when comparing completely different architectures. The same value of f can result from an architecture that has for example $\mathbf{P_{e,A}} = (0.6, 0, 0, 0, 0, 0)$ or another that has $\mathbf{P_{e,B}} = (0.24, 0.24, 0.24, 0.24, 0.24, 0.24)$. This was not relevant for comparisons done in previous chapters since changing exclusively the material or support dimensions without changing the support arrangement does not vary how errors are distributed between all DOFs but only how much they are scaled ($\mathbf{P_{e,A1}} = \alpha \mathbf{P_{e,A2}}$).

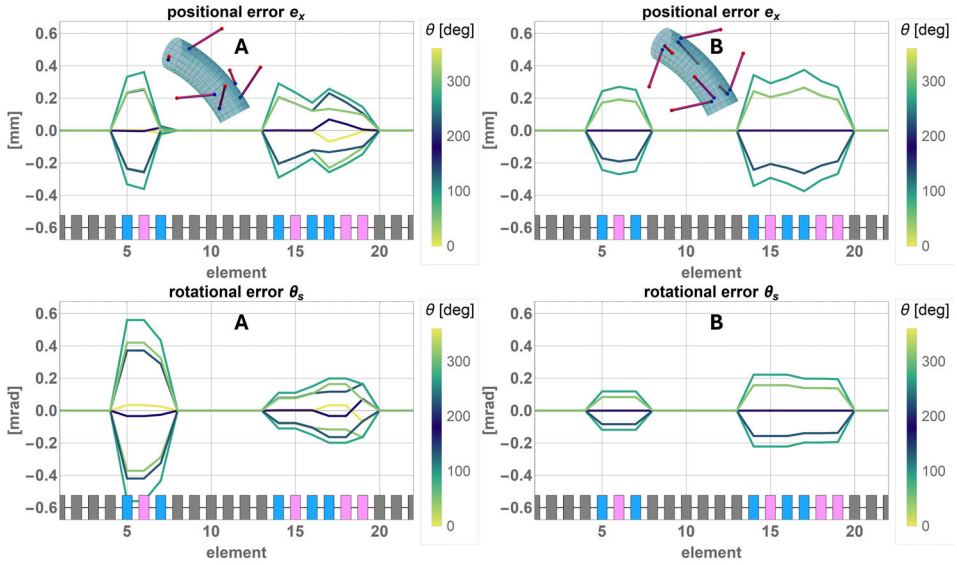

Figure 9.1: *comparison between architecture "6S" and architecture "8S" of position and rotation misalignments of superconducting elements of the transfer line due to the elasticity of supports and vacuum vessel during a* 360° *rotation of the gantry.*

An illustration of the positional error e_x and the rotational error θ_s along the transfer line is given in Figure 9.1. Both optimized solutions are rigid enough for the requirements (Table 3.1): solution 8S results more rigid than solution 6S, improving on almost all DOFs by 20% to 73% except for e_x where 8S is less stiff than 6S, although with a difference of only 4%. Both solutions are sound mechanically having an average safety factor of 15.5 and 12.5 respectively for solution 6S and 8S. Cryomodules of solution 8S are much more similar among each other (internal loads), this does not results in an over-sizing of the supports of some cryomodules as much as for solutions 6S. The use of CFRP in solution 8S decreases the heatloads in the system requiring up to 80% less power to extract heat at 4.5 K.

9.1 Sensitivity analysis

The two support configurations have been analyzed under the point of view of their sensitivity to variations in input parameters. For example, for solution 8S, random variations in the pre-load applied to each of the supports can generate an unwanted displacement of the cold mass, hard to detect and correct in the assembly phase. Some input parameters of the sensitivity study are fundamental, while others are derived from them. For example, the length contraction of supports is a derived input quantity that depends on their lengths, which is the fundamental input. A list of Fundamental input parameters is given in Table 9.2.

All random effects generated by variations of fundamental input parameters are:

- deformation of the support elements,
- deformation of the vacuum vessel due to loads transferred by support elements,

Table 9.1: *Comparison of the first three figures of merit for solution 6S and 8S.*

		6S	**8S**	**% improv.**
Material		Ti6Al4V	CFRP	
Geometry		tube	double band	
Equivalent diameter	mm	18.0	13.2	
e_x	mm	0.36	0.37	-4%
e_y	mm	0.32	0.24	23%
e_s	mm	0.45	0.36	20%
θ_x	mrad	0.16	0.04	73%
θ_y	mrad	0.36	0.12	65%
θ_s	mrad	0.56	0.22	60%
Max load	kN	19.9	22.3	
Safety factor (static nominal loads)		15.5	12.5	
Heat flux @ 4.5 K	W	2.16	0.44	80%
Compressor input power	kW	10.2	2.08	80%

Table 9.2: *List of fundamental parameters and their variation ranges considered as input parameters for the sensitivity analysis.*

Fundamental parameter	**6S**	**8S**	**value (3σ)**	
Equivalent diameter of a support	YES	YES	0.1	mm
Length of a support	YES	YES	0.1	mm
Elastic Modulus of material	YES	YES	5	%
Position measurements uncertainty	YES	YES	0.15	mm
Sensibility of positioning system	YES	NO	0.05	mm
Pre-load	YES	YES	5	%

- deformation of the vacuum vessel due to pre-load system,
- displacements due to the cool-down process,
- tolerances stack-up in the assembly chain from the main structure up to the cold-mass.

With respect to Table 5.1 some effects has not been considered:

- the backlash because of the assumption to use the pneumatic pre-load system discussed in Section 8.2;
- the deformation of the main structure since is not relevant for the comparison of different suspension systems for the cold mass;
- the deformation of the vacuum vessel due to differential pressure and own distributed weight because considered as a second order effects.

9.1.1 Sensitivity analysis of solution 6S

During cool-down solution 6S behaves like in Figure 9.2 (left): since the cool-down is not generally symmetric, the system must be put in an initially misaligned position at room temperature (red in figure), this is done by moving all 6 warm prismatic joints of a calculated distance q_{ni} from the reference origins $H_{n0,i}$. During cool-down, the warm position of the warm prismatic joints H_{ni} is fixed, the cold mass moves from the misaligned position to the nominal position at cold.

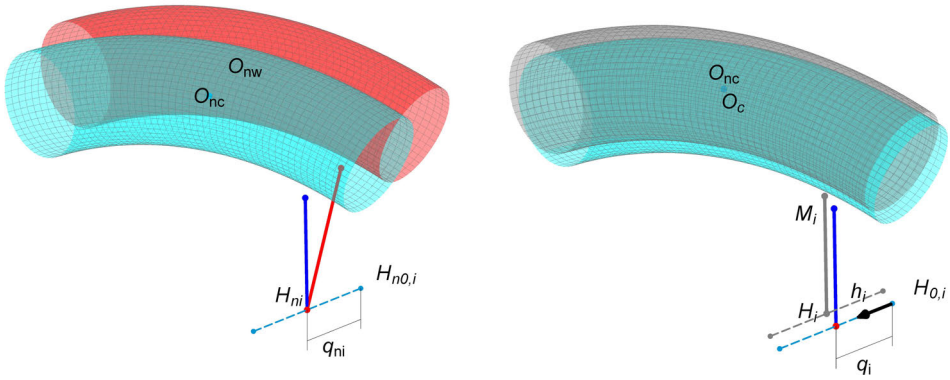

Figure 9.2: *Cool-down displacement of solution 6S with nominal dimension and position of warm joints (left). Final position after cool-down in a system with real dimensions (right).*

Mathematically, the distribution of the pose in response to applied variations is calculated as follows:

1. the IPK routine (Section A.1) is used with the cold dimensions, imposing the pose of the cold mass in the nominal position and finding the position of each warm joint ($\mathbf{q}_{n0}$), which is the same at room temperature and at operational temperature;
2. variations of fundamental parameters are used to define the real geometry:

2.1. the position of real warm joints $\mathbf{H}_{0,i}$ is found by varying its position according to a Gaussian distribution, with standard deviation associated to the position measurements uncertainty (Table 9.2);

2.2. the direction of the guide of the prismatic joint $\mathbf{h_i}$ is varied by assuming it is measured from 3 points on the surface of the support flange (violet laser reflectors in Figure 9.3) of the vacuum vessel. Each point is assumed to be within a sphere of radius $3\sigma = 0.15\,\text{mm}$ (position measurements uncertainty Table 9.2). This virtual measure is repeated 10 times to have an average of the direction of the guide mimicking the surveying procedure;

2.3. each component of the nominal initial joint vector $\mathbf{q}_{n0}$ is varied according to the sensibility of positioning system (Table 9.2) finding the real initial joint vector $\mathbf{q}_{n0}$;

2.4. the position of $\mathbf{H}_i$ is calculated from results of steps 2.1 - 2.3 from Equation A.1;

2.5. the position of cold joints in the tool reference frame ${}^1\mathbf{M}_i$ is found by varying its position according to the position measurements uncertainty (Table 9.2);

2.6. the length of each support is varied according to the respective parameter in Table 9.2.

3. the DPK routine (Section A.2) is performed, using as input parameter results of step 2, to calculate the pose of the cold mass at operational temperature (Figure 9.2 right). Additionally, the deformations of the vacuum vessel and of the supports are calculated as formalized in Section 5.1 by varying the external load given by pre-load, elastic modulus and the cross section of supports (function of the equivalent diameter Table 9.2).

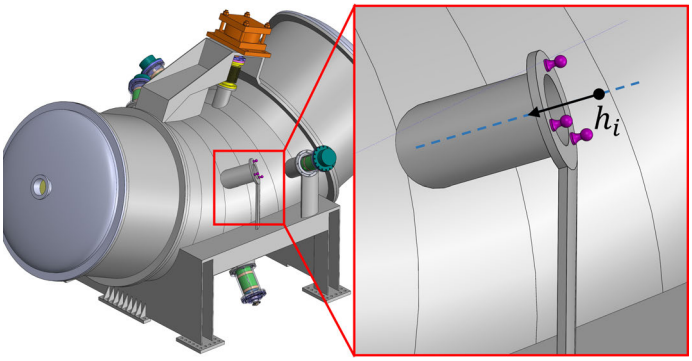

Figure 9.3: *Position on the vacuum vessel of points probed in the virtual assessment of the direction of the prismatic joint guide (step 2.2).*

As can be seen from the above procedure all fundamental inputs have been used combined together in the LPM developed. This guarantees more meaningful overall results rather than evaluating separately every contribution and having the problem of choosing a formal and accurate way of combining the sub-results. The procedure of step 1-3 is repeated for 10000 times to have a discrete statistic. Note that the LPM developed in

this work enables such evaluations time-wise in a much cheaper way than running classical FEAs varying the geometry.

9.1.2 Sensitivity analysis of solution 8S

The sensitivity analysis for the over-constrained solution depends, as for solution 6S, from the alignment procedure chosen (Section 8.5). Mathematically, the distribution of the pose in response to applied variations is calculated as follows:

1. the position of the eight cold joint with respect to the cold mass reference system is varied within a sphere with a radius of 0.15 mm (position measurement uncertainty Table 9.2);
2. the cold mass is positioned in the global frame by varying its position according to the position measurement uncertainty;
3. the length of each support is varied according to the respective parameter in Table 9.2.
4. the warm joints positions are varied in the global frame according to the position measurement uncertainty and the length of supports (step 3). This is done because of the assumption of no extra stress during the positioning, so the position of the cold joint, position of the warm joint and length of the support must be congruent;
5. the LPM is used varying the pre-load, thermal contraction, elastic modulus, length and diameter of the rods according to the relative fundamental parameters;
6. the uncertainty in the position of the cold mass is added back to results of step 5.

Note that the LPM for the over-constrained system calculates displacements due to stress states only, and is independent from rigid body motions. Step 2 act as a rigid body motion and is used to calculate the non nominal arrangement of each support and their influence on the stress-state and consequently on the relative displacement. Therefore, the variation in position of the cold mass at step 2 must be summed straight to the results of the LPM routine (step 5). The procedure of step 1-6 is repeated for 10000 times to have a discrete statistic.

9.1.3 Sensitivity analysis comparison of 6S and 8S

Quantitative results of the sensitivity analysis of the 6S and 8S supporting systems in response to variations of input parameters (Table 9.2) are reported in Table 9.3 and Table 9.4. Qualitative results are reported in Figure 9.4, Figure 9.6, Figure 9.5, and Figure 9.7. Overall the exactly constrained solution (6S) seems more sensitive to variations of input parameters. The axial internal actions on supports seem to be almost equally influenced, with 104 N of standard deviation (1σ) on average for the 6S supporting system and 90 N (1σ) for the 8S supporting system.

Table 9.3: *Results of the sensitivity analysis for both the 6S and 8S supporting system. 1σ standard deviation of the internal axial action for each of the supports.*

	Rod1	Rod2	Rod3	Rod4	Rod5	Rod6	Rod7	Rod8	
Force Std. 1σ (6S)	97.08	89.55	120.85	134.62	93.55	90.60			N
Force Std. 1σ (8S)	86.64	86.96	87.16	86.83	93.90	93.57	93.71	94.10	N

Table 9.4: *Results of the sensitivity analysis for both the 6S and 8S supporting system. 1σ standard deviation of the position and rotation of the cold mass.*

DOF	e_x	e_y	e_z		θ_x	θ_y	θ_z	
Pose Std. 1σ (6S)	0.28	0.06	0.13	mm	0.37	0.51	0.15	mrad
Pose Std. 1σ (8S)	0.02	0.02	0.02	mm	0.02	0.02	0.02	mrad

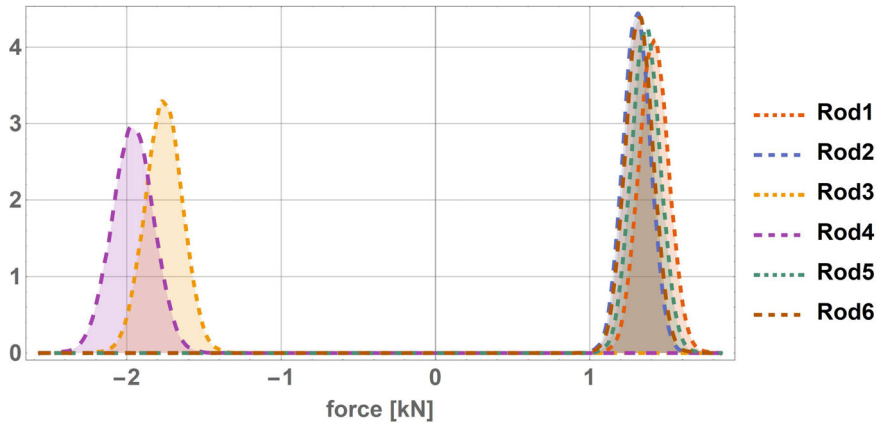

Figure 9.4: *Resulting forces of the sensitivity analysis of the 6S LPM.*

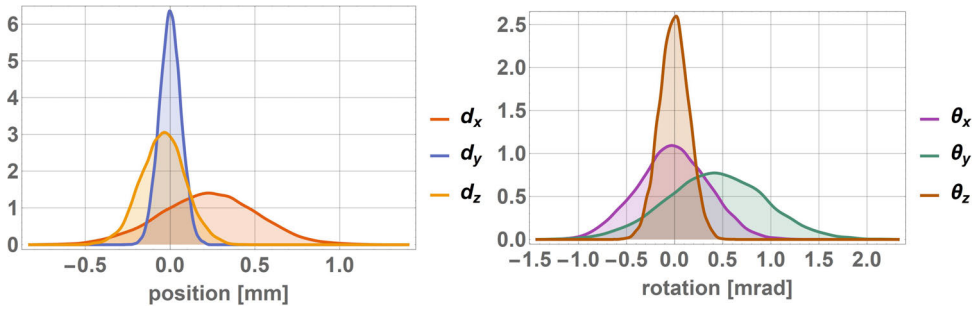

Figure 9.5: *Resulting position and rotation of the sensitivity analysis of the 6S LPM.*

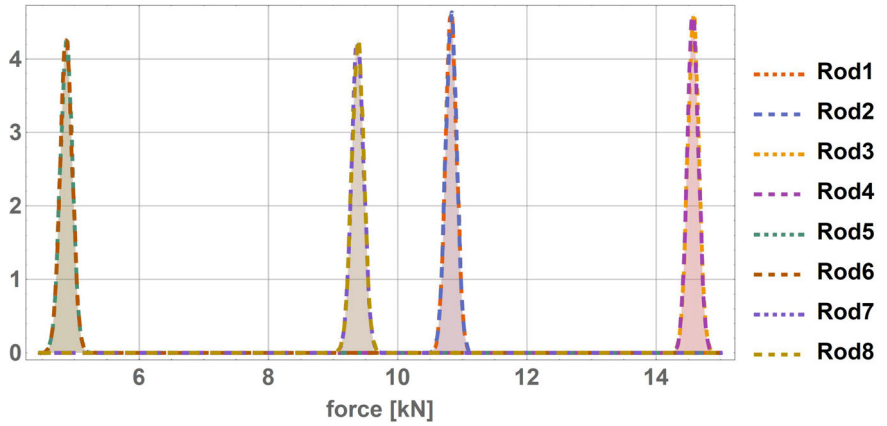

Figure 9.6: *Resulting forces of the sensitivity analysis of the 8S LPM.*

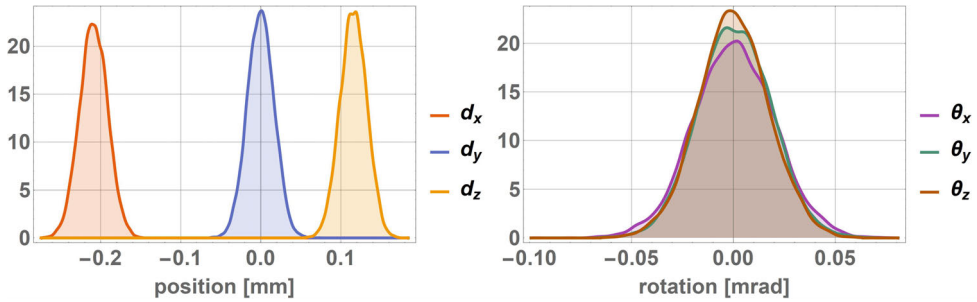

Figure 9.7: *Resulting position and rotation of the sensitivity analysis of the 8S LPM.*

9.1.4 Comparison of sensitivity impact on beam parameters

The impact of design choices proposed in this thesis on the beam transported through the gantry beam transfer line has been estimated from studies done in coordination with experts from the Italian National Center of Oncological hAdron therapy (CNAO). In addition to the deformation of the supports and cryostat calculated from the developed LPMs, and the random errors estimated in the above reported sensitivity analysis, the author has provided also the contribution of the deformation of the main gantry structure. The results provided by the Author have been used to optimize the positioning of the elements on the transfer line in order to maximize the effectiveness of beam corrections. The metrics used to measure the performance of the transfer line are: the beam envelope radius at different gantry positions and the percentage of correction kicks which exceed hardware capabilities of correctors already used at CNAO. The complete methodology used for this study will be described in [109]. The results in terms of beam envelope radius are reported in Figure 9.8 and Figure 9.9. The beam envelope is simulated running thousands analysis in MADX supposing the random error distributions calculated in the previous sections. Maximum envelope considering the full data (100th percentile) and only the data up to the 95th percentile show that the maximum envelope is reduced

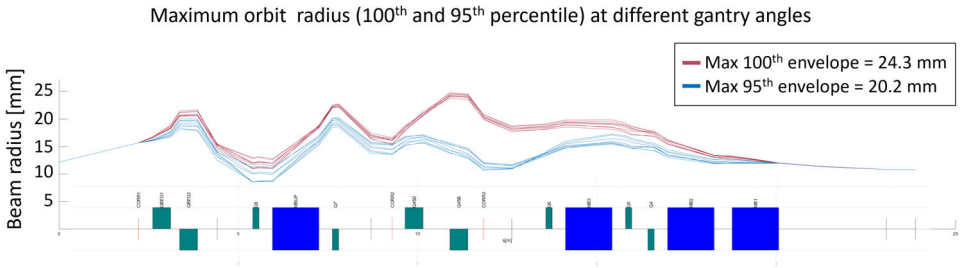

Figure 9.8: *Beam envelope in transfer line based on 6S supporting architecture considering deformation of supports, cryostat, main gantry structure and impact of random errors. Results courtesy of CNAO.*

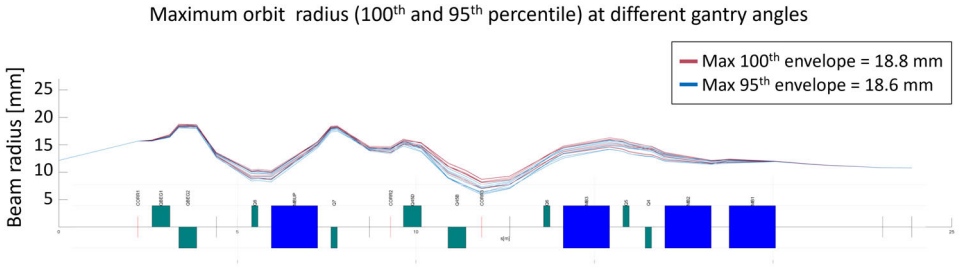

Figure 9.9: *Beam envelope in transfer line based on 8S supporting architecture considering deformation of supports, cryostat, main gantry structure and impact of random errors. Results courtesy of CNAO.*

using solution 8S under the current hypothesis on system sensitivity. The envelope radius is 24.3 mm and 18.8 mm respectively for solution 6S and 8S. Both structures respect the beam envelope radius requirements of 26.7 mm related to the estimated good field region of the magnetic field of the superconducting dipoles [110] (calculated as 2/3 of the magnet bore radius). The percentage of correction kicks that exceed the current hardware capabilities (CNAO machine) expresses the probability of having beam that cannot be corrected and could result in beam losses. This maximum percentage is 2.5 % for solution 6S and null for solution 8S, meaning that without upgrading the current technology of warm correctors used at CNAO, or additional measures during alignment and commissioning, the transfer line may be subject to beam losses in case of solution 6S while solution 8S results more stable under the current theoretical alignment hypothesis.

9.2 Analysis of transportation and handling loads

During transportation and handling, extra accelerations along directions x, y, and z may result in loads on supports that are higher than those experienced during nominal operation of the machine. This section analyzes the performances of the two supporting systems (6S and 8S) proposed under transportation and handling loads. The figure of merit used to compare the two solutions is the minimum safety factor over mechanical resistance measured on all the supports when different loading conditions are applied.

During transportation and handling, the cryostat may be shipped on the road, ship or rail and be moved by cranes. Accelerations during transportation are commonly defined as longitudinal when in the direction of travel, sideways when transversal to the direction of travel and vertically when aligned with the direction of gravity. Different sources propose different longitudinal, sideway and vertical accelerations experienced by cargo. For example, the Transport Information Service (TIS) from the German Insurance Association, addressing "Load values as specified in the Guidelines for Packing of Cargo Transport Units" [111] suggests respectively extra accelerations of 4.0 G, 0.8 G and 0.8 G (longitudinal, sideway and vertical). Another study focused on measuring the transportation environment effects (vibration and acceleration levels) in container shipments using multiple modes of transport, originating in Hungary and destined for Mexico, India, and China over several weeks [112]. This last article shows that "extreme acceleration levels in vertical direction (9.37 G) occur while containers are handled in a seaport, and in sideway (4.45 G) and longitudinal (5.55 G) directions while they are transshipped by truck to rail container terminals". In this work, as a conservative measure, the highest values from both sources have been used.

Since the supporting system does not resist loads equally in all directions, it is assumed that the cryostats are positioned on transportation vessels according to the following guidelines: the directions x, y and z as defined in LPMs are respectively aligned with the sideway, longitudinal and vertical transportation directions. The chosen values rounded to 4.5 G, 5.6 G and 9.5 G (sideway, longitudinal and vertical) have been assumed as amplitude to be added to gravity, each acceleration acting in both directions, generating six loading conditions listed in Table 9.5.

Table 9.5: *Load cases considered for transportation and handling loads. G is the standard value for Earth gravity.*

Load cases	LPM dir.	Case 1	Case 2	Case 3	Case 4	Case 5	Case 6	
Sideway	x	4.5	0	0	−4.5	0	0	G
Longitudinal	y	0	5.6	0	0	−5.6	0	G
Vertical	z	−1	−1	8.5	−1	−1	−10.5	G

The same loading conditions have been applied as external loads in the LPMs of both 6S and 8S for all four dipoles of the gantry beam line multiplying accelerations listed in Table 9.5 for the mass of the different cold masses. For both solutions trasportation and handling are assumed to happen at room temperature conditions. Solution 6S has been assumed to be transported without pre-load applied since the geometry of supports is able to withstand compressive loads. Solution 8S has been assumed pre-loaded with 38 kN in order to have always the supports under tension even during transportation, otherwise the supporting system can collapse.

Results in terms of safety factor over the mechanical resistance are reported in Figure 9.10 and Figure 9.11 respectivelty for solution 6S and 8S. For both supporting systems load case 6 results in the worst safety factor, respectively about 2.3 and 6.3. Solution 8S guarantees a 2.7 greater safety margin during transportation and handling phases with respect to solution 6S. The high symmetry in solution 8S lets all supports be loaded

almost equally for all load cases and dipoles of the beam line. Additionally, the use of CFRP in 8S instead of titanium for 6S guarantees higher safety margins because of the higher mechanical resistance. Both solutions can be judged safe for transportation and handling: the required safety factor for transportation and handling can be much smaller than the value of 12 used during the sizing of the supports in nominal conditions as high cycle fatigue is not present in this phase. Solution 6S, to increase the safety factor over transportation and handling loads, can benefit of a temporary additional supporting system during transportation and handling, a measure which is common in transportation of cryostats.

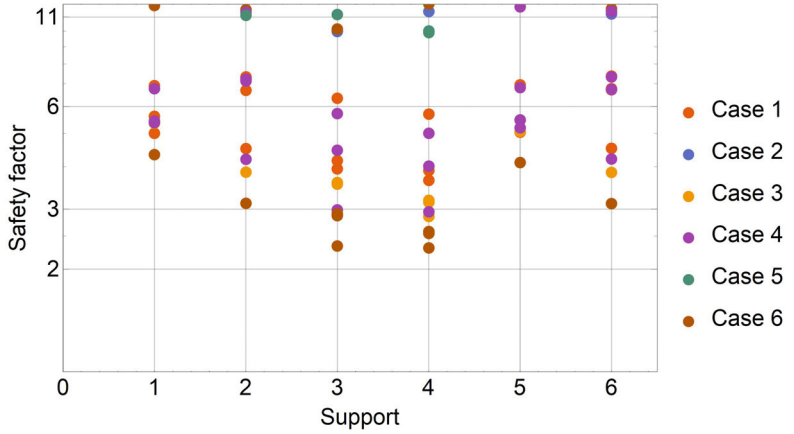

Figure 9.10: *Results of the safety factor for each rod in supporting system 6S for the different transportation and handling load cases.*

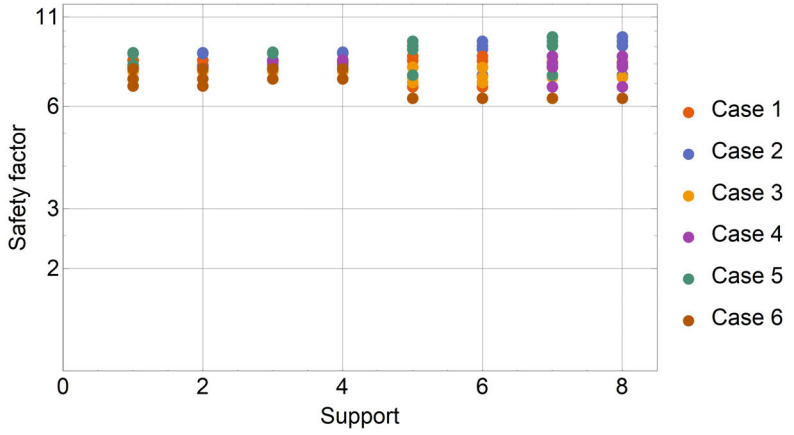

Figure 9.11: *Results of the safety factor for each rod in supporting system 8S for the different transportation and handling load cases.*

9.3 Analysis of natural frequencies of the systems

Table 9.6: *Natural frequencies and ratio of effective mass over total mass for solution 6S.*

Mode	Frequency Hz	X direction	Y direction	Z direction	Rotation X	Rotation Y	Rotation Z
1	7.04	0.2927	0.0000	0.0365	0.0000	0.0946	0.0000
2	23.91	0.0000	0.3420	0.0015	0.0069	0.0005	0.0763
3	27.16	0.0412	0.0093	0.2720	0.0008	0.1108	0.0000
4	30.36	0.2208	0.0004	0.2159	0.0001	0.0973	0.0001
5	37.34	0.0019	0.3553	0.0010	0.0421	0.0015	0.1370
6	54.19	0.0003	0.0134	0.0000	0.0194	0.0002	0.1512
7	86.21	0.0000	0.0131	0.0000	0.1968	0.0000	0.0032
8	92.037	0.0787	0.0000	0.0076	0.0000	0.1960	0.0000
9	123.08	0.0112	0.0000	0.1085	0.0000	0.0013	0.0000
Sum		0.65	0.73	0.64	0.27	0.50	0.37
Dipole mass/total		0.57	0.57	0.57	0.07	0.45	0.37

Table 9.7: *Natural frequencies and ratio of effective mass over total mass for solution 8S.*

Mode	Frequency Hz	X direction	Y direction	X direction	Rotation X	Rotation Y	Rotation Z
1	23.27	0.6060	0.0000	0.0000	0.0000	0.0039	0.0000
2	31.73	0.0000	0.6714	0.0000	0.0109	0.0000	0.0000
3	40.21	0.0000	0.0000	0.5939	0.0000	0.0000	0.0000
4	41.70	0.0008	0.0000	0.0000	0.0000	0.4426	0.0000
5	50.69	0.0000	0.0000	0.0000	0.0000	0.0000	0.4356
6	68.85	0.0000	0.0003	0.0000	0.0156	0.0000	0.0000
7	115.21	0.0000	0.0597	0.0000	0.1318	0.0000	0.0000
8	145.51	0.2908	0.0000	0.0000	0.0000	0.0282	0.0000
9	150.76	0.0000	0.0000	0.0182	0.0000	0.0000	0.0000
Sum		0.90	0.73	0.61	0.16	0.47	0.44
Dipole mass/total		0.57	0.57	0.57	0.07	0.45	0.37

Natural frequencies of solution 6S and 8S have been compared for the first dipole of the gantry beam line. The natural frequencies have been simulated by mean of FEA chaining the results of different analysis: the temperature distribution from a steady state thermal analysis is used in a static structural analysis to get the stress state after cool-down, the stress state is used in a modal analysis to get the natural frequencies and participation factors γ_i (in ANSYS notation). Results are reported in Table 9.6 and Table 9.7 in terms of the ratio of effective mass over the total mass of the assembly ($M_{eff,i}/M_{TOT}$ with $M_{eff,i} = \gamma_i^2$). This ratio expresses how much a given mode contributes to the vibration response of the analyzed system. Usually to identify the main frequencies of the system are analyzed the first n modes that have a sum of $0.95 \leq \sum M_{eff,i}/M_{TOT} < 1$ meaning that those frequencies contribute to 95–100% of the vibration response of the system. In this case, the cold mass is not the only massive element of the simulated geometry, the vacuum vessel roughly weighs 1 tonne. Therefore, the parameter to understand if all major modes are being considered is given by the ratio of the dipole mass over the total mass (or ratio of inertia for rotations). These values are reported in the last row of Table 9.6 and Table 9.7.

Solution 8S exhibits by average higher natural frequencies although not drastically

different. Solution 8S shows a more decoupled response of the system: modes 1 to 5 being rigid body movements of the dipole as they effective mass/total mass is greater than the dipole mass/total mass and no other DOFs sees a relevant $M_{eff,i}/M_{TOT}$ ratio. Given these preliminary results on natural frequencies both solutions are comparable as values do not drastically differ. Further studies and tuning of the supporting system may be needed in both cases to remove low natural frequencies before proceeding with a testing campaign and prototyping.

9.4 Chapter conclusions

The designed and optimized supporting systems 6S and 8S have been compared to each other in terms of accuracy performances under load during the rotation of the machine, heat-flux through supports, sensitivity to variations of input parameters, performance during transportation/handling and natural frequencies of the cryostat. Aside from the natural frequencies of the two systems which are comparable between the two supporting systems. Solution 8S performs overall better than solution 6S. Thanks to the viability of use of CFRP for solution 8S heat-flux see a great reduction from 2.16 W to 0.44 W at 4.7 K. This consequently reduces the power required by compressors in the cooling system passing from 10.2 kW for solution 6S to 2.08 kW for solution 8S. Solution 8S performs better also in terms of accuracy, with reductions from 20% to 73% of losses of accuracy due to elastic deformations during the rotation of the machine. A sensitivity analysis has been done to assess the sensitivity of the design solutions to variations of input parameters, such as nominal material mechanical properties. Additionally, the impact of uncertainties in measurements during the assembly and alignment phase has been considered in the sensitivity analysis. Standard deviations with respect to all six DOFs have been measured as a figure of merit of the sensitivity of the solutions. Solution 8S resulted about 10 times less sensible. This result is related to the greater displacement of solution 6S during cool-down, and how even small uncertainties in the position of components at room temperature propagate after cool-down. Solution 6S can benefit of the possibility of automating the positioning of the warm prismatic joints, feasible already with the current design. This can help reducing the impact of uncertainties by applying a feedback control system. Regarding transportation and handling performances, supports in solution 8S results more homogeneously loaded thanks to the symmetries increasing the safety margin over transportation and handling shocks. The safety margin over static loads given by accelerations is respectively 2.3 and 6.3 for solution 6s and 8S, with accelerations of 5.6 G longitudinally, 4.5 G sideway and 10.5 G vertically.

In conclusion for the application case of the rotating gantry for medical treatments, if the possibility of automation is excluded, solution 8S is deemed more performing than solution 6S. Solution 6S can become greatly advantageous if the supporting system is automatized, thanks to the exactly constrained parallel mechanism architecture, compensating the losses of accuracy due to elastic deformation with active positioning. The automation of solution 6S can recover elastic deformations not only of the cryostat, but also of the gantry main structure, enabling less stringent requirements on the rigidity of the gantry and therefore a considerable reduction in weight of the complete machine.

CONCLUSIONS

This thesis contributes to the mechanical engineering field by proposing a novel model that can be used to design and optimize the rod supporting system of cryogenic devices under a generic variable load. Through a comprehensive literature review and original structured mathematical modeling, it identifies and addresses a key gap in the design of support systems under general variable load conditions. Two alternative support architectures: one statically determinate (6S), the other over-constrained (8S) are proposed, mathematically modeled, validated and optimized. The resulting insights not only advance the state of the art in support system design but also provide tools that can be generalized to a range of cryogenic applications such as: accelerator cryogenic components that can be developed in the future, superconducting radio frequency cavities, optical alignment systems for cryogenic devices in high-energy physics experiments, superconducting generators for wind turbines, and supporting systems in the space industry.

Key findings in this thesis include:

1. The novel mathematical Lumped Parameter Models (LPMs) are adaptable to a wide range of rod support configurations (six or more rods) and enable rapid evaluation of system performance such as position of the cryogenic device and load distributions in supports.
2. The LPMs describe supporting systems that are arranged in configurations not necessarily symmetric, and can model a system where supports have their own dimensions and material which may differ from one another.
3. The LPMs show strong agreement with FEA results, achieving accuracies of 98.6% and 99.4% for the general 8 and 11 supports models. Accuracies of 97–98.5% have been achieved for solution 6S and 8S designed for the gantry study case.
4. The proposed LPMs outperform FEA in terms of calculation speed by 20 times, measurement achieved running the LPM and FEA on the same hardware.
5. Optimization using a parallel genetic algorithm resulted in notable performance gains over manually optimized designs in the specific case of the gantry application, particularly in position accuracy robustness and thermal efficiency. The computer aided optimized solution has been proven to be by average 16% and up to 83% better in terms of accuracy during the rotation of the gantry. The computer aided optimized solution has been proven to require half of the pre-load needed by the initial designed supporting system to eliminate backlash. This translates into a reduction of about 44% of the internal actions in the supports and consequently of the heat-flux for the optimized 6S configuration. The heat-flux reduction allows a reduction from 19.2 kW to 10.4 kW of the power needed by compressors in the cooling system of the machine.

This work contributes to the cryogenic device engineering field by providing a validated wide modeling framework, qualitative advantages with respect to classical FEA analysis include:

1. simplicity of the model, thanks to the limited set of essential parameters in the LPM, the model can be used by a wider community of designers and engineers, allowing to achieve accurate results almost independently from the level of expertise that is instead highly required to run accurate FEA analysis.
2. insightfulness of the model, thanks to its simplicity, the developed LPM offers clear direct insights into the fundamental relationships that govern the system. Designers and engineers can have a faster and clearer grasp on the influence of relevant parameters on crucial output quantities, boosting the capability to choose optimal configurations of supports before running computational expensive FEA.

The developed model can be used for fast, flexible evaluation of symmetric and non-symmetric rod supporting structures in cryogenic environments subject to non-variable and variable loads. Possible evaluations include:

1. Large scale sensitivity studies, by varying the most relevant driving parameters of the design and addressing the impact of their variations to the mechanical system performances and, in case of accelerator technologies, the crucial impact of such variations on accelerator beam parameters.
2. Material and geometric optimization strategies that balance structural performance with thermal load constraints and can be easily tuned to other optimize other target quantities by introducing new objective functions in the proposed optimization algorithm.
3. Support arrangement optimization that include realistic boundaries given by mechanical system integration.

The modeling, optimization, and comparison strategies developed in this thesis extend beyond the specific case of superconducting magnets for hadron therapy. They reflect a more general design philosophy centered on computationally efficient modeling tools that enable deep exploration of complex, highly constrained engineering problems.

The proposed and validated LPM framework supports a shift away from common approaches based just on experience and trial-and-error approaches based on finite element methods toward more digitally assisted designs. In particular, the ability to evaluate thousands of configurations in a fraction of the time required by traditional FEA enables early-stage exploration of design spaces that were previously impractical to fully assess. This capability is especially relevant in fields where mechanical performance must be balanced with thermal, vibrational, and integration constraints — such as in accelerator technologies, space systems, superconducting generators or motors, and high-energy physics experiments.

Finally, the thesis demonstrates the value of tightly coupling the model, optimization, and validation which is a workflow that aligns with current trends in digital twin development. By implementing performance evaluation and sensitivity analysis directly into the design loop, the methods developed here offer a foundation for more agile, iterative designs.

Results of this thesis has contributed considerably to one of the milestones (M7.2) of the Horizon2020 European project Heavy Ion Therapy Research Integration plus (HITRI*plus*),

by proposing the supporting system designed and reported in this thesis as baseline for the carbon-ion gantry mechanical design and integration. This thesis has been used to analyzed the impact of the mechanical solutions proposed on the optimization of the beam optics layout aiming at correcting the random errors calculated in the sensitivity studies presented in the thesis. Notable results for the gantry study case are:

1. Solution 8S for the applicative case of the rotating gantry, incorporating CFRP supports, outperforms Ti6Al4V solution 6S in metrics such as accuracy performances under load during the rotation of the machine, heat-flux through supports, sensitivity to variations of input parameters, and performance during transportation/handling phases, in case automation is not considered, while 6S retains potential advantages in automated systems due to its simpler architecture, tunability and reduced stress state induced in the cryogenic device.
2. Solutions 6S and 8S have been proven compliant to beam requirements by beam tracking ensuring the efficacy of correcting errors related to deformations and manufacturing tolerances without major beam losses.

While this thesis presents a validated modeling, some limitations must be acknowledged:

1. The developed LPMs are applicable to a specific class of supporting architectures that employ only rods connected through spherical or universal joints. Nonetheless, this architectural class is among the most commonly adopted, as highlighted in the literature review. This limits the applicability of the models in configurations where the supports are connected through joint types that introduce significant rotational constraints.
2. The modeling approach assumes the absence of friction. However, this can be solved already by introducing a more complete model.
3. The validation of the models has been conducted primarily through numerical comparison with FEA. While the agreement is strong, experimental validation through physical prototyping and testing must be foreseen. Real-world boundary conditions, assembly tolerances, and material imperfections may affect the performance in ways that may differ from the current hypothesis.

These limitations define the current boundaries of the proposed methodology and provide motivation for future developments which may include:

1. The extension of the proposed LPMs to supporting systems that utilize supports other than linking rods (joined solely by universal and spherical joints) by including the contribution of bending and torsion in the response of the system. This extension can be used to simulate the impact of friction, modeling it as additional torsional or bending stiffness.
2. The integration of the calculation of the natural frequencies of the system enabling the introduction of fitness functions to fine-tune the system's frequency response during optimization with the genetic algorithm.

3. The study of the stress-state on the cryogenic device generated by the over-constrained system.
4. The completion of the validation process, although the LPMs have already been deemed as reliable as FEAs, through a prototyping and testing campaign.

The most relevant outcome of this thesis is, therefore, the novel mathematical model developed for rod supporting systems applied to cryogenic devices. It combines simplicity in terms of the number of relevant parameters with low computational cost and high accuracy compared to standard FEAs. These advantages make it accessible to a wider community than just experienced Finite Element analysts, providing useful insights into possible ways of optimizing the supporting system.

Appendix A
Parallel mechanism kinematics

The IPK and DPK for the kind of parallel mechanism used in this study are reported in [98]. In this appendix, both IPK and DPK are partially reported according to these authors formalism to be consistent through the text. Additionally, this shows how the kinematics in [98] is not constrained to the geometry showed in the original article but can be applied to more complex geometries too.

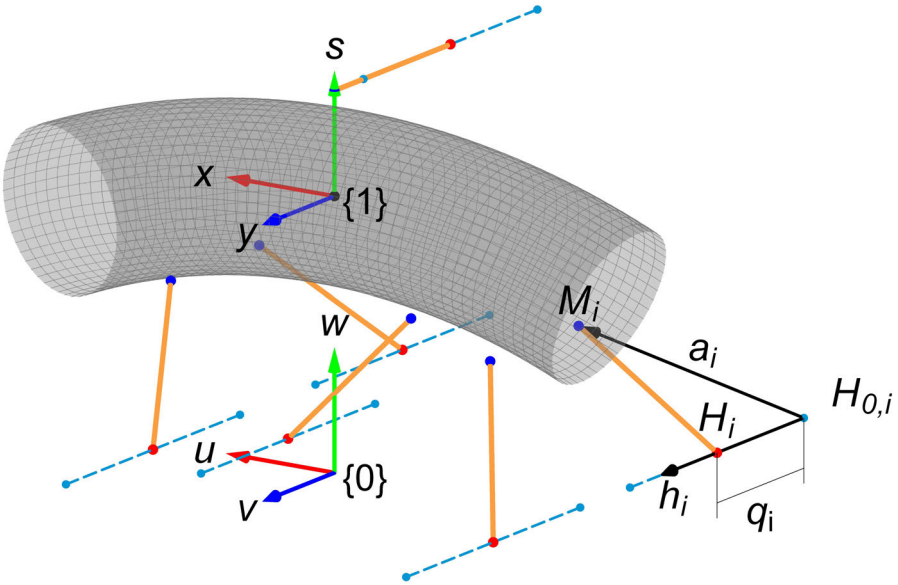

Figure A.1: *Kinematic scheme of the cold-warm supporting system. In the picture example the envelope of the iron yoke of a SC dipole is represented in gray and the six supporting rods in orange.*

Figure A.1 illustrate the kinematic of the cold-warm support system, in the example picture the body supported colored in gray is one of the SC dipoles while the six supports are colored in orange. Two reference frames are defined, the master frame $\{0\}$ fixed in the environment and the local frame $\{1\}$ fixed to the supported body. One end of each rod C_i is connected to the cold-mass while the other end H_i stands on prismatic joint (1D translation in azure) which is anchored to the vacuum vessel of the cold-mass. The prismatic joints represented in Figure A.1 are in such position only to better schematize the problem.

A.1 Inverse Position Kinematics

The position of the warm joint of the i-th supporting rod ${}^{0}\mathbf{H}_i$ in the master frame $\{0\}$ is described by:

$$ {}^{0}\mathbf{H}_i = \mathbf{H}_{0,i} + q_i \mathbf{h}_i \tag{A.1} $$

where $\mathbf{H}_{0,i}$ is the position of the local frame of the i-th prismatic joint, $\mathbf{h}_i$ its orientation given as a unit vector and q_i is the parameter that describe the position of the warm joint in the one-dimensional local frame of the prismatic joint. Both $\mathbf{H}_{0,i}$ and $\mathbf{h}_i$ are expressed with respect to $\{0\}$.

The IPK requires a system of eight equations to be solved, the first six represent the constrain of rigid body for each rod:

$$ E_i : \; e_i = 0 \quad \text{with:} \quad e_i = \| {}^{0}\mathbf{M}_i - {}^{0}\mathbf{H}_i \|^2 - L_i^2 \tag{A.2} $$

where ${}^{0}\mathbf{M}_i$ is the position of the cold joint of the i-th rod on the cold-mass and L_i is the length of the i-th support. ${}^{0}\mathbf{M}_i$ is not known beforehand but can be found by applying the so called transformation matrix ${}^{0}_{1}\mathbf{T}$ to ${}^{1}\mathbf{M}_i$. The remaining two equations can be seen in [98] and complete the system of equations for the mechanism:

$$ \{E_1 \,;\, E_2 \,;\, E_3 \,;\, E_4 \,;\, E_5 \,;\, E_6 \,;\, S \,;\, N\} \tag{A.3} $$

A generic affine transformation between two reference frames $\{m\}$ and $\{l\}$ can be expressed by the affine transformation matrix:

$$ {}^{m}_{l}\mathbf{T} = \begin{bmatrix} {}^{m}_{l}\mathbf{R} & {}^{m}\mathbf{p}_l \\ \mathbf{0}_{1\times 3} & 1 \end{bmatrix} \tag{A.4} $$

where ${}^{m}_{l}\mathbf{R} = \mathbf{R}_k \mathbf{R}_j \mathbf{R}_i$ is a general rotation matrix between the frames S_l and S_m composed by the three rotation matrices about each axis of the reference system $\left\{\hat{i}_m, \hat{j}_m, \hat{k}_m\right\}$. The column vector ${}^{m}\mathbf{p}_l$ is the position of the frame $\{l\}$ expressed in the $\{m\}$ coordinates and $\mathbf{0}_{1\times 3}$ is a 1×3 row vector containing zeros.

Applying the transformation matrix ${}^{m}_{l}\mathbf{T}$ to a position expressed in the $\{l\}$ frame ${}^{l}\mathbf{P}$ gives as result the position with respect to the $\{m\}$ frame ${}^{m}\mathbf{P}$:

$$ \begin{bmatrix} {}^{m}\mathbf{P} \\ 1 \end{bmatrix} = {}^{m}_{l}\mathbf{T} \begin{bmatrix} {}^{l}\mathbf{P} \\ 1 \end{bmatrix} \tag{A.5} $$

${}^{1}\mathbf{M}_i$ is purely related to geometric data of the magnet mechanical design and the choice of the position of $\{1\}$, that in this work is on the beam design orbit at half the magnetic length the optic element. The matrix ${}^{0}_{1}\mathbf{T}$ is also defined by arbitrary choices while defining the position ${}^{0}\mathbf{p}_1$ of $\{1\}$ with respect to $\{0\}$ and their reciprocal orientation contained in the rotation matrix ${}^{0}_{1}\mathbf{R}$.

The transformation matrix ${}^{0}_{1}\mathbf{T}$ can be parameterized as showed in [98].

The IPK solutions for each rod are given by:

$$ q_{i_{1,2}} = \mathbf{h}_i^T \mathbf{a}_i \pm \sqrt{\left(\mathbf{h}_i^T \mathbf{a}_i\right)^2 - \mathbf{a}_i^T \mathbf{a}_i + L_i^2} \tag{A.6} $$

where $\mathbf{a}_i$ can be visualized as the vector that goes from the origin of the prismatic joint $\mathbf{H}_{0,i}$ to the cold joint ${}^0\mathbf{M}_i$ of each support, and written explicitly is:

$$\begin{bmatrix}\mathbf{a}_i\\1\end{bmatrix} = {}^0_1\mathbf{T}\begin{bmatrix}{}^1\mathbf{M}_i\\1\end{bmatrix} - \begin{bmatrix}\mathbf{H}_{0,i}\\1\end{bmatrix} \tag{A.7}$$

To summarize, the IPK calculation routine takes the following inputs:

- Geometric data of the design magnet mechanical design ${}^1\mathbf{M}_i$,
- geometric data of the position $\mathbf{H}_{0,i}$ and orientation $\mathbf{h}_i$ of the prismatic joints,
- data about the position and orientation of the moving end-object, stored in ${}^0_1\mathbf{T}$.

to give the configuration of the supporting rods that allow the end-object to be in such pose. As written in Equation A.6 each rod comes with two possible solutions that combined for all six rods give a total of $2^6 = 64$ solutions.

A.2 Direct Position Kinematics

The solution of the DPK is not analytical as the one of the IPK: it requires therefore the implementation of a numerical method. The algorithm implemented has been taken from [98] and it is here reported for completeness and adapted to be coherent with this work.

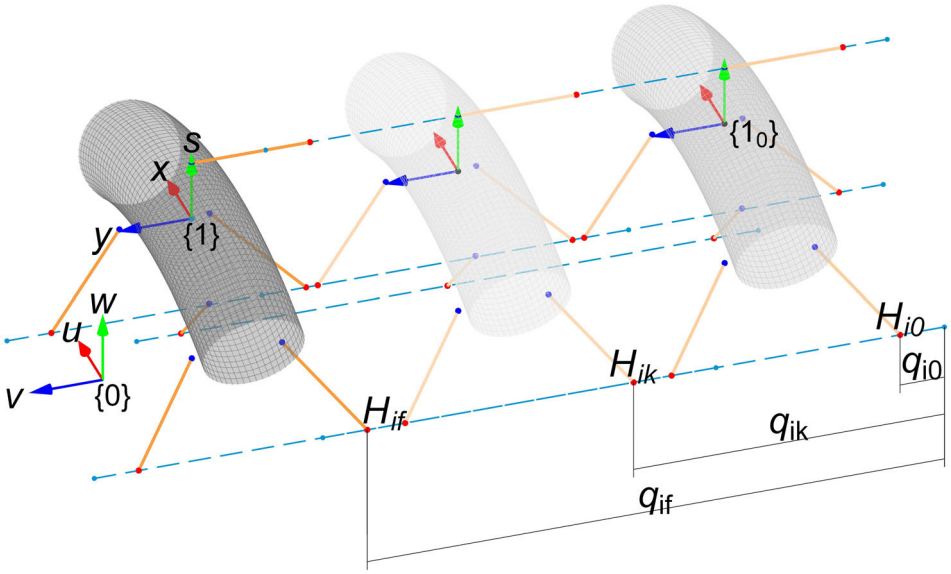

Figure A.2: *Visualization of the steps of the algorithm solving the DPK for the kinematic model of the support system. A simplified initial pose* $\{1_0\}$ *allows to visualize here a simpler version of the solution of the DPK that would require only a translation to obtain the output pose of* $\{1\}$.

The algorithm follows the following steps:

1. With reference to Figure A.2, an initial pose of the body, represented by the local reference system $\{1_0\}$, is arbitrarily given by the matrix ${}^0_1\mathbf{T}_0$. For example, composed by the rotation matrix ${}^0_1\mathbf{R}_0 \equiv \mathbf{I}_{3\times3}$ and an arbitrary position vector ${}^0\mathbf{p}_{1_0}$.
2. The initial joint vector $\mathbf{q}_0 = (q_{01}, \ldots, q_{06})^T$ is calculated solving the IPK for the initial pose ${}^0_1\mathbf{T}_0$. Note that $\mathbf{q}_0$ is not a unique solution for the IPK (it is one in 64). However, supposing as fixed for this application the final configuration of the supports i.e. the rod on top of the magnet in Figure A.2 will always be on the right by design. A set of six conditions as the aforementioned define then uniquely $\mathbf{q}_0$ among the 64 solutions.
3. A discrete sequence of joint vectors $(\mathbf{q}_0, \ldots, \mathbf{q}_k, \ldots, \mathbf{q}_f)$ is defined by means of a linear interpolation. Where $\mathbf{q}_f$ is the input joint vector related to the position of the warm joints for which one is solving the DPK.
4. An iterative Newton-Rhapson algorithm is used to find the vector $\mathbf{x}_k$ that verifies the system of equations in A.3 within a given arbitrarily small tolerance δ. (i.e. for Equation A.2 it can be asked that $e_i(\mathbf{x}_l) < \delta$). The iterative process, regulated by the index l, starts by taking as a first guess the previous solution $\mathbf{x}_{k-1}$. For each l-step a new estimate for the solution at the k-step is found by:

$$\mathbf{x}_{l+1} = \mathbf{x}_l - \mathbf{J}_l^{-1}\mathbf{V}_l \tag{A.8}$$

where $\mathbf{V}_l$ and $\mathbf{J}_l$ are:

$$\mathbf{V}_l = \begin{bmatrix} \|{}^0\mathbf{M}_1(\mathbf{x}_l) - {}^0\mathbf{H}_1(\mathbf{s}_k)\| - L_1 \\ \vdots \\ \|{}^0\mathbf{M}_6(\mathbf{x}_l) - {}^0\mathbf{H}_6(\mathbf{s}_k)\| - L_6 \\ s(\mathbf{x}_l) \\ n(\mathbf{x}_l) \end{bmatrix} \quad \text{and}$$

$$\mathbf{J}_l = \begin{bmatrix} \frac{\partial e_1}{\partial x_0} & \cdots & \frac{\partial e_1}{\partial y_3} \\ \vdots & \ddots & \vdots \\ \frac{\partial e_6}{\partial x_0} & \cdots & \frac{\partial e_6}{\partial y_3} \\ \frac{\partial s}{\partial x_0} & \cdots & \frac{\partial s}{\partial y_3} \\ \frac{\partial n}{\partial x_0} & \cdots & \frac{\partial n}{\partial y_3} \end{bmatrix} \tag{A.9}$$

note that the partial derivatives contained in the Jacobian $\mathbf{J}_l$ must be evaluated for $\mathbf{x}_l$ and $\mathbf{q}_k$.
5. The point four is repeated until $\mathbf{q}_k = \mathbf{q}_f$ giving as result the vector $\mathbf{x}$ associated to the transformation matrix ${}^0_1\mathbf{T}$

Appendix B
Information transfer from mechanics to beam optics

This appendix has been written in collaboration with Enrico Felcini from CNAO

B.1 Recap of MAD manuals

In MADX (and previously in MAD8) [113, 114], magnet misalignments are referred to the local reference system. The local reference system is defined as a local curvilinear right handed coordinate system (x,y,s). The s–axis is the longitudinal axis, locally tangent to the arc sections. The two other axes are perpendicular to the s–axis; they are labelled x (in the bend plane) and y (perpendicular to the bend plane), as represented in Figure B.1.

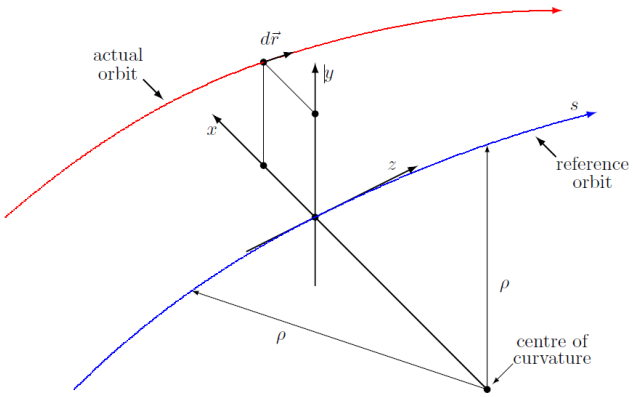

Figure B.1: *Local reference system used in MADx. Fig. from ref. [113]*

As reported in the MADx user and MAD8 physics manuals, misalignments are defined as displacements along the three coordinate axes, and rotations about the coordinate axes. The *misalignment pivot*, i.e. **the point around which the rotation takes place is the origin of the local reference system at the element entrance**. The effect of misalignments is treated in a linear approximation.

Therefore, any magnet misalignment is represented by the three translational components as:

$$\mathbf{V} = \begin{pmatrix} \Delta x \\ \Delta y \\ \Delta s \end{pmatrix} \tag{B.1}$$

and by the rotation angles about the three axis of the local reference system:

$$\mathbf{R} = \begin{pmatrix} \phi \\ \theta \\ \psi \end{pmatrix} \tag{B.2}$$

The code treats the rotation angles as follows:

$$\begin{aligned} \mathbf{W} &= \begin{pmatrix} w_{11} & w_{12} & w_{13} \\ w_{21} & w_{22} & w_{23} \\ w_{31} & w_{32} & w_{33} \end{pmatrix} = \\ &= \begin{pmatrix} +\cos\theta\cos\psi - \sin\theta\sin\phi\sin\psi & -\cos\theta\sin\psi - \sin\theta\sin\phi\cos\psi & \sin\theta\cos\phi \\ \cos\phi\sin\psi & \cos\phi\cos\psi & \sin\phi \\ -\sin\theta\cos\psi - \cos\theta\sin\phi\sin\psi & +sin\theta\sin\psi - \cos\theta\sin\phi\sin\psi & \cos\theta\cos\phi \end{pmatrix} = \\ &= \boldsymbol{\Theta}\ \boldsymbol{\Phi}\ \boldsymbol{\Psi} \end{aligned} \tag{B.3}$$

where

$$\boldsymbol{\Theta} = \begin{pmatrix} \cos\theta & 0 & \sin\theta \\ 0 & 1 & 0 \\ -\sin\theta & 0 & \cos\theta \end{pmatrix}, \quad \boldsymbol{\Phi} = \begin{pmatrix} 1 & 0 & 0 \\ 0 & \cos\phi & \sin\phi \\ 0 & -\sin\phi & \cos\phi \end{pmatrix}, \quad \boldsymbol{\Psi} = \begin{pmatrix} \cos\psi & -\sin\psi & 0 \\ \sin\psi & \cos\psi & 0 \\ 0 & 0 & 1 \end{pmatrix} \tag{B.4}$$

For the considered order of matrix multiplication and sign convention for the angles:

- θ is the rotation around the y–axis; it follows the right hand rule (Figure B.2);
- ϕ is the rotation around the x–axis; **it does not follow the right hand rule**; a positive angle gives a greater y–coordinate at the exit than at the entry (Figure B.3);
- ψ is the rotation around the s–axis; it follows the right hand rule (Figure B.4).

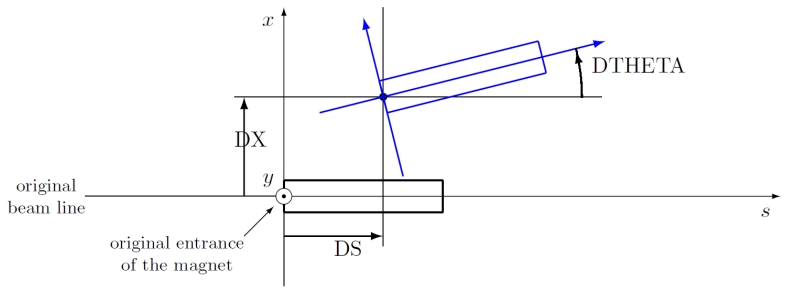

Figure B.2: *Alignment errors in the (x, s)–plane: θ angle.*

Any rotation matrix (i.e. a 3×3 matrix with unitary determinant and with all elements being real and in the range $[-1:1]$) in 3D space can be obtained by the multiplication of the three basic rotation matrices (see B.4). Matrix multiplication does not profit from the

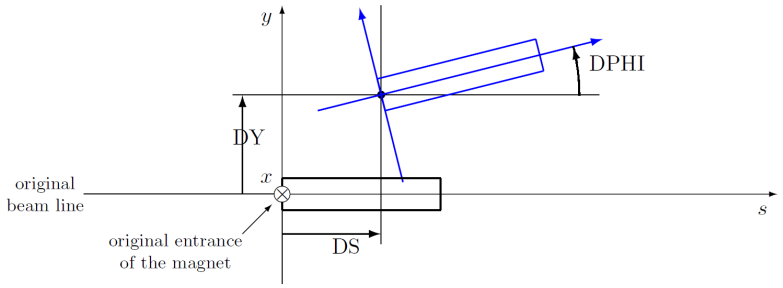

Figure B.3: *Alignment errors in the (y, s)–plane: ϕ angle. The rotation angle ϕ does not follow the right hand rule*

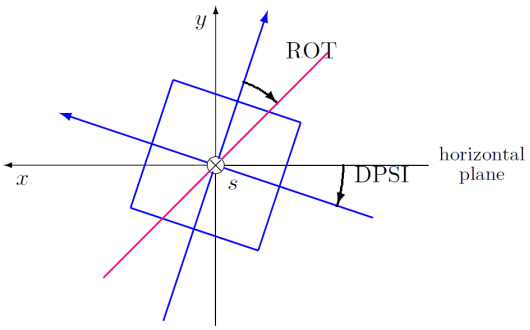

Figure B.4: *Alignment errors in the (x, y)–plane: ψ angle.*

commutative property; as a consequence, there are eight different ways of representing the same rotation matrix, each with a specific tripod of angles. To determine the correct rotation angles from any given rotation matrix W (B.3) for later use in MADx, it is of uppermost importance to follow the MADx convention for the rotation angle (see B.4) and the MADx multiplication order, see (B.3). The appropriate rotation angles can be calculated as:

$$\begin{aligned} \theta &= \arctan \frac{w_{13}}{w_{33}}, \\ \psi &= \arctan \frac{w_{21}}{w_{22}}, \\ \phi &= \begin{cases} \arctan \frac{w_{23}}{w_{22}} / \cos\psi, & \text{if } \psi = 0 \text{ or } \psi = \pi \\ \arctan \frac{w_{23}}{w_{21}} / \sin\psi, & \text{otherwise} \end{cases} \end{aligned} \tag{B.5}$$

B.2 Recap Mechanics

B.2.1 Conventions for dipoles two, three and four

Each dipole has a local system defined as in Figure B.5. To simplify mechanical calculations, local systems viewed from a fixed reference system follow the convention

illustrated in Figure B.7. The misalignment is expressed as an affine transformation matrix between the nominal local system and the real local system (Figure B.6), as defined by equation (B.6). The rotation matrix ${}^{2}_{3}\mathbf{R}$ inside the affine transformation matrix is defined by three positive rotations along each axis, where a rotation is positive if it follows the right hand rule. The order of multiplication of the three rotation matrices is expressed by equation (B.7). Note that ${}^{2}_{3}\mathbf{T}$ is the output of the routine described in Section A.2.

$$ {}^{2}_{3}\mathbf{T} = \begin{bmatrix} {}^{2}_{3}\mathbf{R} & {}^{2}\mathbf{p}_{3} \\ \mathbf{0}_{1\times3} & 1 \end{bmatrix} = \begin{bmatrix} & & dx \\ & \mathbf{R}_z\mathbf{R}_y\mathbf{R}_x & dy \\ & & dz \\ \mathbf{0}_{1\times3} & & 1 \end{bmatrix} \tag{B.6} $$

$$ {}^{2}_{3}\mathbf{R} = \mathbf{R}_z\mathbf{R}_y\mathbf{R}_x = \begin{bmatrix} \cos\delta_z & -\sin\delta_z & 0 \\ \sin\delta_z & \cos\delta_z & 0 \\ 0 & 0 & 1 \end{bmatrix} \begin{bmatrix} \cos\delta_y & 0 & \sin\delta_y \\ 0 & 1 & 0 \\ -\sin\delta_y & 0 & \cos\delta_y \end{bmatrix} \begin{bmatrix} 1 & 0 & 0 \\ 0 & \cos\delta_x & -\sin\delta_x \\ 0 & \sin\delta_x & \cos\delta_x \end{bmatrix} \tag{B.7} $$

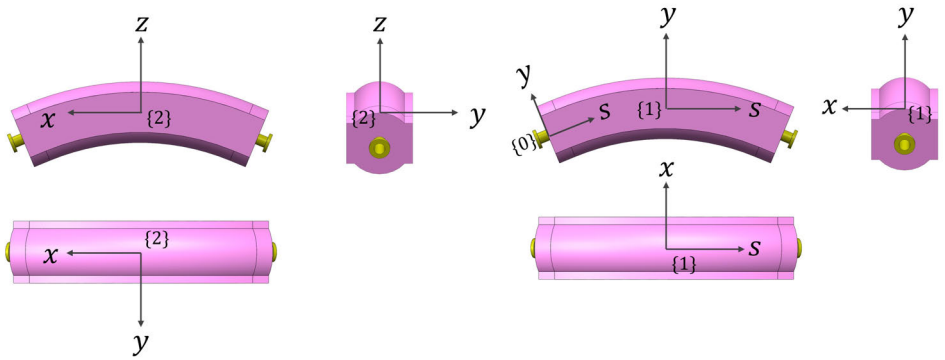

Figure B.5: *Nominal reference systems used in the misalignment evaluation. Where* {0} *is the local system at the entry of the magnet with the axes convention of MADx (illustrated only on the y-s plane for simplicity);* {1} *is the local system at the middle point of the magnet (on the design orbit), this also follows MADx axes convention;* {2} *is the local system used for mechanical calculations.* ***This picture is coherent with dipole two, three and four, enumerated following the beam from the entry of the gantry to the isocentre. The convention for dipole one is schematized in Figure B.8.***

Information needed for MADx that are stored in the vector $\mathbf{V}$ (B.1) and the rotation matrix $\mathbf{W}$ (B.3) can be combined in the affine transformation matrix ${}^{0}_{5}\mathbf{T}$ as follows:

$$ {}^{0}_{5}\mathbf{T} = \begin{bmatrix} & & \Delta x \\ & \mathbf{W} & \Delta y \\ & & \Delta s \\ \mathbf{0}_{1\times3} & & 1 \end{bmatrix} \tag{B.8} $$

The matrix ${}^{0}_{5}\mathbf{T}$ can also be expressed as the multiplication of affine matrices for each

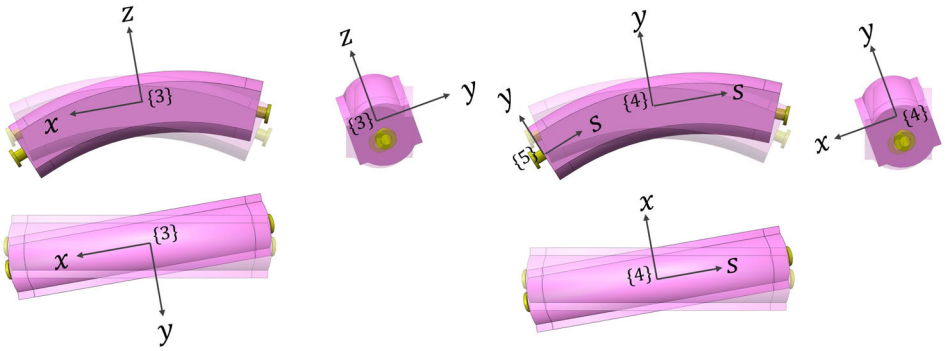

Figure B.6: *Real reference systems for a misaligned dipole. Where* {5} *is the local system at the entry of the magnet with the axes convention of MADx (illustrated only on the y-s plane for simplicity);* {4} *is the local system at the middle point of the magnet (on the design orbit), this also follows MADx axes convention;* {3} *is the local system used for mechanical calculations.* ***This picture is coherent with dipole two, three and four, enumerated following the beam from the entry of the gantry to the isocentre. The convention for dipole one is similar to the one schematized in Figure B.8 for nominal reference systems.***

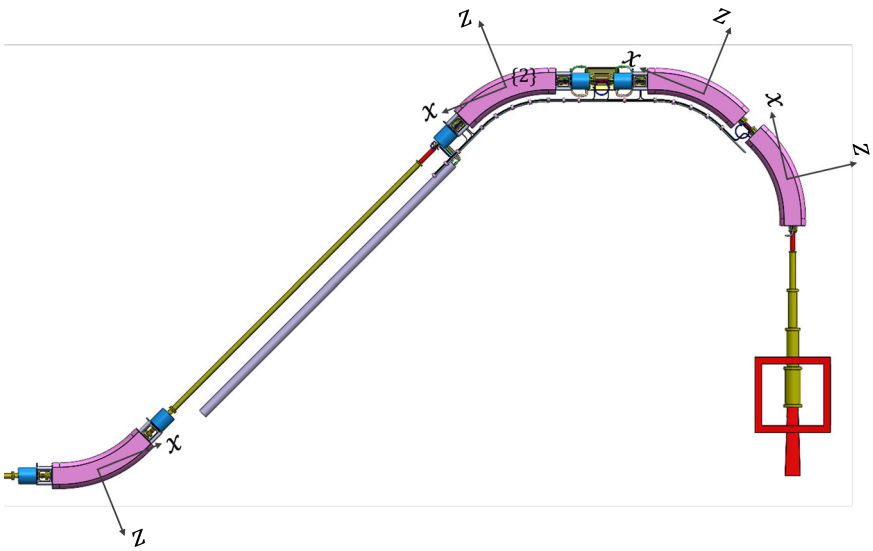

Figure B.7: *Dipoles local systems in the assembly. Dipoles are numbered from one to four following the path of a particle from the entry in the gantry to the isocentre.*

reference system transformation:

$$ {}^{0}_{5}\mathbf{T} = {}^{0}_{1}\mathbf{T}\ {}^{1}_{2}\mathbf{T}\ {}^{2}_{3}\mathbf{T}\ {}^{3}_{4}\mathbf{T}\ {}^{4}_{5}\mathbf{T} \tag{B.9} $$

The matrix ${}^{0}_{1}\mathbf{T}$ can be expressed as the inverse of the opposite transformation for

simplicity: ${}^{0}_{1}\mathbf{T} = ({}^{1}_{0}\mathbf{T})^{-1}$. With reference to Figure B.5, ${}^{1}_{0}\mathbf{T}$ gives how a vector in the frame $\{0\}$ is transformed in frame $\{1\}$, therefore is related to a rotation of $-\pi/8$ around the x axis and translations of $(0, \rho\cos\pi/8 - \rho, -\rho\sin\pi/8)$, giving:

$$ {}^{1}_{0}\mathbf{T} = \begin{bmatrix} 1 & 0 & 0 & 0 \\ 0 & \cos(-\pi/8) & -\sin(-\pi/8) & \rho\cos(\pi/8) - \rho \\ 0 & \sin(-\pi/8) & \cos(-\pi/8) & -\rho\sin(\pi/8) \\ 0 & 0 & 0 & 1 \end{bmatrix} \tag{B.10} $$

The matrix ${}^{1}_{2}\mathbf{T}$ is equal to:

$$ {}^{1}_{2}\mathbf{T} = \begin{bmatrix} 0 & -1 & 0 & 0 \\ 0 & 0 & 1 & 0 \\ -1 & 0 & 0 & 0 \\ 0 & 0 & 0 & 1 \end{bmatrix} \tag{B.11} $$

B.2.2 Conventions for dipole one

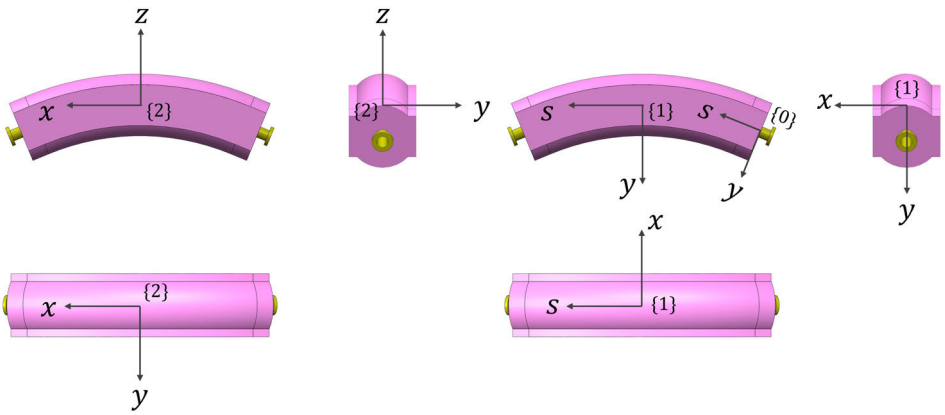

Figure B.8: *Nominal reference systems used in the misalignment evaluation for dipole one.*

With reference to Figure B.8, the matrix ${}^{1}_{0}\mathbf{T}$ contains a rotation of $\pi/8$ around the x axis and translations of $(0, \rho - \rho\cos(\pi/8), -\rho\sin\pi/8)$, giving:

$$ {}^{1}_{0}\mathbf{T} = \begin{bmatrix} 1 & 0 & 0 & 0 \\ 0 & \cos(\pi/8) & -\sin(\pi/8) & \rho - \rho\cos(\pi/8) \\ 0 & \sin(\pi/8) & \cos(\pi/8) & -\rho\sin(\pi/8) \\ 0 & 0 & 0 & 1 \end{bmatrix} \tag{B.12} $$

With reference to Figure B.8, the matrix ${}^{1}_{2}\mathbf{T}$ is equal to:

$$ {}^{1}_{2}\mathbf{T} = \begin{bmatrix} 0 & -1 & 0 & 0 \\ 0 & 0 & -1 & 0 \\ 1 & 0 & 0 & 0 \\ 0 & 0 & 0 & 1 \end{bmatrix} \tag{B.13} $$

Since, ${}^{3}_{4}\mathbf{T} = ({}^{1}_{2}\mathbf{T})^{-1}$ and ${}^{4}_{5}\mathbf{T} = ({}^{0}_{1}\mathbf{T})^{-1} = {}^{1}_{0}\mathbf{T}$ the equation (B.9) can be generally rewritten as:

$$ {}^{0}_{5}\mathbf{T} = ({}^{1}_{0}\mathbf{T})^{-1}\ {}^{1}_{2}\mathbf{T}\ {}^{2}_{3}\mathbf{T}\ ({}^{1}_{2}\mathbf{T})^{-1}\ {}^{1}_{0}\mathbf{T} \tag{B.14} $$

where equations (B.10) and (B.11) are substituted when calculating dipoles two, three and four, while equations (B.12) and (B.13) are used for dipole one instead.

Appendix C
Code example for the over-constrained LPM

An example of the code programmed in Wolfram Mathematica 13.0 is given below. This code provides only a basic example of the implementation of the code to obtain the axial loads on each support and displacements of the suspended object given the external loads $(F_x, F_y, F_z, M_x, M_y, M_z)$, the pre-load δ_P in mm. The matrices governing the deformation of the vacuum vessel D_{cm}, D_{ow}, D_v appear as variables and their calculation is explained in Section 5.1. The calculation of the thermal contraction δ is left to the reader following Equation 5.28.

```
(*number of tie rods*)
n = 11;
(*example of a 11 tie-rods geometry*)
geometry = {{{-184.1, 48.4, -87.5}, {-112.6, 173.4, -129.4}}, {{267.9, -75.8, 65.2},
    {260.2, -224.6, 82.6}}, {{108.9, 4.1, 99.9}, {178.8, 59.9, 220.3}}, {{387.2, 83.2,
    55.4}, {346.6, 124., 193.9}}, {{-360.8, 98.1, 19.5}, {-296., 138.5, 148.6}}, {{-48.5,
     -57.4, 81.9}, {60.7, -113.5, 168.1}}, {{-254.7, -67.7, 73.6}, {-234.6, -51.9,
    221.4}}, {{-155.7, -56.8, -82.3}, {-243.1, -178.2, -93.5}}, {{147.,95.7, -29.},
    {173.2, 239.3, 5.5}}, {{-361.4, 5.9, -99.8}, {-294., 68.1, -218.5}}, {{38.5, 77.,
    63.8}, {-58.1, 145.7, 155.8}}}
(*geometry of the compatible structure*)
ISOgeometry = Drop[geometry, -(n-6)];
directionM = Table[Normalize[Geometry[[i, 2]] - Geometry[[i, 1]]], {i, 1, n}];
(*input external forces components*)
Fs = {Fx, Fy, Fz, Mx, My, Mz};
(*calculates the forces for each support in the compatible structure*)
N0 = Join[Transpose[J[ISOgeometry]].Fs, ConstantArray[0, n - 6]];
(*calculates w_i*)
w = Table[Normalize[geometry[[i]][[2]] - geometry[[i]][[1]]], {i, 7, n}];
(*calculates u_i*)
u = Table[Cross[geometry[[i]][[1]], Normalize[geometry[[i]][[2]] - geometry[[i]][[1]]]],
    {i, 7, n}];
Fm = Join[#[[1]], #[[2]]] & /@ Transpose[{w, u}];
(*support internal actions due to application of unitary loads due to over-constrain
    variables*)
NXm = Table[Join[Transpose[J[ISOgeometry]].Fm[[i]], IdentityMatrix[n-6][[i]]], {i, 1, n
    -6}];
(*over-constrain variables*)
X = {X1, X2, X3, X4, X5};
(*Equation 2*)
eq = Table[Nv[[j]].(N0 + X.NXm + δ RodStiffness - δP) == RodStiffness*Table[(Dcm.(N0 + X.
    NXm))[[i]].directionM[[i]], {i, 1, n}].NXm[[j]] + RodStiffness*Table[(Dow.{Cos[ang],
    Sin[ang]})[[i]].directionM[[i]], {i, 1, n}].NXm[[j]] + RodStiffness*Table[Dv[[i]].
    directionM[[i]], {i, 1, n}].NXm[[j]], {j, 1, n-6}];
```

```
(*solves the system of equations calculating the over-constrain variables*)
sol = NSolve[eq, X];
localX = X /. sol[[1]];
(*calculates internal actions on the real structure*)
forces = N0 + localX.NXm;
(*calculates disaplacements of the supported device Equation 13*)
displcement = Table[1/RodStiffness*Join[Transpose[J[ISOgeometry]].IdentityMatrix[6][[j]],
     ConstantArray[0, n-6]].(N0 + localX.NXm + δ RodStiffness - δP) - Join[Transpose[J[
    ISOgeometry]].IdentityMatrix[6][[j]], ConstantArray[0, n-6]].Table[(Dcm.(N0 + localX.
    NXm)[[i]].directionM[[i]], {i, 1, n}] - Join[Transpose[J[ISOgeometry]].IdentityMatrix
    [6][[j]], ConstantArray[0, n-6]].Table[(Dow.{Cos[ang], Sin[ang]})[[i]].directionM[[i
    ]], {i, 1, n}] - Join[Transpose[J[ISOgeometry]].IdentityMatrix[6][[j]], ConstantArray
    [0, n-6]].Table[Dv[[i]].directionM[[i]], {i, 1, n}], {j, 1, 6}];
```

Appendix D
Pose results after optimization

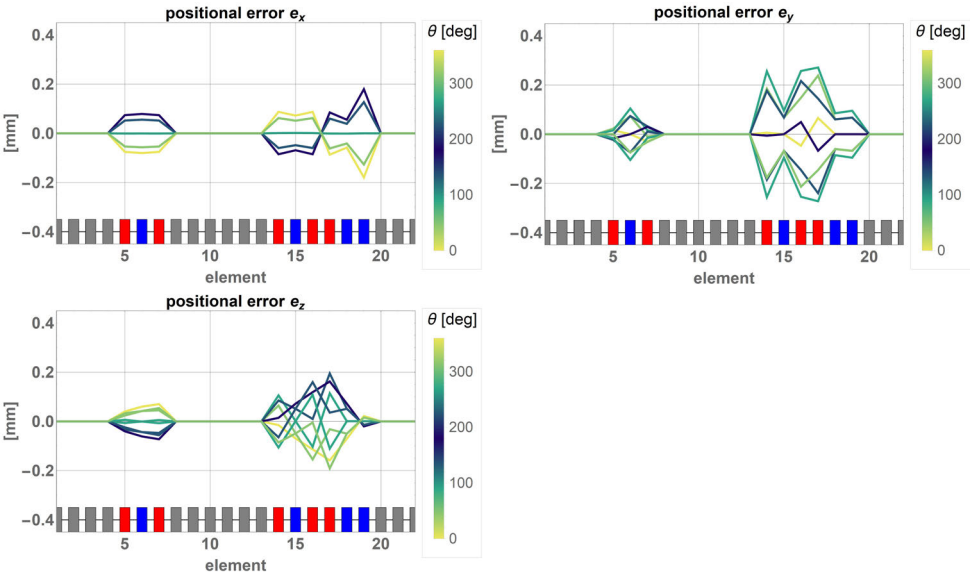

Figure D.1: *Displacement of the elements of the gantry beam line during rotation with supporting systems of the 4 dipoles as initially designed.*

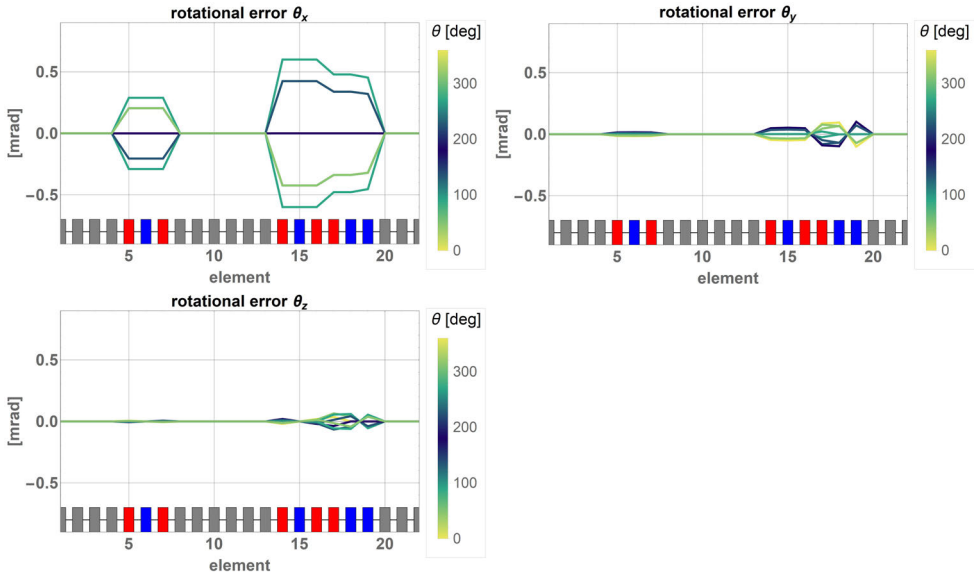

Figure D.2: *Orientation of the elements of the gantry beam line during rotation with supporting systems of the 4 dipoles as initially designed.*

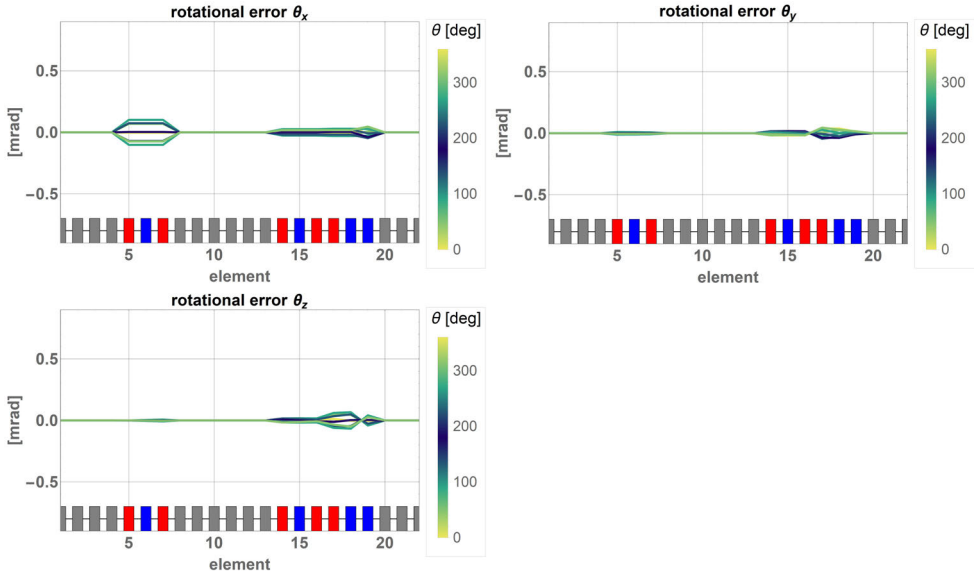

Figure D.3: *Orientation of the elements of the gantry beam line during rotation with supporting systems of the 4 dipoles as result of the optimization.*

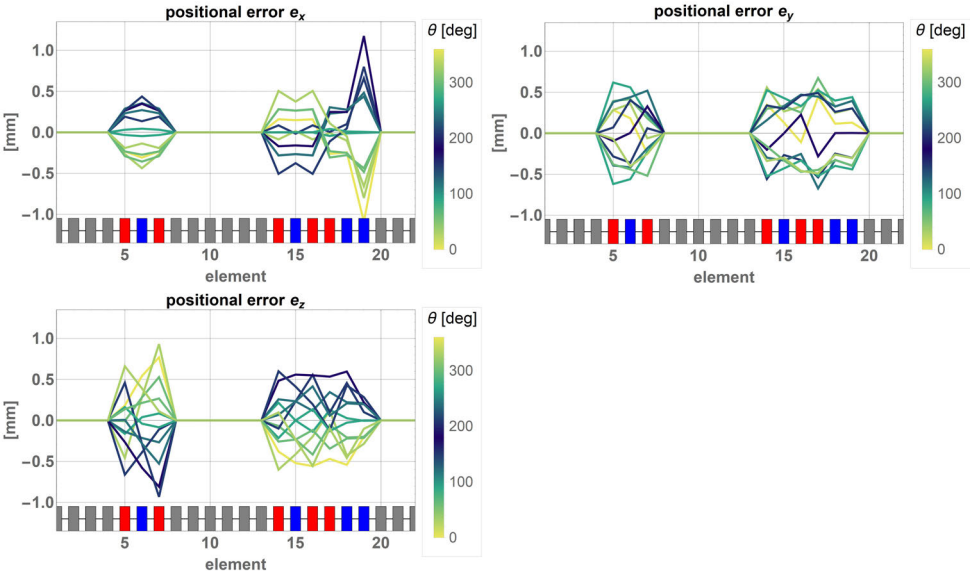

Figure D.4: *Displacement of the elements of the gantry beam line during rotation with supporting systems of the 4 dipoles subject to backlash (S3).*

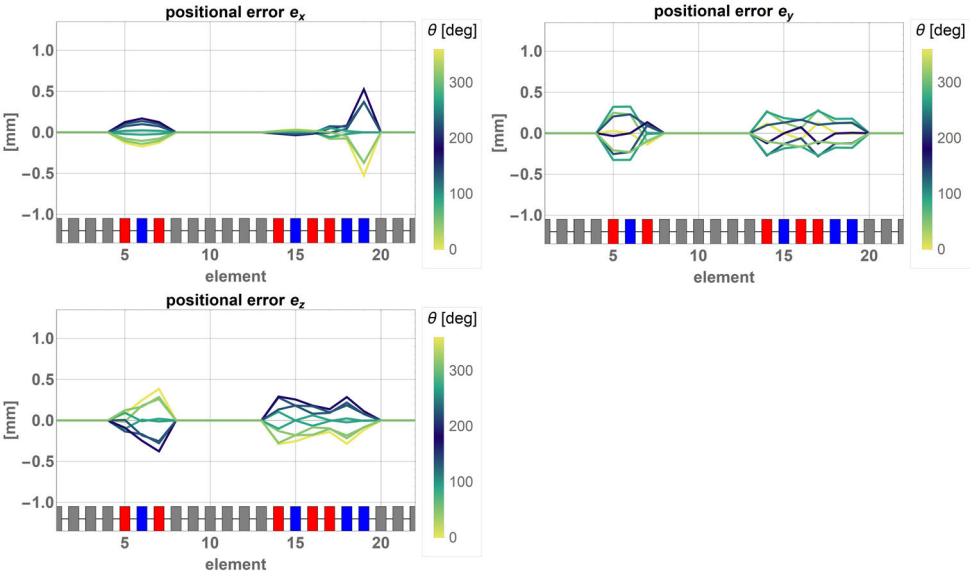

Figure D.5: *Displacement of the elements of the gantry beam line during rotation with supporting systems of the 4 dipoles with pre-load system (S4).*

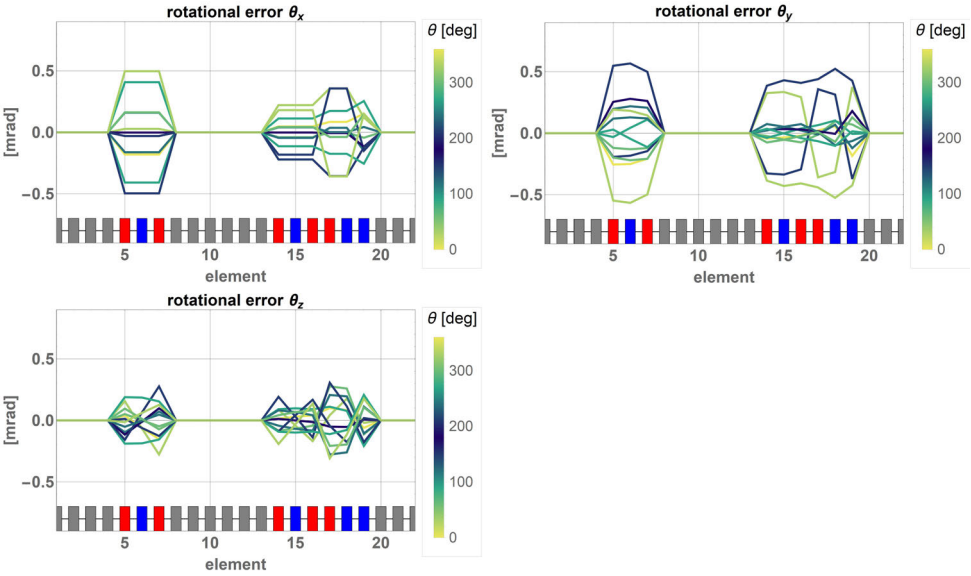

Figure D.6: *Orientation of the elements of the gantry beam line during rotation with supporting systems of the 4 dipoles subject to backlash (S3).*

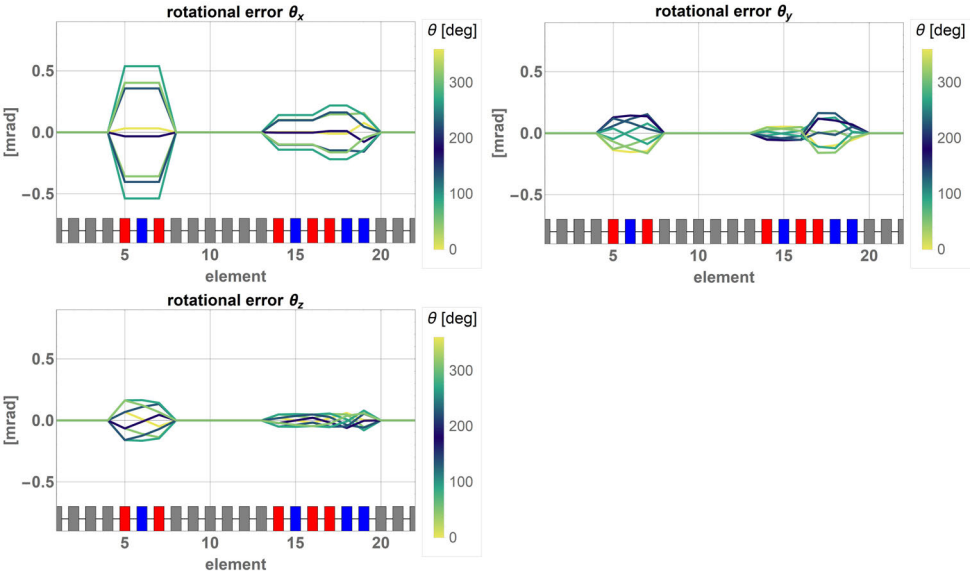

Figure D.7: *Orientation of the elements of the gantry beam line during rotation with supporting systems of the 4 dipoles with pre-load system (S4).*

Bibliography

[1] *The Top 10 Causes of Death.* World Health Organization. URL: https://www.who.int/news-room/fact-sheets/detail/the-top-10-causes-of-death (visited on 12/13/2021).

[2] Tadeusz Dyba et al. "The European cancer burden in 2020: Incidence and mortality estimates for 40 countries and 25 major cancers". In: *European Journal of Cancer* 157 (2021), pp. 308–347.

[3] *Global Cancer Observatory.* URL: https://gco.iarc.fr/today/home (visited on 08/09/2022).

[4] *Europe's Beating Cancer Plan.* European comission. URL: https://eur-lex.europa.eu/legal-content/en/TXT/?uri=COM%3A2021%3A44%3AFIN.

[5] JJ Wang, KF Lei, and F Han. "Tumor microenvironment: recent advances in various cancer treatments". In: *Eur Rev Med Pharmacol Sci* 22.12 (2018), pp. 3855–3864.

[6] Richard R Love et al. "Side effects and emotional distress during cancer chemotherapy". In: *Cancer* 63.3 (1989), pp. 604–612.

[7] Timothy D Malouff et al. "Carbon ion therapy: a modern review of an emerging technology". In: *Frontiers in oncology* 10 (2020), p. 82.

[8] K Esfahani et al. "A review of cancer immunotherapy: from the past, to the present, to the future". In: *Current Oncology* 27.s2 (2020), pp. 87–97.

[9] Wilhelm Conrad Röntgen. *Über eine neue Art von Strahlen.* BoD–Books on Demand, 2020.

[10] Nicolas Foray. "Victor Despeignes, the forgotten pioneer of radiation oncology". In: *International Journal of Radiation Oncology, Biology, Physics* 96.4 (2016), pp. 717–721.

[11] S Birkenhake and R Sauer. "Historical essentials influencing the development of radiooncology in the past 100 years". In: *Experientia* 51.7 (1995), pp. 681–685.

[12] Edmund JN Wilson. "Fifty years of synchrotrons". In: *Proceedings of the 1996 European Particle Accelerator Conference (EPAC'96).* 1996, pp. 135–139.

[13] Robert R Wilson et al. "Radiological use of fast protons". In: *Radiology* 47.5 (1946), pp. 487–491.

[14] Masahiro Endo. *Robert R. Wilson (1914–2000): the first scientist to propose particle therapy—use of particle beam for cancer treatment.* 2018.

[15] *Pathologies that can be treated.* CNAO. URL: https://fondazionecnao.it/en/hadrontherapy/what-is-hadrontherapy.

[16] *Bragg curves and peaks.* Brookhaven National Laboratory. URL: https://www.bnl.gov/nsrl/userguide/bragg-curves-and-peaks.php (visited on 12/15/2021).

[17] *Facilities in operation.* URL: https://www.ptcog.ch/index.php/facilities-in-operation (visited on 06/02/2022).

[18] Shyh-Yuan Lee. *Accelerator physics.* World Scientific Publishing Company, 2018.

[19] Dirk Van Delft and Peter Kes. "The discovery of superconductivity". In: *Physics today* 63.9 (2010), pp. 38–43.

[20] C Muehle et al. "Magnets for the heavy-ion cancer therapy accelerator facility (HICAT) for the clinic in heidelberg". In: *IEEE transactions on applied superconductivity* 14.2 (2004), pp. 461–464.

[21] W Beeckman et al. "Magnetic design improvement and construction of the large 90 bending magnet of the vertical beam delivery line of CNAO". In: *Proceedings of EPAC.* Vol. 1784. 2008.

[22] *The HITRIplus project.* 2010. URL: https://www.hitriplus.eu/ (visited on 10/23/2024).

[23] Alberto Martín-Martín et al. "Google Scholar, Web of Science, and Scopus: A systematic comparison of citations in 252 subject categories". In: *Journal of informetrics* 12.4 (2018), pp. 1160–1177.

[24] JG Weisend II. *Cryostat Design.* Springer, 2016.

[25] Kun Lu et al. "Evolution of the design of cold mass support for the ITER magnet feeder system". In: *Plasma Science and Technology* 15.2 (2013), p. 196.

[26] Yinfeng Zhu et al. "Conceptual design and analysis of cold mass support of the CS3U feeder for the ITER". In: *Plasma Science and Technology* 15.6 (2013), p. 599.

[27] Fabien Seyvet et al. "Improvement of the geometrical stability of the LHC cryodipoles when blocking the central support post". In: *Proceedings of the 2005 Particle Accelerator Conference.* IEEE. 2005, pp. 2675–2677.

[28] M Mathieu et al. "Supporting systems from 293 K to 1.9 K for the Large Hadron Collider (LHC) cryo-magnets". In: *Advances in cryogenic engineering* (1998), pp. 427–434.

[29] JH Sondericker and LJ Wolf. "Alternative concepts for structurally supporting the cold mass of a superconducting accelerator magnet". In: *Supercollider 3.* Springer, 1991, pp. 175–189.

[30] TH Nicol, RC Niemann, and JD Gonczy. "SSC magnet cryostat suspension system design". In: *Advances in Cryogenic Engineering.* Springer, 1988, pp. 227–234.

[31] Thomas Peterson et al. "LCLS-II 1.3 GHz cryomodule design-modified tesla-style cryomodule for CW operation". In: *Proc. 17th Int. Conf. RF Superconductivity (SRF'15).* 2015, pp. 1417–1421.

[32] Egbert Fischer et al. "Superconducting quadrupole module system for the sis100 synchrotron". In: *Proc. RUPAC.* 2012, pp. 143–145.

[33] JP Meier et al. “Cryo-technical design aspects of the superconducting SIS100 quadrupole doublet modules”. In: *AIP Conference Proceedings*. Vol. 1573. 1. American Institute of Physics. 2014, pp. 1519–1526.

[34] F Nunio et al. “Mechanical design of the Iseult 11.7 T whole body MRI magnet”. In: *IEEE Transactions on Applied Superconductivity* 20.3 (2010), pp. 760–763.

[35] P Vedrine et al. “Latest progress on the Iseult/INUMAC whole body 11.7 T MRI magnet”. In: *IEEE transactions on applied superconductivity* 22.3 (2011), pp. 4400804–4400804.

[36] Lankai Li et al. “Theoretical model of a cold mass strap suspension system for superconducting magnets”. In: *IEEE transactions on applied superconductivity* 21.6 (2011), pp. 3640–3645.

[37] HH Chen et al. “Design of mechanical structure and cryostat for IASW superconducting wiggler at NSRRC”. In: *2007 IEEE Particle Accelerator Conference (PAC)*. IEEE. 2007, pp. 374–376.

[38] Miao-Fu Xu et al. “Design, assembly, and pre-commissioning of cryostat for 3W1 superconducting wiggler magnet”. In: *Nuclear Science and Techniques* 31 (2020), pp. 1–15.

[39] Li Wang et al. “Design and analysis of a self-centered cold mass support for the MICE coupling magnet”. In: *IEEE transactions on applied superconductivity* 21.3 (2011), pp. 2259–2262.

[40] Yiyong Liu et al. “Design of cold mass supports for a superconducting undulator prototype at SINAP”. In: *IEEE Transactions on Applied Superconductivity* 25.3 (2014), pp. 1–4.

[41] Li Wang et al. “Development of a Test Cryostat for a Superconducting Undulator Prototype at the SSRF”. In: *IEEE Transactions on Applied Superconductivity* 31.5 (2021), pp. 1–5.

[42] G Olivier et al. “Ess cryomodules for elliptical cavities”. In: *Proceedings of the 16th International Conference on RF Superconductivity*. 2013.

[43] Christine Darve et al. “The ESS elliptical cavity cryomodules”. In: *AIP Conference Proceedings*. Vol. 1573. 1. American Institute of Physics. 2014, pp. 639–646.

[44] Denis Reynet et al. “Design of the ESS Spoke cryomodule”. In: *MOP089, SRF* (2013).

[45] Sebastien Bousson et al. “The ESS spoke cavity cryomodules”. In: *AIP Conference Proceedings*. Vol. 1573. 1. American Institute of Physics. 2014, pp. 665–672.

[46] P Duthil et al. “Design and Prototyping of the Spoke Cyromodule for ESS”. In: *HB2016, WEAM4Y01* (2016).

[47] Federico Carra et al. “Assessment of thermal loads in the CERN SPS crab cavities cryomodule1”. In: *Journal of Physics: Conference Series*. Vol. 874. 1. IOP Publishing. 2017, p. 012005.

[48] Thomas Jones et al. “Development of a Novel Supporting System for High Luminosity LHC SRF Crab Cavities”. In: *18th Int. Conf. on RF Superconductivity (SRF'17), Lanzhou, China, July 17-21, 2017*. JACOW, Geneva, Switzerland. 2018, pp. 304–308.

[49] P Azevedo. *SPL Short Cryomodule Design*. URL: https://indico.cern.ch/event/216370/contributions/441396/attachments/345704/482100/SPL_SC_Design_PAzevedo_SPLmeeting_7_12_2012.pdf (visited on 04/19/2023).

[50] V Parma et al. *Status of the Superconducting Proton Linac (SPL) cryo-module*. Tech. rep. 2014.

[51] Mauricio Lopes et al. “Mu2e transport solenoid cold-mass alignment issues”. In: *IEEE Transactions on Applied Superconductivity* 27.4 (2017), pp. 1–5.

[52] JJ Kosse et al. “Mechanical design of a superconducting demonstrator for magnetic density separation”. In: *Superconductor science and technology* 34.11 (2021), p. 115019.

[53] *ATLAS end-cap toroids: Technical Design Report*. Technical design report. ATLAS. Electronic version not available. Geneva: CERN, 1997. DOI: 10.17181/CERN.P03D.WQLV. URL: http://cds.cern.ch/record/331066.

[54] Akira Yamamoto et al. “The ATLAS central solenoid”. In: *Nuclear Instruments and Methods in Physics Research Section A: Accelerators, Spectrometers, Detectors and Associated Equipment* 584.1 (2008), pp. 53–74.

[55] A Dudarev et al. “First full-size ATLAS barrel toroid coil successfully tested up to 22 kA at 4 T”. In: *IEEE transactions on applied superconductivity* 15.2 (2005), pp. 1271–1274.

[56] Y Kadi, M A Fraser, and A Papageorgiou-Koufidou. *HIE-ISOLDE: technical design report for the energy upgrade*. Ed. by Y Kadi. CERN Yellow Reports: Monographs. Geneva: CERN, 2018. DOI: 10.23731/CYRM-2018-001. URL: http://cds.cern.ch/record/2635892.

[57] G Ambrosio et al. “Challenges and design of the transport solenoid for the Mu2e experiment at Fermilab”. In: *IEEE transactions on applied superconductivity* 24.3 (2013), pp. 1–5.

[58] D Elwyn Baynham et al. “Engineering design optimisation of the superconducting end cap toroid magnets for the ATLAS experiment at LHC”. In: *IEEE transactions on applied superconductivity* 9.2 (1999), pp. 856–859.

[59] DE Baynham et al. “ATLAS end cap toroid final integration, test and installation”. In: *IEEE transactions on applied superconductivity* 18.2 (2008), pp. 391–394.

[60] C Mayri et al. “Suspension system of the barrel toroid cold mass”. In: *IEEE transactions on applied superconductivity* 16.2 (2006), pp. 525–528.

[61] J P Badiou et al. *ATLAS barrel toroid: Technical Design Report*. Technical design report. ATLAS. Electronic version not available. Geneva: CERN, 1997. DOI: 10.17181/CERN.RF2A.CP5T. URL: http://cds.cern.ch/record/331065.

[62] B Levesy et al. “Design and test of the titanium alloy tie rods for the CMS coil suspension system”. In: *IEEE transactions on applied superconductivity* 12.1 (2002), pp. 403–406.

[63] N Delruelle et al. “The high Beta cryo-modules and the associated cryogenic system for the HIE-ISOLDE upgrade at CERN”. In: *AIP Conference Proceedings*. Vol. 1573. 1. American Institute of Physics. 2014, pp. 811–818.

[64] V Corato et al. “The DEMO magnet system–Status and future challenges”. In: *Fusion engineering and design* 174 (2022), p. 112971.

[65] N Mitchell et al. “The ITER magnets: Design and construction status”. In: *IEEE transactions on applied superconductivity* 22.3 (2011), pp. 4200809–4200809.

[66] Min Liao et al. “Prototype engineering test platform of ITER magnet gravity support”. In: *Plasma Science and Technology* 15.2 (2013), p. 192.

[67] U Bhunia et al. “Development and performance evaluation of a conduction-cooled warm bore HTS steering magnet”. In: *Physica C: Superconductivity and its Applications* 604 (2023), p. 1354191.

[68] Jun-Sheng Zhang et al. “Magnetic and thermal design of HTS quadrupole magnet for newly developed superconducting proton cyclotron beam line”. In: *Journal of Superconductivity and Novel Magnetism* 32 (2019), pp. 529–538.

[69] Jaehwan Lee et al. “Thermal and mechanical design for refrigeration system of 10 MW class HTS wind power generator”. In: *IEEE Transactions on Applied Superconductivity* 30.4 (2020), pp. 1–5.

[70] O Tuvdensuren et al. “Design of an HTS module coil for a 750 kW-class superconducting wind power generator”. In: *Journal of Physics: Conference Series*. Vol. 1293. 1. IOP Publishing. 2019, p. 012077.

[71] O Tuvdensuren et al. “Structural design and heat load analysis of a flux pump-based HTS module coil for a large-scale wind power generator”. In: *Journal of Physics: Conference Series*. Vol. 1054. 1. IOP Publishing. 2018, p. 012084.

[72] Byeong-Soo Go et al. “Structural design of a module coil for a 12-MW class HTS generator for wind turbine”. In: *IEEE Transactions on Applied Superconductivity* 27.4 (2017), pp. 1–5.

[73] Magnus Dam et al. “Conceptual design of a high temperature superconducting magnet for a particle physics experiment in space”. In: *Superconductor Science and Technology* 33.4 (2020), p. 044012.

[74] Magnus Dam et al. “Design and modeling of AMaSED-2: A high temperature superconducting demonstrator coil for the space spectrometer ARCOS”. In: *IEEE transactions on applied superconductivity* 32.4 (2022), pp. 1–5.

[75] Magnus Dam et al. “Manufacturing and testing of AMaSED-2: A no-insulation high-temperature superconducting demonstrator coil for the space spectrometer ARCOS”. In: *Superconductor Science and Technology* 36.1 (2022), p. 014007.

[76] Xiao Long Guo et al. “Thermal and mechanical analysis on the cold mass support assembly of test cryomodule for IMP ADS-injector-II”. In: *AIP Conference Proceedings*. Vol. 1573. 1. American Institute of Physics. 2014, pp. 1341–1348.

[77] Jiandong Yuan et al. “Alignment and Deformation of the Cryostat in the CADS Injector II”. In: (2018).

[78] Alexander Gerbershagen et al. “A novel beam optics concept in a particle therapy gantry utilizing the advantages of superconducting magnets”. In: *Zeitschrift für Medizinische Physik* 26.3 (2016), pp. 224–237.

[79] KP Nesteruk et al. “Large energy acceptance gantry for proton therapy utilizing superconducting technology”. In: *Physics in Medicine & Biology* 64.17 (2019), p. 175007.

[80] Bin Qin et al. “Comparison of beam optics for normal conducting and superconducting gantry beamlines applied to proton therapy”. In: *International Journal of Modern Physics A* 34.36 (2019), p. 1942015.

[81] National Institute of Standards and Technologies. *Properties of solid materials from cryogenic to room-temperatures*. URL: https://trc.nist.gov/cryogenics/materials/materialproperties.htm (visited on 04/19/2023).

[82] Patxi Duthil. “Material properties at low temperature”. In: *arXiv preprint arXiv:1501.07100* (2015).

[83] Jishnu Dwivedi et al. *The alignment jacks of the LHC cryomagnets*. Tech. rep. 2004.

[84] *European Spallation Source*. European Spallation Source. URL: https://europeanspallationsource.se/article/2023/03/15/ess-installs-first-two-cryomodules-linac (visited on 04/19/2023).

[85] Laura Monaco et al. “Fabrication and treatment of the ESS medium beta prototype cavities”. In: *Proc. IPAC'17* (2017).

[86] Shrikant Pattalwar et al. “Key Design Features of Crab-Cavity Cryomodule for HiLumi LHC”. In: (2014).

[87] S Atieh et al. *Mechanical design and fabrication studies for SPL superconducting RF cavities*. Tech. rep. 2011.

[88] C-S Hwang et al. “Superconducting wiggler with semi-cold beam duct at Taiwan light source”. In: *Nuclear Instruments and Methods in Physics Research Section A: Accelerators, Spectrometers, Detectors and Associated Equipment* 556.2 (2006), pp. 607–615.

[89] P Wanderer et al. “Construction and testing of arc dipoles and quadrupoles for the Relativistic Heavy Ion Collider (RHIC) at BNL”. In: *Proceedings Particle Accelerator Conference*. Vol. 2. IEEE. 1995, pp. 1293–1297.

[90] Arnaud Devred et al. *Quench characteristics of full-length SSC R&D dipole magnets*. Springer, 1990.

[91] John N Galayda et al. “The LCLS-II: A high power upgrade to the LCLS”. In: *9th IPAC* (2018), p. 18.

[92] M Castoldi et al. *Thermal performance of the supporting system for the Large Hadron Collider (LHC) superconducting magnets*. Tech. rep. 1999.

[93] Nicolas Boulant and Lionel Quettier. “Commissioning of the Iseult CEA 11.7 T whole-body MRI: current status, gradient–magnet interaction tests and first imaging experience”. In: *Magnetic Resonance Materials in Physics, Biology and Medicine* (2023), pp. 1–15.

[94] THG Megson. “Structural and Stress Analysis”. In: (2005).

[95] Luca Piacentini et al. “Literature Review of Suspension Systems for Superconducting Elements”. In: *Machines* 11.10 (2023). ISSN: 2075-1702. DOI: 10.3390/machines11100929. URL: https://www.mdpi.com/2075-1702/11/10/929.

[96] MG Pullia et al. “Explorative studies of an innovative superconducting gantry”. In: *Journal of Physics: Conference Series*. Vol. 2420. 1. IOP Publishing. 2023, p. 012099.

[97] Xin-Jun Liu and Jinsong Wang. “Parallel kinematics”. In: *Springer Tracts in Mechanical Engineering* (2014).

[98] Matteo-Claudio Palpacelli et al. “Functional Design of a 6-DOF Platform for Micro-Positioning”. In: *Robotics* 9.4 (2020), p. 99.

[99] Wen-Lan Liu et al. “Methods for force analysis of overconstrained parallel mechanisms: a review”. In: *Chinese Journal of Mechanical Engineering* 30 (2017), pp. 1460–1472.

[100] Colin Caprani. *Virtual Work 3rd Year Structural Engineering*. 2010. URL: https://www.colincaprani.com/files/notes/SAIII/Virtual%20Work%201011.pdf (visited on 10/23/2024).

[101] Sanjay Govindjee. *Engineering mechanics of deformable solids: a presentation with exercises*. Oxford University Press, USA, 2012.

[102] Giovanni Legnani et al. “A new isotropic and decoupled 6-DoF parallel manipulator”. In: *Mechanism and Machine Theory* 58 (2012), pp. 64–81.

[103] *SKF spherical plain bearings and rod ends catalogue*. SKF. URL: https://cdn.skfmediahub.skf.com/api/public/0901d19680154a05/pdf_preview_medium/0901d19680154a05_pdf_preview_medium.pdf#cid-122020 (visited on 01/10/2023).

[104] Stephanie Forrest. “Genetic algorithms”. In: *ACM computing surveys (CSUR)* 28.1 (1996), pp. 77–80.

[105] Darrell Whitley, Soraya Rana, and Robert B Heckendorn. “The island model genetic algorithm: On separability, population size and convergence”. In: *Journal of computing and information technology* 7.1 (1999), pp. 33–47.

[106] Association Française du Froid Commission Cryogénie et Supraconductivité. *Fascicule de Cryogénie et de Supraconductivité*. 2019. ISBN: 978-2-37620-356-8. URL: http://www.affccs.org/index.php/venue/ (visited on 02/19/2024).

[107] ALLOYS INTERNATIONAL INC. *Invar 36 mechanical properties*. URL: https://alloysintl.com/ (visited on 02/19/2024).

[108] Vittorio Parma. "Cryostat design". In: *arXiv preprint arXiv:1501.07154* (2015).

[109] Simone Savazzi et al. "Optimization of a carbon-ion gantry layout based on simulated mechanical errors". Under submission.

[110] MG Pullia et al. "Gantries for carbon ions". In: *Health and Technology* (2024), pp. 1–11.

[111] *Transport Information Service*. German Insurance Association. URL: https://www.tis-gdv.de/tis_e/verpack/verpackungshandbuch/03verpackungshandbuch_0131-htm/ (visited on 01/10/2025).

[112] Péter Böröcz. "Vibration and acceleration levels of multimodal container shipping physical environment". In: *Packaging Technology and Science* 32.6 (2019), pp. 269–277.

[113] L. Deniau et al. "The MAD-X Program - User's Reference Manual - Version 5.03.06". In: (2017).

[114] F. C. Iselin. "The MAD Program - Physical Methods Manual - Version 8.13". In: (92).

Luca Piacentini was born in 1996 in Brescia, Italy. He obtained his Bachelor's degree in Mechanical and Industrial Engineering and a Master's degree in Mechanical Engineering (2021) from the University of Brescia. Since 2021, he has been a research assistant at Riga Technical University and carried out his research mainly abroad, at CERN. He is currently a Project Engineer at T.I.S. Service S.p.A. His research interests include mechanical design and system optimisation in social applications.